VISCOUS MODELING OF GROUND EFFECT AERODYNAMICS OF AIRFOIL AND JET

By

ALEX EARLE OCKFEN

A thesis submitted in partial fulfillment of
the requirements for the degree of

MASTER OF SCIENCE IN MECHANICAL ENGINEERING

WASHINGTON STATE UNIVERSITY
School of Mechanical and Materials Engineering

DECEMBER 2008

To the Faculty of Washington State University:

The members of the Committee appointed to examine the thesis of ALEX EARLE OCKFEN find it satisfactory and recommend that it be accepted.

Chair

ACKNOWLEDGMENT

First and foremost I would like to acknowledge my graduate advisor Dr. Konstantin Matveev, who made himself available for my questions and concerns at all times, no matter the subject or complexity. In addition to the vast technical and professional guidance from Dr. Matveev, I am thankful for his constant motivation and effort to provide diverse research, publication, and presentation opportunities. The members of my graduate committee, Dr. Prashanta Dutta and Dr. David Stock, have also been very helpful and provided feedback.

Although my committee members have been instrumental, this educational experience would not have been possible without the handful of additional professors at Washington State University who provided the challenging coursework which has provoked my interest in the engineering field. In particular, Dr. Cecilia Richards provided the opportunity to complete an assistantship and related opportunities to gain experience with student interaction. All of these tasks could not have been completed without the constant support from members of the office staff, Jan Danforth, Bob Ames, and Gayle Landeen who have taken time on a weekly basis to make my experience as smooth as possible. Any additional technical difficulties were quickly addressed by Michael Shook and Giac Pham.

Lastly, I would like to thank my family and friends whose support and advice have been a driving force for all of my achievements.

VISCOUS MODELING OF GROUND EFFECT AERODYNAMICS OF AIRFOIL AND JET

Abstract

by Alex Earle Ockfen, M.S.
Washington State University
December 2008

Chair: Konstantin I. Matveev

Wing-in-Ground craft and aerodynamically assisted marine vehicles take advantage of increased lift and reduced drag of wing sections in ground proximity. However, at relatively low speeds or heavily loaded craft, the passive aerodynamic lift may not be sufficient to provide vehicle support. In such cases, a flap at the wing trailing-edge or properly placed jet propulsor may be implemented to augment vehicle lift.

Parametric design studies are completed for several ground effect configurations gaining insight into fundamental flow patterns and optimal performance regimes with flap and/or jet components implemented. This research takes advantage of efficient and low-cost numerical methods suited for design studies. The technique consists of a two-dimensional, steady-state, incompressible, viscous, finite volume method utilizing RANS turbulence models. Grid generation and solution of the Navier-Stokes equations are completed using Fluent 6.3. Validation of solution approach is provided with experimental validation of aerodynamic forces in and out of ground effect, plane turbulent jets, planar impinging jets, and static airfoil-flap-jet configurations.

The influence of flap mechanization is first studied on the NACA 4412 airfoil in ground effect. Aerodynamic forces are calculated, and the effects of attack angle, Reynolds number, ground height, and flap deflection are presented for split and plain flaps. Overall, flap use on ground-effect vehicles with small attack angles is found to be beneficial for small flap deflections up to 5% of the chord, where an enhanced aerodynamic efficiency is realized.

At low speeds where flap use is insufficient, the Power-Augmented-Ram (PAR) concept implements jet support to sufficiently augment vehicle lift. A simplified aerodynamic jet propulsor model, the ducted momentum source, is developed to account for upstream jet suction and downstream jet spreading. First, beneficial obliquely impinging propulsor configurations are studied with cross flow, and are then combined with a platform-flap to simulate a PAR vehicle.

Results of PAR simulations suggest that in low-speed operation, harmful jet ingestion may occur. To avoid this phenomenon, the propulsor should be placed at impingement angles less than 30° and at moderate ground distances. With increasing PAR forward speed, performance may be increased by reducing flap deflection and impingement angle.

TABLE OF CONTENTS

Page

CHAPTER

APPENDIX

LIST OF TABLES

LIST OF FIGURES

CHAPTER ONE

INTRODUCTION

1.1 Motivation

Wing-In-Ground (WIG) vehicles take advantage of the ground effect when operating at high speeds in close proximity to the ground. Although only limited amounts of ground effect design and development have been completed, there are many factors which motivate further studies in this flight regime. With the growing scarcity of oil increasing fuel prices, the most significant short term benefit of the ground effect is its substantial increase in aerodynamic efficiency (Barber et al. 1998, Rozhdestvensky 2000, Chun and Chang 2003, Firooz and Gadami 2006, Rozhdestvensky 2006, etc.). With further studies of the fundamental behavior of ground-effect flight, it appears likely that the increase in aerodynamic efficiency can be harnessed and successfully used in high-speed human and cargo transportation. This concept has the potential to provide a more economical and energy efficient alternative to current aircraft and marine vehicles used for transportation applications.

The large increase in aerodynamic efficiency is a result of two phenomena that only present themselves very near a ground surface. The first such occurrence is called the “span based ground effect” and occurs as the ground-effect vehicle moves to within one wingspan of the ground. At this point the wingtip vortices, which develop as the under-wing high-pressure fluid passes over the tip of the airfoil to the low-pressure region above the wing, begin being suppressed by the approaching ground surface. As these wingtip vortices are blocked, the induced drag is significantly reduced.

In addition to the previously described drag reduction, as the ground-effect vehicle approaches one chord of the ground, another effect is visible. At such minute ground distances, flow starts being trapped between the airfoil and ground and forms a pressure cushion beneath the vehicle. A schematic of this effect is shown in Fig. 1.1, and ultimately yields an increase in vehicle lift. Therefore, it is clear the coupling of drag reduction and lift augmentation will yield an increase in flight efficiency. For vehicles to take full advantage of both ground effect factors, they should ideally operate in the "extreme ground effect" regime within one tenth chord of the ground.

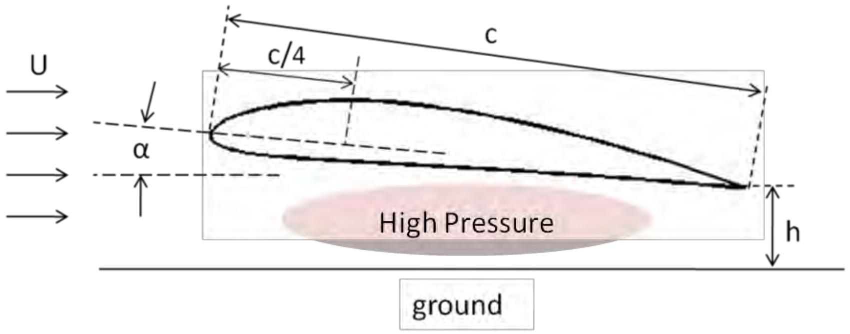

Fig. 1.1 Illustration of WIG aircraft in extreme ground effect behavior.

Although the development of ground-effect vehicles have been limited due to their complex nature, full scale ground-effect vehicles (or Ekranoplans) were designed and built in Russia (Kirillovikh, 1995). Ekranoplans have served both military and transportation applications: two examples are shown in Fig. 1.2. These craft have successfully demonstrated the chord based ground effect as shown in Fig. 1.2, and can ideally increase the aerodynamic efficiency, or lift-to-drag ratio, by up to 50%.

While there are great benefits of such vehicles, the stability requirements are not nearly as forgiving in ground effect as they are for high altitude flight (Kirillovikh, 1995). These increased stability difficulties coupled with reduced jet propulsor performance near the ground have been some of the drawbacks limiting the study of ground-effect aerodynamics. In the big picture, increased aerodynamic efficiency has potential to significantly overcome any challenges or difficulties in the ground effect development process. Therefore, motivation to gain a further understanding of ground-effect vehicles is essential for development of the next generation of energy efficient commercial and military transport platforms.

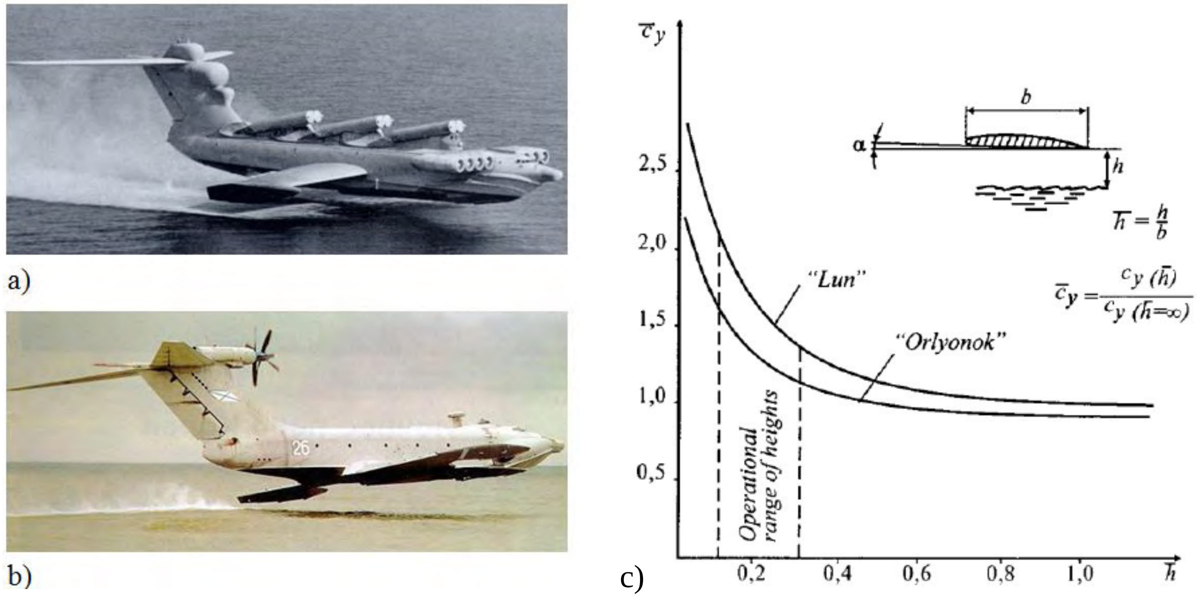

Fig. 1.2 Full scale ground-effect vehicles: a) rocket carrier "Lun"; b) transport carrier "Orlyonok"; c) lift performance of ground-effect vehicles. Pictures of "Lun" and "Orlyonok" were found online at www.aerospaceweb.org and www.se-technology.com respectively.

1.2 Objective

With the considerable motivation discussed above, the objective of this work is to further the understanding of aircraft and amphibious vehicle operation in close ground proximity. The major focus of the research will be to improve the operating efficiency of ground-effect vehicles. Although increased aerodynamic efficiency takes center stage with the rapid increasing fuel prices and environmental concerns, safety issues will also be studied for jet propulsor configurations used in ground proximity. Overall, the goal is to use parametric design studies to optimize ground effect flight while providing insight into important fundamental flow behaviors.

Aerodynamic efficiency is to be optimized in ground effect flight by varying common WIG parameters such as ground height, attack angle, vehicle forward speed, and Reynolds number. In addition to the simple manipulation of the aircraft speed and position, implementation of more complex geometries will also be considered. These complex geometries will consist of added components such as the trailing edge flap, which is commonly implemented as a lift control device. Ideally, the study will optimize ground effect flight efficiency at several common operating configurations with and without added components. Ultimately, it will provide a set of design rules for future ground-effect vehicle development.

Although safety concerns have been addressed from an aerodynamic stability standpoint (Kornev and Matveev, 2003), the behavior of a jet propulsor in ground effect must be studied further. In such a flight regime, the aircraft jet may intentionally or unintentionally impinge on the ground surface during operation. The fundamental flow structures in such a case are of great interest to the ground-effect vehicle operation. Most importantly, it must be determined if similar phenomenon to the “hot gas ingestion” in vertical/short takeoff and landing vehicles (V/STOL) will occur in ground-effect vehicles and harm propulsor performance.

This study will not only optimize the common WIG vehicle, but additionally provide insight into the design of high speed amphibious vehicles such as the Power-Augmented-Ram Wing-In-Ground (PAR-WIG) vehicle which uses the ground effect in an unconventional manner (section 1.4.2).

1.3 Approach

Several methods can be utilized in the study of fundamental ground-effect vehicles. The two most common approaches for studying ground effect flight are experimental testing and mathematical modeling.

Experimental methods are the most sought after technique for studying physical flow behavior of aerodynamic vehicles. This is evident as experimental wind tunnel data are commonly used to validate numerical models. However, the benefit of experimental testing comes at a heavy price in ground effect. The most prominent difficulty in experimental ground effect studies lies in the implementation of proper ground conditions. In ground proximity, the vehicle moves at a finite forward speed both through the air and over the ground. Therefore, the wind tunnel must be modified to properly account for the moving ground condition. The most effective way to approximate the physical situation is to implement a moving belt boundary condition at the bottom of the tunnel (Ahmed et al., 2006). Due to the large expense of this technique, simplified blowing or suction systems are generally used to control the boundary layer on the ground (Hirata and Hino, 1997).

In addition to the above difficulties, added time and costs are anticipated for model creation and setup of complex measurement systems and experimental data is limited to Reynolds numbers much lower than the practical ground effect operating regime (10^6 – 10^9). Although experimental methods are still the most trusted method, high cost and complexities significantly reduce their applicability.

Due to facility restrictions and limitations in economic resources an experimental ground effect study is not currently possible at Washington State University. Instead, the current approach will implement computer aided numerical techniques to solve mathematical equations governing ground effect fluid flow. Not only does the numerical procedure present an inexpensive alternative to experimental testing, but it is ideal for a design study in which geometry and Reynolds number can be readily modified at minimal cost. Additionally, the method will prove beneficial when complex components such as jets or flaps are implemented into the flow. Overall, the use of numerical methods will provide a quick and inexpensive way to determine important flow patterns and beneficial vehicle configurations in ground effect.

Many simplified numerical models have been previously used for ground effect simulations. These methods have consisted of matched asymptotic expansions for configurations in limiting "extreme ground effect" regimes, and potential flow techniques for ground-effect vehicles with and without added jet support (e.g., Windall and Barrows 1970, Gallington et al. 1976, Smithey et al. 1977, Katz and Plotkin 1991, Rozhdestvensky 2000, and Kornev and Matveev2003). Unfortunately, these simplified methods significantly reduce the usefulness of the numerical technique and do not allow optimization of ground-effect vehicles over a broad flight regime. Perhaps the most questionable assumption in the simplified models is the disregard of viscosity.

By taking a step back, it becomes clear that accounting for viscosity is essential in ground effect and cannot be neglected. For illustration purposes, imagine a WIG vehicle operating in the "extreme ground effect" as shown in Fig. 1.1. The boundary layer on this vehicle may account for a significant portion of the distance from vehicle to ground. In such cases, experimental observations show that aerodynamic forces in ground effect cannot be accurately predicted unless the boundary layer is correctly represented in the tests (Ahmed et al., 2006). This phenomenon can also be directly correlated to the need for a moving ground boundary condition in order to correctly represent the physical situation regarding boundary layer creation on the ground (Barber et al., 1998).

In addition to the inherent need for viscosity in close ground proximity, it must also be accounted for when jet propulsors are included in the vehicle design. Free jet spreading and mixing of a jet propulsor is driven by the viscous nature of the working fluid. Therefore, viscosity must be included to properly model propulsor behavior and jet-ground interaction for propulsor ingestion studies mentioned in section 1.2 and presented in Chapter 5.

Numerous researchers have come to similar conclusions and studied ground-effect vehicles by viscous numerical methods (Hsiun and Chen 1996, Barber et al. 1998, Chun and Chang 2003, Huminic and Lutz 2005, Firooz and Gadami 2006, and Mahon and Zhang 2008). These previous studies have generally focused on airfoil type, turbulence model, ground boundary condition, and effects of varying the ground height of simple ground-effect vehicles. Current numerical procedures will be built off the methods referenced in the above studies. This study will be the first to implement such advanced components as the trailing edge flap or jet propulsor, which require a more complex framework with the ability to not only predict aerodynamic forces but also account for the complex flow behavior from a jet propulsor.

After the above study of several possible approaches to ground-effect vehicle design, viscous numerical methods have emerged as the most appropriate technique. This technique is chosen for current research due to its inexpensive and efficient nature, configuration change freedom, and ability to account for the physical situation in ground effect. It is hoped that this technique will provide a significant amount of design information for ground-effect vehicles, and can be used in the future to reduce the expense of experimental validation studies.

1.4 Vehicles Benefiting From Ground Effect

Over the last few decades the motivating factors discussed in section 1.1 have led to the emergence of many ground-effect concepts. Concepts have ranged from the large scale military and transport applications shown in Fig. 1.2 to small personal craft. In all cases, the goal is to take advantage of beneficial aerodynamic properties that are obtainable in close ground proximity (Fig. 1.2c).

This study will focus on two common ground effect designs which show promise for practical military and commercial applications. The first concept to be studied is the Wing-In-Ground aircraft, which has been the focus of the majority of previous studies. A second concept, the PAR-WIG vehicle, will use jet support in ground effect to attempt to overcome some of the common setbacks of WIG vehicles at static and low speeds.

1.4.1 Wing-In-Ground

The Wing-in-Ground effect, taking place when an airfoil flies in close proximity to the ground, provides beneficial aerodynamic properties discussed in section 1.1. These benefits include a decrease in the induced drag due to suppression of wingtip vortices and an increase in the lift as flow is trapped underneath the aircraft. The Wing-In-Ground aircraft concept takes advantage of this flight regime in order to improve aerodynamic efficiency by up to 50%. Common WIG aircraft are shown in Fig. 1.2 and consist of an airfoil placed in close proximity to ground (Fig. 1.1). Various experimental Wing-in-Ground (WIG) craft, have also been constructed and tested in the last century (e.g., Rozhdestvensky 2006).

Although the efficiency increase in ground effect is the most well known benefit of these vehicles, they also have many other advantages. They have the ability to carry large payloads similar to that of ships, although WIG aircraft operate at much higher speeds of 70-350 miles per hour. Additionally WIG aircraft are not limited to operation over water surfaces; these vehicles have amphibious capabilities and can operate over any relatively flat ground surface (e.g., water, ice, snow, land). They can additionally be designed to take-off and land on either solid land or water surfaces.

With the above benefits, WIG aircraft are ideal for several practical applications including a next generation high speed sea transportation vehicle for passenger and cargo transport (Chun and Chang, 2003). Furthermore, the amphibious nature of the WIG aircraft makes it an ideal choice for military applications. In the near ground operating range, it will fly below air defense radar and operate above regions in which it would be vulnerable to common marine mine/torpedo weapons.

As mentioned above, the WIG aircraft has been studied previously by several researchers (Hsiun and Chen 1996, Barber et al. 1998, Chun and Chang 2003, Huminic and Lutz 2005, Firooz and Gadami 2006, and Mahon and Zhang 2008). The current focus of WIG aircraft will be to optimize aircraft efficiency with implementation of a trailing edge flap configuration. In an attempt to further improve ground effect performance, the Power-Augmented-Ram Wing-In-Ground (PAR-WIG) concept, which uses jet support, will be discussed in the next section.

1.4.2 Power-Augmented-Ram

A new generation of aerodynamically assisted transport platforms couple the Power Augmented Ram (PAR) principle with the beneficial ground effect regime (Gallington 1987, Kirillovyh and Privalov 1996, Matveev and Malhiot 2007, Matveev 2008). A schematic of the PAR-WIG concept is shown in Fig. 1.3 with airfoil platform. The vehicle consists of a platform operating in extreme ground effect (chord-to-height ratio > 10) with side hulls barely touching the ground or water surface. The idea behind the PAR-WIG concept is to add jet support to the WIG vehicle in order to avoid the problematic WIG configurations at low and static speeds where the passive aerodynamic lift is insufficient in supporting the vehicle.

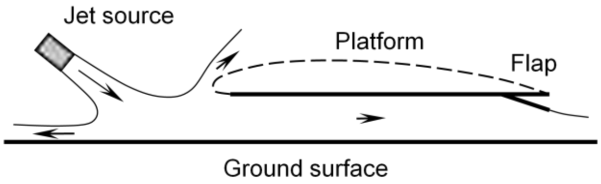

Fig. 1.3: Schematic of Power-Augmented-Ram concept. Arrows indicate directions of main air jets at zero or low forward speeds. The platform can be made in form of a wing (dashed contour) to augment passive aerodynamic lift at high speeds.

The jet support is introduced as a row of radial jets or a slot jet source mounted in front of the platform and directed downstream into the nearly two-dimensional channel created by platform, side hulls, and ground. Flow is trapped in this region using a trailing edge flap that creates a pressurized air cushion in the channel. Smithey et al. (1977) have provided a comparison between potential flow theory and experiments, which suggest the ratio of platform lift to momentum flow of the jet entering the under-platform channel in static cases is proportional to the platform chord over the ground height (in extreme ground effect yielding lift up to ten times the jet momentum). This lift increase is an order of magnitude greater than that of V/STOL craft and can be explained by the high pressure of nearly stagnated jets acting over the entire platform bottom. Nearly all lift is accounted for with the pressure cushion at low or zero speeds. At large vehicle forward speeds the jet support becomes unnecessary and the PAR-WIG vehicle may in some cases be approximated by the common WIG aircraft with a trailing edge flap implemented.

The PAR-WIG concept shares all of the common benefits of the WIG aircraft as explained in section 1.4.1. Additionally the jet support provides safe operations at low speeds while the ability of side hull structures to safely interact with the ground reduces stability difficulties found in WIG vehicles. With the many benefits, it is possible the PAR-WIG craft could be the next generation of amphibious vehicles. PAR-WIG boasts a greater weight efficiency (50%) and reduced thrust-to-weight ratio (0.15-0.25) in comparison to current air cushion vehicles. Similar to use of air cushion vehicles, the PAR-WIG craft provides an ideal platform for use as an amphibious military landing craft (water to land).

Research within this thesis is geared toward advancing the complex WIG-flap configuration by adding a PAR propulsor to the model. With a model of the PAR-WIG vehicle, ground effect flight can be optimized for safe and increasingly efficient operating configurations. It is thought that the knowledge of such configurations will benefit the advancement of high efficiency, high speed, amphibious, and transportation vehicles.

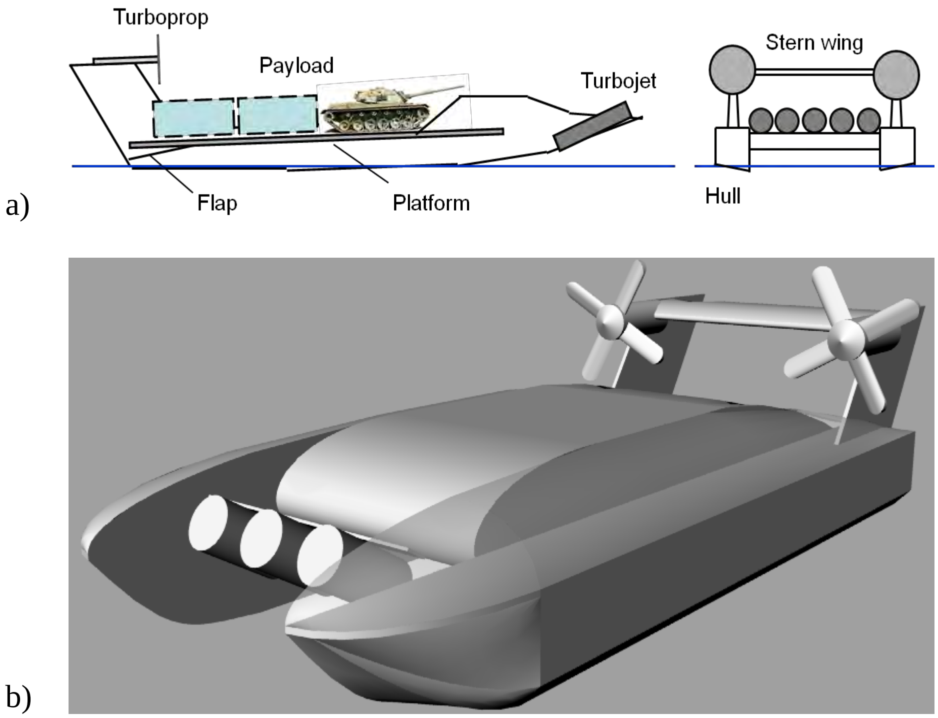

Fig. 1.4: Power-Augmented-Ram vehicle under development at Washington State University: a) flat plate deck for cargo transport; b) airfoil platform to enhance passive aerodynamic lift.

Figure 1.4 illustrates the current Power Augmented Ram Vehicle (PARV) concept being developed at Washington State University with use of a flat plate platform replacing the WIG airfoil. Radio controlled models were created, and successfully demonstrate the amphibious nature and maneuverability of the PARV concept. This study will also contribute to design and development of future radio controlled, and experimental models to be created.

CHAPTER TWO

NUMERICAL MODELING AND VALIDATION

2.1 Numerical Modeling

It is widely known that most forms of the Navier Stokes equations written for common engineering applications cannot be solved analytically. Therefore, a numerical approach must be used to solve these equations. Over the last few decades several commercial programs have been developed to solve many of the common engineering flows. The current research implements a commercial code rather than developing a Navier Stokes solver, owing to the previous success of ground effect modeling with commercial codes. Due to its availability and extensive aerodynamic validation, the finite volume solver Fluent 6.3 has been chosen for the current research. The use of Fluent has been heavily validated in section 2.2 and Chapter 3.

Gambit 2.3 is the mesh generator for Fluent, and is used to create all meshes. Gambit has the capability of creating both two and three dimensional meshes consisting of structured or unstructured geometries.

2.1.1 Governing Equations

The mass continuity and momentum conservation (Navier Stokes equations simplified for Newtonian incompressible flow) equations are shown below. The continuity equation describes the physical principle of conservation of mass, while the momentum equation represents Newton's 2nd Law or the conservation of momentum. The equations below represent the general unsteady, viscous, incompressible, constant viscosity flow with a source:

$$\frac{\partial}{\partial x_i}(u_i) = 0, \tag{2-1}$$

$$\rho\frac{\partial}{\partial t}(u_i) + \rho u_j\frac{\partial}{\partial x_j}(u_i) = -\frac{\partial p}{\partial x_i} + \mu\frac{\partial}{\partial x_j}\left(\frac{\partial u_i}{\partial x_j}\right) + S, \tag{2-2}$$

where u_i is the velocity in the i-direction. Symbols ρ, μ, and p correspond to the density, molecular viscosity, and pressures, respectively. The single term in the continuity equation is the divergence of the velocity, while the first and second terms on the left-hand side in the momentum equation are the transient and momentum advection terms. The three terms on the right-hand side of the momentum equation are the pressure force, viscous term, and source. The source term in Eq. (2-2) is defined by the user and is appropriately linearized. All governing equations in sections 2.1.1 are written in Cartesian index notation with summation convention.

The incompressible and constant viscosity assumptions are similarly used in the majority of PAR and WIG studies (Hsiun and Chen 1996, Barber et al. 1998, Chun and Chang 2003, Firooz and Gadami 2006) and yield reasonable results for ground effect flight regimes. The two dimensional assumption is also valid for the ground effect aerodynamics studied. Basically the ground suppresses the majority of the three dimensional effects and the aerodynamic forces of interest are dominated by the pressure in between the airfoil and the ground. In addition, ground-effect vehicles generally include endplates which further promote a two dimensional behavior.

Due to the high speed and high Reynolds number of aerodynamically supported flows, Eqs. (2-1) and (2-2) must be modified for the fully turbulent nature of practical ground effect flows. A common approximation used to model turbulent flows is to time average the Navier Stokes equations, and hence obtain a time averaged turbulent solution instead of the instantaneous solution. Derivation of the time averaged or Reynolds Averaged Navier Stokes (RANS) equations are obtained by decomposing the instantaneous variables (velocity, pressure, etc.) from Eqs. (2-1) and (2-2) into mean and fluctuation components (Ferziger & Peric, 1999);

$$u_i = \overline{u}_i + u_i^{'}, \tag{2-3}$$

where u_i is the instantaneous velocity in the i-direction and $\overline{u_i}$ and $u_i^{'}$ are the time averaged velocity and instantaneous fluctuating velocity in the i-direction. When the decomposed velocity is plugged into the continuity equation and averaged, the fluctuating terms will drop out and leave you with an equation of the same form as Eq. (2-1),

$$\frac{\partial}{\partial x_i}(\overline{u_i}) = 0, \tag{2-4}$$

where it is important to realize that in this case the velocity, $\bar{u}_i$, is an time average instead of an instantaneous value. Similarly, the decomposed velocity in Eq. (2-3) can be plugged into the momentum Eq. (2-2) and averaged. The resulting equation is the time averaged momentum equation,

$$\rho\frac{\partial}{\partial t}(\overline{u_i}) + \rho\frac{\partial}{\partial x_j}\left(\overline{u_i}\overline{u_j}\right) = -\frac{\partial \bar{p}}{\partial x_i} + \mu\frac{\partial}{\partial x_j}\left(\frac{\partial \overline{u_i}}{\partial x_j}\right) + \frac{\partial}{\partial x_j}\left(-\rho\overline{u_i^{'}u_j^{'}}\right) + S, \tag{2-5}$$

where $\bar{u}_i$ is the time averaged velocity in the i-direction, and symbols ρ, μ, and $\bar{p}$ correspond to the density, molecular viscosity, and time averaged pressures, respectively. The terms on the left-hand side of the momentum equation are the transient and momentum advection terms. The four terms on the right-hand side of the momentum equation are the pressure force, viscous term, Reynolds stress, and user defined source. The Reynolds stress term in Eq. (2-5) is unknown and contains the mean of the product of turbulent fluctuating velocities which will be modeled by the Boussinesq approximation,

$$-\rho\overline{u_i^{'}u_j^{'}} = \mu_t\left(\frac{\partial \overline{u_i}}{\partial x_j} + \frac{\partial \overline{u_j}}{\partial x_i}\right) - \frac{2}{3}\left(\rho k + \mu_t\frac{\partial \overline{u_i}}{\partial x_i}\right)\delta_{ij}\ , \tag{2-6}$$

where μ_t and k represent the turbulent viscosity and turbulent kinetic energy. The Boussinesq approximation as shown by Eq. (2-6) relates the mean of the product of turbulent fluctuating velocities to a viscous stress term. With this approximation the turbulent viscosity is assumed to be isotropic, and this assumption becomes invalid in anisotropic turbulent flows (e.g. strongly swirling). In general the Boussinesq approximation can successfully model equilibrium flows which avoid strong streamline curvature and discontinuities in strain rate.

The RANS equations are commonly used for commercial applications due to their extensive validation, robustness, and inexpensive computational cost. For the parametric design application at hand it becomes essential to numerically solve an inexpensive set of equations (low computational time). More complex methods, which model reduced portions of the flow, such as Large Eddy Simulation (LES) and Direct Eddy Simulation (DES), are currently much too expensive for use in practical applications. Although the use of the RANS equations, Eq. (2-4) and (2-5), model all turbulent scales, their use has been validated for aircraft operation in and out of ground effect (Chapters 2 and 3).

The RANS equations are commonly used in steady state applications while their use in the transient regime has been questioned due to the inherent time averaging in their derivation process. Wilcox (2006) explains the situation very nicely. Unsteady RANS solutions are valid as long as the turbulence time scales are much smaller than that of the mean transient flow structures. Examples of several successful transient RANS simulations are the vortex shedding behind rectangular or cylindrical objects (Constantinescu et al. 2003, Iaccarino et al. 2003) and flow over a blunt airfoil (Doolan, 2007). However, loss in accuracy should be expected in cases in which the turbulent and mean flow structures operate on similar time scales.

In many applications the above equations must be coupled with the energy equation. The energy equation represents the first law of thermodynamics, also known as the conservation of energy. In our application there are no significant energy interactions or temperature gradients; therefore, the energy equation and momentum/continuity equations are decoupled. Consequently, the energy equation will not be solved in the current design study.

Overall, the above equations describe the physical nature of turbulent flow over an airfoil in ground effect. As mentioned above, the finite volume (FVM) solver Fluent will be used to solve the final RANS equations which govern our ground proximity flow, Eqs. (2-4) and (2-5). However, before the solution can proceed, a turbulence model must be adopted to close the RANS equations with the Boussinesq approximation.

2.1.2 Spalart-Allmaras Model

The Spalart-Allmaras model used by Fluent is a relatively new one equation turbulence model. The Spalart-Allmaras model solves a single equation for the modified turbulent viscosity. This model has been designed specifically for wall bounded aerodynamic flows, and has shown to provide good results for boundary layers subjected to adverse pressure gradients (Fluent 2005, Wilcox 2006). Although the model is very robust it poorly predicts jet flows (Rumsey and Ying, 2002), and cannot predict turbulent decay in uniform flows. In addition, Rumsey and Ying reference a high lift study which validates the Spalart-Allmaras model against experimental pressure and velocity profiles in separated flow conditions.

The Spalart-Allmaras model provides closure for the Navier-Stokes equations with the Boussinesq approximation. The additional equation for the modified turbulent viscosity $\tilde{\nu}$ is:

$$\frac{\partial}{\partial t}(\rho\tilde{\nu}) + \frac{\partial}{\partial x_i}(\rho\tilde{\nu}\overline{u_i}) = G_\nu + \frac{1}{\sigma_{\tilde{\nu}}}\left\{\frac{\partial}{\partial x_j}\left[(\mu + \rho\tilde{\nu})\frac{\partial\tilde{\nu}}{\partial x_j}\right] + C_{b2}\rho\left(\frac{\partial\tilde{\nu}}{\partial x_j}\right)^2\right\} - Y_\nu + S_{\tilde{\nu}}, \qquad (2\text{-}7)$$

where $\sigma_{\tilde{\nu}}$ and C_{b2} are constants and $S_{\tilde{\nu}}$ is the user defined source term. As before the first and second terms of the transport equation represent unsteady effects and advection, respectively. The term within the brackets on the right side represents the diffusive transport. The production and destruction of turbulent viscosity are represented by G_ν and Y_ν and are elaborated on in

Fluent Manual (2005). These terms account for the viscous damping and wall blocking in the near wall region. The turbulent dynamic viscosity is then determined as follows,

$$\mu_t = \rho \tilde{\nu} f_{\upsilon 1}, \tag{2-8}$$

where $f_{\upsilon 1}$ is a viscous damping function. Equation (2-8) connects the Spalart-Allmaras turbulence model back to the Boussinesq approximation of the Reynolds stress term. Although the turbulent viscosity and modified turbulent viscosities are the same throughout most regions of flow, the above relation accounts for the change in turbulent viscosity near walls. For a more detailed explanation of the Spalart-Allmaras model and its coefficients, the reader is referred to Fluent Manual (2005), paper by Spalart and Allmaras (1991), or book by Wilcox (2006). Implementation of the Spalart-Allmaras model closes the set of governing equations (2-4), (2-5), (2-7) and provides a mathematical model which can be solved by numerical means.

Lastly, the Spalart-Allmaras model is a low Reynolds number turbulence model which can be integrated through the viscous sub-layer. However, if a coarse mesh is desired, wall functions can be implemented in the expanded Fluent version. Fluent will automatically use the near wall approach when $y^+ < 11.225$, and implement wall functions (refer to section 2.1.8) at larger y^+ values.

2.1.3 k-ε Model

The k-ε model used by Fluent is an extensively used two equation turbulence model. The two equations are for the turbulent kinetic energy, k, and dissipation rate, ε. The k-ε model is implemented in the current research due to its robust and computationally inexpensive nature, coupled with its ability to accurately predict planar jet flows (Wilcox, 2006). Although there are many benefits to the current model, it poorly predicts boundary layer behavior with strong adverse pressure gradients and may yield significant errors in cases where production does not equal dissipation (Wilcox, 2006).

The kinetic energy equation for the k-ε model is defined as the trace of the Reynolds stress tensor. This is a very well understood equation which provides information on the transport of turbulence,

$$\frac{\partial}{\partial t}(\rho k) + \frac{\partial}{\partial x_i}(\rho k \overline{u}_i) = \frac{\partial}{\partial x_j}\left[\left(\mu + \frac{\mu_t}{\sigma_k}\right)\frac{\partial k}{\partial x_j}\right] + G_k - \rho\epsilon + S_k. \tag{2-9}$$

In Eq. (2-9) ρ, μ, μ_t, σ_k, k, and ε represent the density, viscosity, turbulent viscosity, turbulent Prandtl number, turbulent kinetic energy, and dissipation. The first two terms on the left hand side of (2-9) are the transient and convection of turbulent kinetic energy while the first through fourth terms on the right hand side represent the diffusion, production (G_k), dissipation, and source (S_k) of turbulent kinetic energy.

To provide closure for the k-ε model, an additional ε equation is necessary to determine the turbulent length scale. The ε equation can be found exactly by time averaging a complicated moment of the Navier stokes equations (Wilcox, 2006). Unfortunately, double and triple correlations in this exact derivation cannot be calculated or experimentally measured, so the ε equation is instead generally modeled as,

$$\frac{\partial}{\partial t}(\rho\epsilon) + \frac{\partial}{\partial x_i}(\rho\epsilon \overline{u}_i) = \frac{\partial}{\partial x_j}\left[\left(\mu + \frac{\mu_t}{\sigma_\epsilon}\right)\frac{\partial k}{\partial x_j}\right] + C_{1\epsilon}\, G_k \frac{\epsilon}{k} - C_{2\epsilon}\rho\frac{\epsilon^2}{k} + S_\epsilon\ , \tag{2-10}$$

where $C_{1\varepsilon}$ and $C_{2\varepsilon}$ are constants and $G_{k,}$ $S_{\varepsilon,}$ and σ_ε represent the production of turbulent kinetic energy, dissipation source, and turbulent Prandtl number. The first two terms on the left hand side of (2-10) are the transient and convection of ε while the first through fourth terms on the right hand side represent the diffusion, production, dissipation, and source of ε. The k-ε model is presented here with Eqs. (2-9) and (2-10), for further description of modeling assumptions and list of constant values please refer to Fluent manual (2005) or book by Wilcox (2006). Implementation of the k-ε model closes the set of governing equations (2-4), (2-5), (2-9), (2-10) and completes a model which can be solved by numerical means.

Lastly, the k-ε model is a high Reynolds number turbulence model which cannot be integrated through the viscous sub-layer. Generally the k-ε model uses wall functions to account for the boundary layer behavior which it cannot model, Eq. (2-12). However, in some cases wall functions are invalid and a near wall approach is necessary. Fluent has provided damping functions which allow for an accurate solution with integration to the wall.

2.1.4 Finite Volume Method

The Finite Volume Method (FVM) used by Fluent is one of the many approaches that can be taken when solving our RANS governing differential equations and turbulence model. In such a problem the flow field of interest is broken down into many cells or control volumes. An example of such a flow field can be visualized with the two dimensional structured grid shown in Fig. 2.1. The center cell of interest in Fig. 2.1 is P while E, W, N, S are the neighboring cells. The faces between cells are noted by lowercase e, w, n, s. This terminology is widely used for the FVM, and was adopted from (Patankar, 1980).

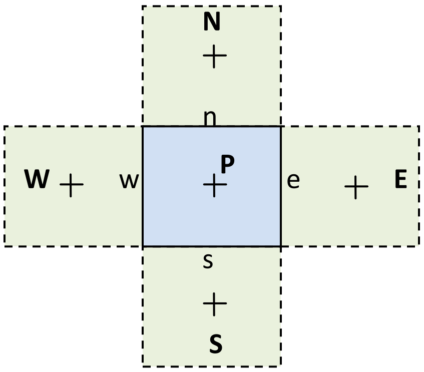

Fig. 2.1: FVM control volume schematic and nomenclature.

In FVM the governing equations are written for each cell in the domain. The equations are then integrated over the control volumes to ensure quantities are conserved in all cells of interest. The Gauss Divergence Theorem is generally applied to convert volume integrals of the divergence into summations of surface fluxes over the boundaries, accounting for property transfer in and out of the control volume. When an unsteady finite volume method is implemented transient terms may be modeled with implicit (using values at the current time step) or explicit schemes (using values from previous time step). For a more thorough discussion of this topic refer to the pioneering work of Patankar (1980).

2.1.5 Discretization

However, it should be noted that the finite volume governing equations developed are still non-linear partial differential equations (PDE). To permit a simple numerical solution, the continuous PDEs must be converted into a discrete set of linear equations. This is known as the "discretization process" and consists of writing the differential equations as a set of algebraic equations in terms of variables at discrete points (located at cell centers).

A discrete set of the algebraic equations can be easily solved by numerical methods which would yield the flow variables (e.g. velocity, pressure) at grid points studied. Therefore, the numerical solution is an approximation which yields results similar to an experimental study with a finite number of data points (Patankar, 1980).

Many discretization schemes exist and can easily be implemented in Fluent. Options for discretization of pressure terms include standard, linear, PRESTO (pressure staggering option), and 2nd order schemes. In addition convective discretization schemes available in Fluent are 1st order upwind, power law, 2nd order upwind, Quick, and 3rd order Muscle (Van Leer, 1979). Where the convective upwind scheme simply assumes the variable at a point is equal to the value upwind of that location (assuming no diffusion). From this model the schemes successively increase in accuracy by accounting for more realistic interaction between convection and diffusion. The most accurate convective model, the 3rd order muscle scheme, blends the central difference and the 2nd order upwind schemes to improve performance.

By approximating the governing equations with discrete points, the model equations generally no longer match the initial governing equations. The assumptions made generally add additional terms to the governing equations (e.g. central difference schemes are known to add a 3rd order dispersive force while upwind schemes generally add a 2nd order artificial viscosity). These discrepancies in the discretized equations can lead to unphysical wiggles in the solution or artificial damping of fluid behavior. Therefore, it is important to understand the numerical errors which may be expected with chosen discretization.

The schemes implemented in the current research consist of higher order schemes which vary depending on flow phenomenon (e.g. jet, airfoil). All of the following studies clearly define their discretization methods and a full explanation of their implementation is given in Fluent (2005).

2.1.6 Pressure-Velocity Coupling

The final hurdle that must be overcome in the solution process of the fluid flow equations is determining a method to account for the unknown pressure driving force in the momentum equations. Although there is no specific equation for pressure a general method must be implemented to solve for the pressure in all flow situations.

The Semi-Implicit Method for Pressure-Linked Equations (SIMPLE) is currently implemented. This method consists of an iterative procedure which handles the non-linearity of the momentum equations along with the missing pressure equation. The iterative process takes a guessed initial condition and directs it toward the correct solution with use of the mass continuity equation.

In order to provide a general solver Fluent implements a co-located SIMPLE technique which avoids “pressure-velocity checkerboarding” while still allowing for use of unstructured grids. A full derivation of the SIMPLE algorithm is presented by (Versteeg and Malalasekera, 1995) and (Patankar, 1980).

2.1.7 Solver

The solver in Fluent is an Algebraic Multigrid (AMG) segregated solver. This is a relatively complex process and only the basic methodology and reasoning will be presented here. For an in depth mathematical description, refer to Fluent manual (2005).

Multigrid solvers such as AMG are comprised on the idea of iterating over the fine grid, then coarsening the mesh and iterating again, before finally iterating a last time on the fine grid. Internal iterations consist of a forward and backward sweep of a point by point Gauss Siedel linear solver. It is known that reduction of error in a point by point process takes a significant amount of time. By coarsening the mesh, there are then fewer cells to iterate over and the error is thought to diminish much more quickly. Overall, the multigrid solver accelerates the convergence by computing corrections on a series of coarser grids.

With an understanding of the basic iterating process, the methodology on a larger scale is covered by the segregated solver. It is apparent that the segregated solver was specifically designed to deal with the problems involving pressure velocity coupling. The segregated method consists of sequentially solving the momentum equations to first obtain the velocities, then the pressure corrections are obtained and the solution is updated. At this point any additional equations (e.g. turbulence) are solved sequentially. This process is repeated until convergence is achieved.

2.1.8 Meshing

Mesh creation is one of the most challenging aspects of CFD. It is essential to create a mesh which captures all physics of the flow while avoiding excessive computational time.   In general, each mesh is case dependent and configured for a specific geometry and flow. To ensure grid quality a mesh independence study is completed for general configurations studied in this thesis. This process entails refining the mesh to a point where the solution is independent of the grid.

Computational meshes may use structured or unstructured grids. Structured meshes consist of quad or hex elements which are applicable for simple geometries and provide added control of the mesh. Due to the simplicity of the geometries studied, all meshes implemented will be of a structured nature. Unstructured meshes would only be necessary with complex geometries.

The most important mesh region is the boundary layer near a solid surface. In laminar simulations the boundary layer must be resolved. However, in the turbulent case, the boundary layer may be resolved with the near wall approach or modeled using wall functions.

The near wall approach refines the flow into the viscous sub layer. Although this is the most accurate approach it may yield excessive mesh sizes with complex geometries or high speed flows. Most computational programs including Fluent define a non-dimensional distance from the wall, y^+. This distance is defined as,

$$y^+ = \frac{\left(\rho y \sqrt{\frac{\tau_w}{\rho}}\right)}{\mu}, \tag{2-11}$$

where ρ, μ, τ_w, and y represent the density, viscosity, wall shear stress, and distance to wall adjacent cell. For an accurate near wall mesh the grid should be refined to $y^+ < 5$. This non-dimensional distance will put the first cell well within viscous the sub-layer.

The majority of meshes created for aerodynamic flows use the low-Reynolds Spalart-Allmaras turbulence model which integrates to the wall with the near wall approach. Jet studies also take advantage of the near wall approach with the use of damping functions on the high-Reynolds k-ε model.

In any situation where resolution of the viscous sub-layer is unattainable, wall functions may be used to allow a coarser mesh. There are many types of wall functions in Fluent, which are based on empirical data (Fluent, 2005) of the turbulent boundary layer. To maintain validity of the wall functions strong adverse pressure gradients and separated flow cannot be handled.

The empirical wall function or "law of the wall" is shown as,

$$u^+ = \frac{1}{k} ln(y^+) + C \approx 2.439 \ln(y^+) + 5.1 \tag{2-12}$$

where k and C are known constants and y^+ is the non-dimensional distance defined in Eq. (2-11) and $u^+ = u/(\tau_w/\rho)^{1/2}$. Wall functions are valid when the non-dimensional distance from the wall lies in the following range, 30 < y+ < 300 (Wilcox, 2006).

2.1.9 Convergence Criteria

In order to find a solution with a numerical method, the variables of interest must converge to a unique finite solution. It is relatively common to monitor convergence by tracking residuals of the transported properties. The solution is said to be converged when the value of these transported values seize to change significantly. In the current study the scaled residuals of the transported properties are monitored with the convergence criteria set to 10^{-10}. Generally the residuals will converge before this point but setting such a small criteria ensures that convergence does not occur prematurely.

In addition to monitoring the scaled residuals, specific quantities of interest are also monitored throughout the solution. In the case of an airfoil, the lift and drag coefficients are also monitored for convergence. There are many cases where the important forces of interest may converge before the residuals, or may not converge at all. Therefore, convergence in the current research is assumed when both the residuals and forces of sufficiently converged.

When completing transient simulations the residuals are required to drop a couple orders of magnitude during each time step.

2.2 Validation

In order to numerically analyze ground effect aerodynamics, an understanding of the numerical capabilities is first necessary. As explained earlier, the software Fluent 6.3 has been used for all analysis. To ensure meaningful results a validation of jet behavior and aerodynamic force predictions with Fluent is completed.

2.2.1 Unbounded Two-Dimensional Airfoil

Predictions of aerodynamic forces out of the ground effect are first studied in Fluent with a two-dimensional, steady, incompressible, NACA 4412 airfoil. The NACA 4412 airfoil has been chosen as it is commonly used for WIG analysis (Barber et al., 1998) because of its nearly flat bottom surface which prevents creation of a venturi nozzle between the airfoil and the ground (Steinbach and Jacob, 1991). The out of ground effect (OGE) geometry is shown in Fig. 2.2. The additional 60° flap at x/c = 0.8 will be used for flap validation in section 2.2.2. All non-dimensional force, moment, and pressure coefficients used are defined in Appendix A.

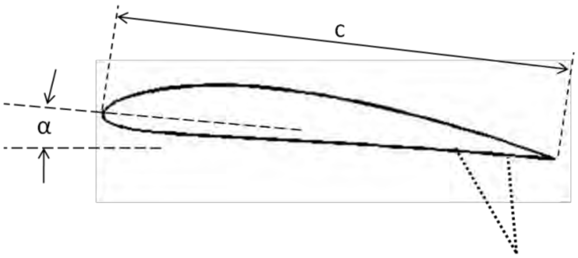

Fig. 2.2: NACA 4412 airfoil geometry.

The computational domain size was chosen such that the effects of the airfoil become negligible at the boundaries. This means that all external boundaries can be thought of as free-stream conditions. Studies have determined domain size independence with a circular upstream domain with radius of 12.5 chords, and a downstream boundary extending 20 chords past the trailing edge.

With a proper domain size, the physical scenario can be modeled using the boundary conditions shown in Fig. 2.3. The upstream boundary is specified as a uniform velocity inlet. This is the accepted upstream condition for aerodynamic applications (Barber et al., 1998), (Firooz and Gadami, 2006) as it defines the uniform forward speed of the vehicle. The upper and lower boundaries were also specified with the velocity inlet boundary condition. With the appropriately large domain size, the extremity flow is not affected by the airfoil, and this assumption becomes accurate. Although the top and bottom domains are modeled with a velocity inlet, with the significantly large domain, the symmetry or slip wall boundaries yield nearly identical results. Where the symmetry condition applies flow symmetry about boundaries while the slip wall defines a solid wall boundary with zero shear stress (fluid does not stick to the wall as it does in the common viscous no-slip wall boundary condition).

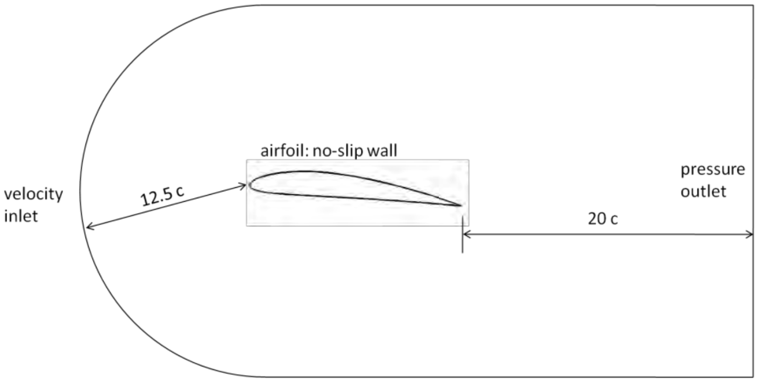

Fig. 2.3: Flow domain with boundary conditions specified.

The downstream edge of the domain is modeled with a constant pressure boundary condition at the atmospheric pressure. This condition is used often in aerodynamic flows (Barber et al., 1998) and is physically realistic as all large pressure changes dissipate within a few chords of the airfoil. Although the outflow condition is used by many researchers it will be avoided in the current research as it assumes fully developed flow leaving the domain. This decision has been made to provide consistency between current validation and complex flows studied in later chapters. Lastly, a smooth no slip wall condition is applied along the airfoil surface. This domain has been meshed with the structured c-mesh grid shown in Fig. 2.4. The near wall technique has resulted in a fine mesh containing 281,223 cells.

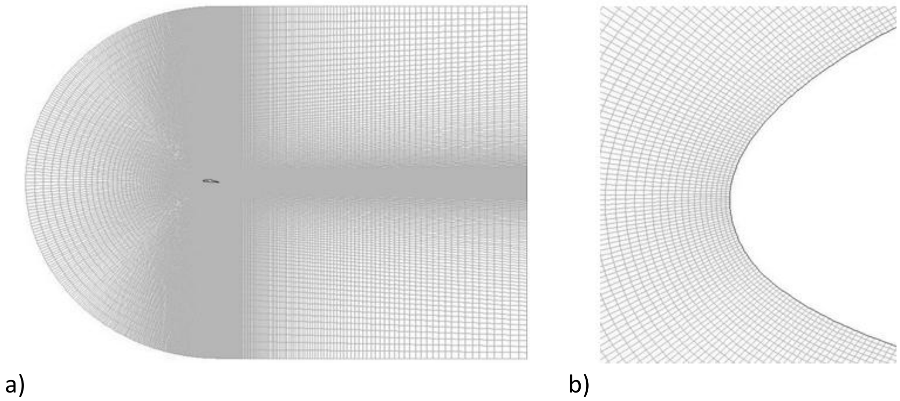

Fig. 2.4: Airfoil mesh: (a) full domain, and (b) nose refinement.

Practical ground-effect vehicles operate at sufficiently high Reynolds numbers, and therefore require modeling of turbulence. Although most configurations will have a small laminar flow region at the nose of the airfoil, this is generally negligible and Fluent forces the fully turbulent assumption. This may introduce errors with Reynolds numbers less than 10^6, generally in the form of a drag increase (see Appendix D). The RANS one equation Spalart-Allmaras turbulence model has been chosen (Spalart and Allmaras, 1991). The Spalart-Allmaras model is designed specifically for bounded aerodynamic flows and is discussed in detail in section 2.1.2.

The current OGE simulations were completed in Fluent 6.3. The Reynolds number was held constant at $6 \cdot 10^6$, corresponding to an incompressible flow regime ($M<0.3$). Standard air properties were taken for density and viscosity while the airfoil chord was fixed at 1 meter. During the analysis aerodynamic forces were obtained for angles of attack in the pre-stall regime between -4 and 12 degrees with a steady state assumption. All solution parameters are defined in Table 2.1.

density	1.225 kg/m^3
viscosity	1.7894e-5 kg/m-s
chord	1 m
grid size	281223 cells
solver	2D Steady
pressure-velocity coupling	SIMPLE
press. descretization	2nd Order
mom. descretization	3rd Order Muscle
mod. viscosity descretization	3rd Order Muscle
turbulence model	Spalart-Allmaras
Y+	0.5-3.5

Table 2.1: NACA 4412 solution parameters using near wall approach.

To ensure mesh quality, a mesh independence study was completed for the near wall method which resolved the viscous sub layer (refer to section 2.1.8). This study consisted of successively refining the mesh until the aerodynamic forces, lift and drag, ceased to change. As shown in Figure 2.5, the solution becomes mesh independent with 250,000+ cells where the mesh uncertainty is 0.36% for lift and 0.44% for drag (Roache, 1997). The estimated converged solution was found using extrapolation (Ferziger and Peric, 1999). Overall, we can see that this independence study provides validation in the quality of our mesh at 250,000 cells.

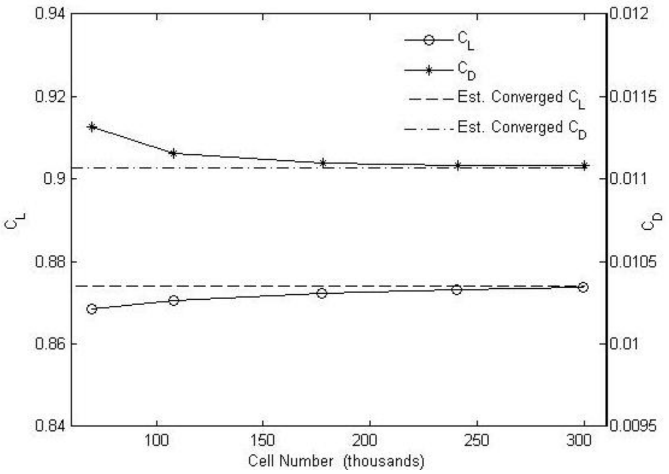

Fig. 2.5: NACA 4412 mesh independence study using near wall approach ($\alpha = 4°$ & $Re = 6 \cdot 10^6$).

Using the numerical techniques explained above, the results of lift coefficient with angle of attack are shown in Fig. 2.6a. As theoretically expected, the lift increases with increasing attack angle. Good agreement is shown between the modeling and experimental wind tunnel data (Abbott and Doenhoff, 1959) at low and medium attack angles. As the airfoil approaches stall, at 13-14°, a deviation from the experimental data begins to appear. Numerical difficulties near the point of stall are common in CFD techniques and are generally attributed to over predicted turbulent viscosity damping out separation. In addition, wind tunnel experiments also show development of three-dimensional effects in the stall regime (Rumsey and Ying, 2002) which cannot be predicted with our two-dimensional model. Fortunately, ground-effect vehicles generally do not operate anywhere near stall, so validation of pre-stall regime is sufficient.

Lift coefficients from similar numerical models (Firooz and Gadami 2006, Barber et al. 1998, Chun and Chang 2003) have also been compared to the current data. Clearly the numerical model also agrees well with other numerical techniques. We can conclude that our modeling techniques accurately predict lift forces in the pre-stall regime (OGE).

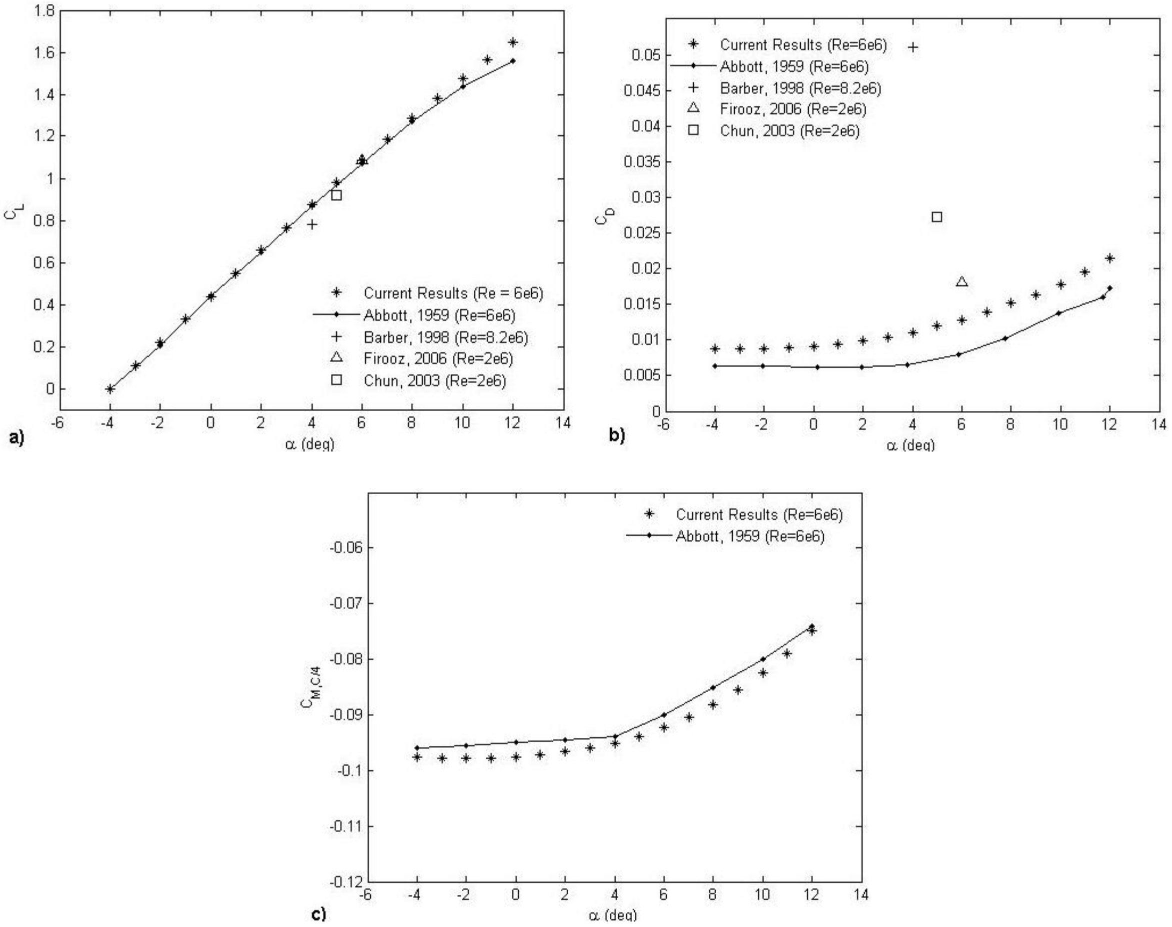

Fig. 2.6: Experimental validation of NACA 4412 with Re = $6{\cdot}10^6$: a) lift coefficient; b) drag coefficient; c) quarter-chord moment coefficient.

The drag coefficient was computed against angle of attack in Fig. 2.6b. As theoretically expected, the drag increased with increasing attack angle. However, the current numerical results appear to over predict the experimental drag coefficient (Abbott and Doenhoff, 1959) for all angles of attack. Overall, we predict the correct behavior but absolute value of forces predicted are shifted by a nearly constant increment.

Numerical data points of Firooz and Gadami (2006), Barber et al. (1998), and Chun and Chang (2003) are again shown in Fig. 2.6b. Among the numerical models, our method predicts drag most accurately; however, all numerical techniques over predict this force. In general CFD (Computational Fluid Dynamics) is known to be relatively inconsistent and sometimes inaccurate when predicting aerodynamic drag forces. This topic is discussed in detail in Appendix D. With the poor quantitative prediction of drag forces it is concluded that the current modeling can only be relied upon for drag trend prediction as absolute values are questionable.

Figure 2.6c compares the quarter chord moment coefficient between current modeling and wind tunnel tests. The airfoil is observed to have a nose down pitching moment as expected. The numerical results compare closely to wind tunnel data (Abbott and Doenhoff, 1959). Similar to the lift coefficient behavior, the moment coefficient is predicted well at low to medium angles of attack, while beginning to deviate near stall.

Lastly, the pressure distribution is calculated over the airfoil surface as shown in Fig. 2.7. The current numerical data closely matches the experimental data of Stack et al. (1939). Small deviations are visible in the pressure distribution at the suction peak. These deviations are expected near the nose of the airfoil where a fully turbulent model is used for a potentially laminar region near the nose at the given Reynolds number. However, the bottom (pressure) side of the airfoil matches the experimental data nearly perfectly. With the acceptable prediction of the lift coefficient and pressure distribution it is clear that Fluent can successfully predict the pressures on the airfoil surface.

For additional validation of airfoil flight outside of ground effect refer to Appendix C. The more commonly studied NACA 0012 airfoil is compared here against several additional experimental and numerical studies in the literature. Data has been left out of the body of this thesis as it yields the same validation conclusions as that of the NACA 4412 study of this section.

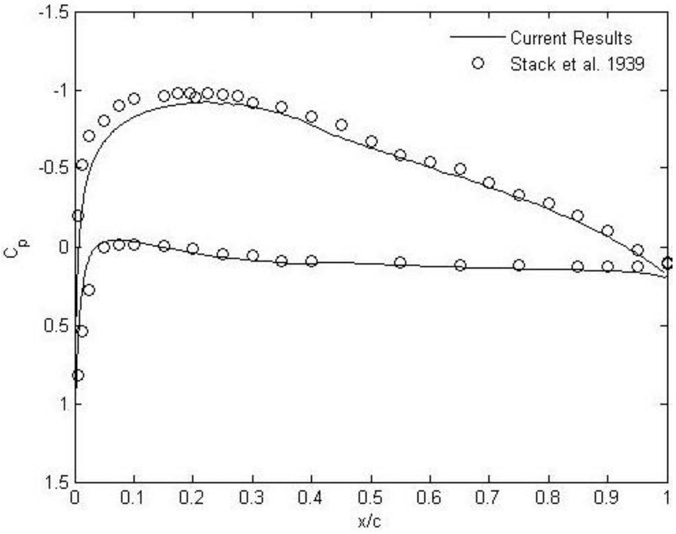

Fig. 2.7: NACA 4412 pressure distribution comparison at α = 1.875° and Re = $7.2 \cdot 10^5$.

2.2.2 Two-Dimensional Airfoil with Flap

Many ground-effect vehicles are designed to skim across water or a similar ground surface. In these cases the WIG effect is generally controlled with a flap at the trailing edge of the airfoil. By changing the flap position, the flow under the airfoil is controlled. This in turn controls the pressure under the airfoil and the airfoil lift. In many cases where ground height and angle of attack are relatively fixed, a flap can be used to adjust the lift of the vehicle.

With the flap being a common component in ground-effect vehicles, it becomes important to validate our modeling of flap implementation. This validation is provided by studying the flow over an NACA 4412 airfoil with a flap out of the ground effect. Figure 2.2 depicts the geometry used. The flap consists of a 60° wedge (from horizontal) which is added to the airfoil at 80% chord. The domain was meshed exactly as shown for the regular NACA 4412 with the exception of the added flap. A further refinement of the mesh was also completed near the flap and trailing edge of the airfoil, where recirculation was expected.

The flap analysis was again computed using Fluent with the similar parameters to those shown in section 2.2.1 including identical domain size and boundary conditions. The only difference being the added flap. Once again the aerodynamic forces were computed for several angles of attack. Figure 2.8a shows the comparison of the numerical lift coefficient to accepted experimental data (Abbott and Doenhoff, 1959) where lift at moderate attack angles is accurately predicted. As the angle of attack decreases to a small value or increases to a large angle the results begin to deviate. This deviation appears to be caused by the unsteady recirculation patterns which occur in these configurations, resulting in fluctuating aerodynamic forces.

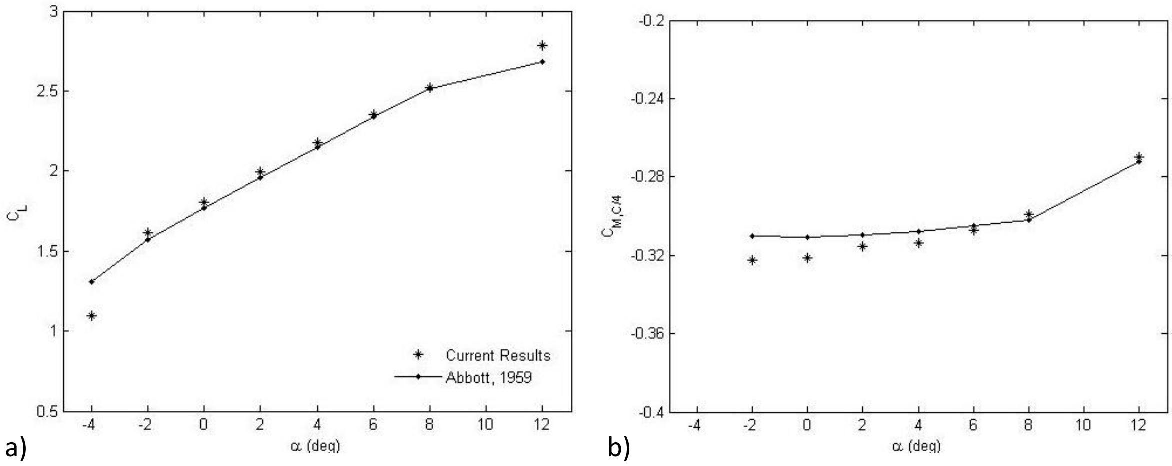

Fig. 2.8: NACA 4412 experimental validation with flap at Re = $6 \cdot 10^6$: a) lift coefficient; b) quarter-chord moment coefficient.

Figure 2.8b shows the variation of moment coefficient with angle of attack. Numerical and experimental data are quantitatively compared to within 5%. In addition, numerical and experimental trends (Abbott and Doenhoff, 1959) sufficiently agree in the range of attack angles studied. Deviation from experimental data are expected at large attack angles where unsteady flow patterns begin to present themselves For a better estimation of these values full unsteady analysis would be necessary at extremities to account for unsteady separation.

It is also of importance to understand the flow physics with an added flap. Previously, with no flap, the streamlined body provided a smooth flow over the airfoil until separation at large angles of attack. With the added blunt flap a significantly different flow is presented. Figure 2.9 shows the streamlines of the flow over the airfoil with added flap. With the blunt flap, for all attack angles, the adverse pressure gradient causes flow separation and a re-circulating wake downstream of the flap. The current steady state numerical model provides a good approximation of the aerodynamic forces with a flap in free air flow with medium attack angles. However, at extreme angles of attack, when the recirculation zone becomes unsteady, the aerodynamic forces cannot be correctly predicted. An unsteady analysis is necessary to accurately predict the aerodynamic forces in this regime.

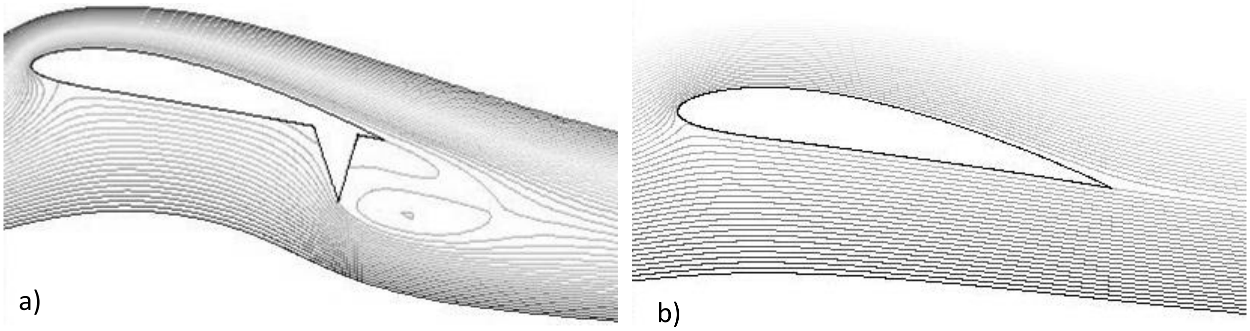

Fig. 2.9: Streamlines around NACA 4412: a) with flap; b) without flap.

2.2.3 Planar Turbulent Free Jet

In addition to the above airfoil studies it is also necessary to properly model planar jet behavior for applications such as the Power-Augmented-Ram vehicle. These ground-effect vehicles use the planar turbulent jet to provide jet induced lift. Therefore, modeling validation will be gained by studying the classical turbulent jet and comparing the performance against the wealth of theoretical (Rajaratnam, 1976) and experimental data (Gutmark and Wygnanski 1976, Bradbury 1965) in the literature. This setup has also been widely studied with numerical techniques, and has been used for turbulence model validation (Wilcox, 2006). Current numerical modeling techniques will be discussed, and results presented and validated against accepted empirical data found in the literature.

The current planar jet flow is governed by the steady two-dimensional, incompressible, constant viscosity, turbulent Reynolds Averaged Navier Stokes (RANS) equations, consisting of the continuity equation and the momentum equation, Eqs. (2-4) and (2-5).

The standard k-ε turbulence model provides closure for the Navier-Stokes equations with the Boussinesq approximation. This model solves two equations for turbulent kinetic energy, k, and turbulent dissipation, ε. For brevity the k-ε model is not shown here, however a detailed description is discussed in section 2.1.3. The k-ε turbulence model has been used because it is robust, computationally inexpensive, and has been validated for planar jet flows (Wilcox, 2006). In addition this model is commonly used in the literature (Anderson and Spall 2001, Nasr and Lai 1998, Guo et al. 2001, Kalita et al. 2002) and studies by Nasr and Lai and Guo et al. both recommend the k-ε model for engineering jet applications due to its low cost and ability to capture main steady and transient flow structures. The paper by Kalita et al. additionally shows successful application of the standard k-ε model for the planar turbulent jet in cross flow.

This closed set of governing equations is solved numerically. The Finite Volume Method (FVM) is used to discretize and linearize the governing equations. This set of algebraic linear equations is then solved by FLUENT 6.3. The segregated SIMPLE (Semi-Implicit Method for Pressure-Linked Equations) algorithm is implemented to modify the continuity equation into the needed pressure relation. The iterative nature of this procedure allows it to capture the non-linear nature of the physical situation while sequentially solving the governing equations. For the classical planar turbulent jet flow, a 2nd order discretization scheme is used for pressure while the second order upwind scheme is used for the momentum, kinetic energy, and turbulent dissipation.

The computational domain is setup to agree with the physical nature of the problem being studied. As shown in Fig. 2.10, the flow is inserted in the domain at the bottom left corner with a constant inlet velocity. The width of the jet, D, was chosen to be 6 cm with a constant inlet velocity of 2.447 m/s, corresponding to a jet Reynolds number of 10^4. The remaining boundary on the inlet wall is modeled with a no-slip wall condition. It is apparent by looking at Fig. 2.10 that only half of the jet is being modeled. This method is applied to take advantage of symmetry at the jet center, reducing the computational expense. Lastly, the top and downstream boundaries are modeled with Pressure boundary conditions to mimic standard conditions in a room.

The domain size of the current study was determined to be 117 jet widths downstream of the jet and 67 jet widths above the jet. This domain was then proven sufficient by increasing the domain by 50% with negligible changes in results. The domain size chosen is also very similar, if not larger, than other numerical studies of classical turbulent jet flows (Nasr and Lai, 1998).

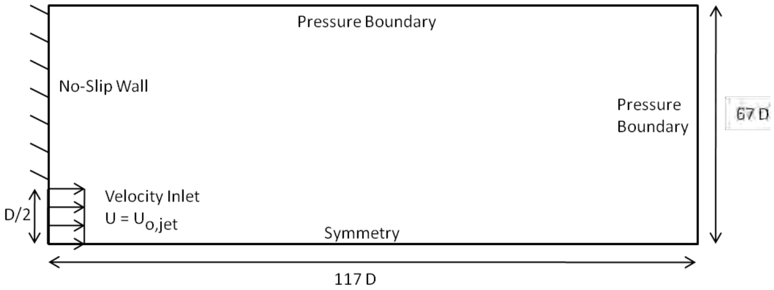

Fig. 2.10: Computational domain and boundary conditions for classic turbulent jet.

Meshes were created for the computational domain with a structured grid of quad elements as shown in Fig. 2.11. The mesh was refined in the jet region with further refinement along the mixing layer between the jet and the ambient fluid. The placement of this refinement region was determined based on the consideration of the common half velocity jet spread rate relation of 0.1x (Rajaratnam, 1976). All meshes created were developed to resolve the viscous sub layer on the inlet no-slip wall, having a wall adjacent cell non-dimensional height of y+ < 1, allowing the use of enhanced wall functions for the k-ε model. All of the above solution parameters can also be found for reference in Table 2.2.

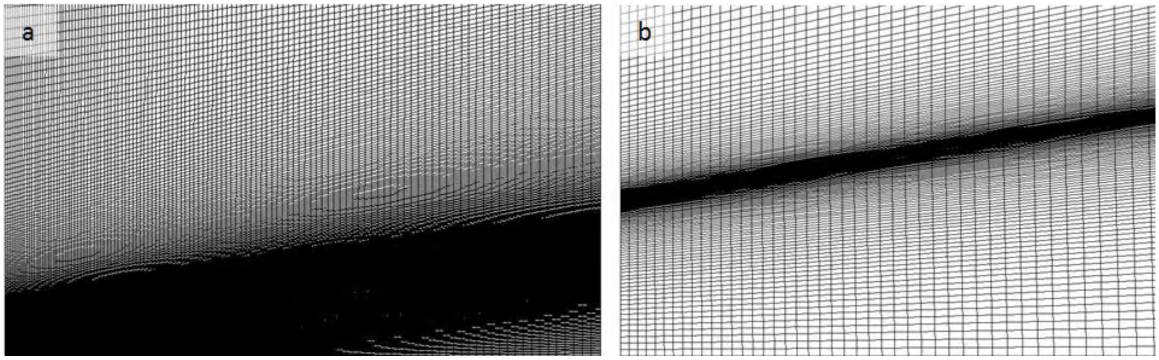

Fig. 2.11: Mesh of computational domain for two-dimensional jet: a) full domain; b) close-up of jet exit and mixing layer refinement on outer edge of jet.

density	1.225 kg/m^3
viscosity	1.7894e-5 kg/m-s
jet width	6 cm
Reynolds Number	10,000
grid size	57500 cells
solver	2D Steady
pressure-velocity coupling	SIMPLE
press. descretization	2nd Order
mom. descretization	2nd Order Upwind
mod. viscosity descretization	2nd Order Upwind
turbulence model	Standard k-ε
Y+	0.5-1

Table 2.2 Turbulent planar jet solution parameters using near wall approach.

A mesh independence study is first completed using centerline velocity profiles of the turbulent jet for comparison. Figure 2.12 shows the comparison between three different mesh densities. As theoretically expected all meshes show the correct trend of centerline velocity decaying in the downstream direction. This decay can be explained by the turbulent mixing of the jet, entraining flow and transferring momentum from the jet centerline to the extremities of the jet. It is apparent in Fig. 2.12 that all mesh densities yield nearly identical centerline velocity profiles, meaning that mesh independence has been achieved. All jet studies will use mesh densities comparable to the 57,500 cell mesh which provides a centerline mesh error of 0.34% at x/D = 20 and 0.091% at x/D = 60. Although the centerline velocity is not an integral property, the above errors (Roache, 1997) provide an approximate accuracy of the mesh. The use of this mesh will be used because it is dense enough to capture all flow behaviors while not containing an excessive number of cells.

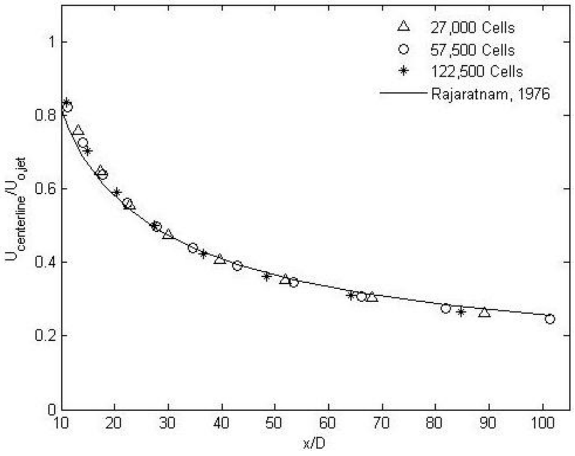

Fig. 2.12: Mesh independence study of centerline velocity at Re = 10^4 and D = 6 cm.

The non-dimensional centerline velocity profile presented in Fig. 2.12 also shows very good agreement with the accepted theoretical centerline velocity profile which is presented by Rajaratnam (1976),

$$\frac{U_{centerline}}{U_{o,jet}} = \frac{C_1}{\sqrt{\frac{x+C_2(D/2)}{(D/2)}}}, \tag{2-13}$$

where C_1 and C_2 are constants which have been found experimentally. The experimental range for C_1 has been found to be 3.12-3.78 while C_2 has shown to be somewhere in the range of 0-2.4 (Rajaratnam, 1976). Physically the $C_2(D/2)$ term is a position correction representing the distance from the jet nozzle to the virtual origin, where C_2 is positive when the virtual origin is behind the jet nozzle. The constant C_1 is an experimental coefficient which correlates to the spread rate of the jet. For Fig. 2.12 the values of C_1 and C_2 were chosen to be 3.5 and 0 respectively. Equation (2-13) has been derived for the fully developed flow region, so it is only valid after the potential core has dissipated at approximately x/D = 6.

Streamlines of the turbulent jet domain are shown in Fig. 2.13. As the jet exits from the bottom left corner it is shown to spread out as turbulence mixing occurs, pulling flow into the domain from the upper boundary and entraining it into the jet. This entrained flow is expected to enter the jet a nearly constant angle (Kotsovinos and Angelidis, 1991). However, we can see that near the downstream domain, the flow is shown to be pulled over the downstream boundary and is entrained into the jet in a much different manner than the majority of the domain. The flow in this range is obviously affected by the downstream boundary condition, and results for the flow over the last 50 widths of the domain will be neglected and only the section with constant entrainment will be studied. It should be noted that the areas to be studied for ground effect applications will focus on areas of x/D < 30 which falls within the valid region shown in Fig. 2.13.

Rajaratnam (1976) also presents radial velocity profiles obtained with the Tollmien and Goertler solutions which implement Prandtl's turbulent shear stress equations to solve the classical planar turbulent jet problem. The radial solutions obtained are shown to be satisfactorily represented by a Gaussian curve,

$$\frac{U}{U_{centerline}} = e^{\left(-C_3\left(\frac{y}{x}\right)^2\right)}, \qquad (2\text{-}14)$$

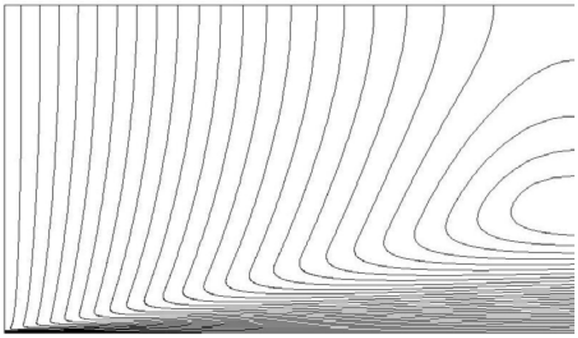

Fig. 2.13: Streamlines of planar turbulent jet at Re = 10^4, D = 6 cm.

where U represents the velocity in the downstream direction at radial distance from jet centerline y, with downstream distance as the sum of the distance from the nozzle to the point of interest and the virtual origin correction, $x_0 = C_2(D/2)$. C_3 is a constant which has been found experimentally to lie in the range 70.7-75. As with the equation for centerline velocity, Eq. (2-14) was derived for the fully turbulent flow outside of the potential core (x/D > 6). Experimental data for planar turbulent jets have shown that the radial self-similar velocity profiles do not develop until x/D ≈ 40 (Gutmark and Wygnanski, 1976). Figure 2.14 shows the non-dimensional radial velocity distributions for x/D = 20, 40, and 60. It is apparent that at all downstream locations the velocity decays from the centerline of the jet to the jet extremities. All curves shown are very nearly approximated by Eq. (2-14) with small deviations at the edge of the jet where the numerical results show a very small negative non-dimensional radial velocity instead of zero. Overall, the data shows that the jet profiles are self-similar for x/D = 40, 60, and nearly so for x/D = 20.

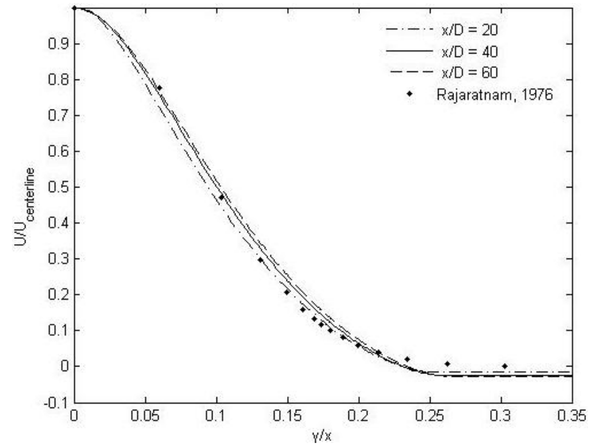

Fig. 2.14: Non-dimensional radial velocity distributions at Re = 10^4, D = 6 cm.

The jet thickness has also been compared to the experimental correlation presented by Rajaratnam (1976). Where the thickness presented is the distance from the jet centerline to the point where the radial velocity decays to half of the centerline velocity. Figure 2.15 shows how the current modeling correctly predicts the jet thickness/spread rate of 0.1x. This provides the final validation necessary to see that the classical jet modeling captures all physical structures of the jet and provides confidence in the numerical models ability to accurately predict the steady free jet flow.

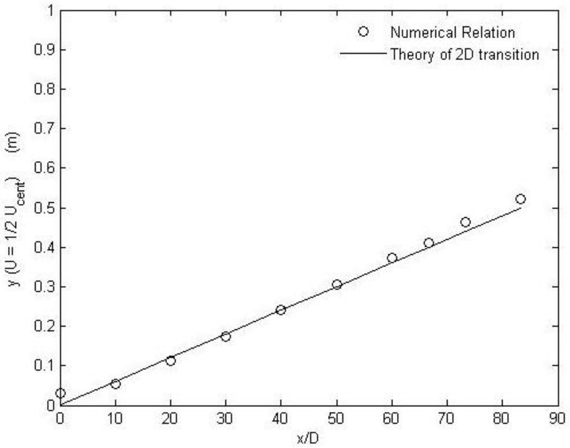

Fig. 2.15: Downstream spreading of turbulent classical jet at Re = 10^4, D = 6 cm.

With the implementation of the Boussinesq approximation to close the RANS turbulence model, information on the individual components of the Reynolds stress and the fluctuating velocities cannot be directly obtained in Fluent. Therefore, no validation has been completed for these fluctuating velocities in the x and y directions. This loss of information is relatively insignificant for the current studies, as only steady state solutions will be needed to capture the basic flow structures which will be necessary for design studies of ground-effect vehicles. However, where this data is needed, it may be determined by solving the definition of the

Boussinesq approximation (Eq. 2-6) with converged results from Fluent, yielding the converged Reynolds stresses field.

Overall, it has been shown that the numerical techniques used to study the incompressible turbulent planar jet flow agree very well with theoretical and experimental data. The knowledge gained will provide a baseline standard and structure for modeling techniques to use on other jet applications. At the same time, the theoretical solutions discussed will provide qualitative validation for future modeling methods.

2.2.4 Modeling Capabilities

Through the validation studies of the free-air NACA 4412 airfoil, confidence is gained in the aerodynamic load prediction capabilities of the current numerical model. Very accurate prediction of lift and moment coefficients are shown while the absolute drag value appears to be over predicted. In general, the drag trend is correct although magnitude is shifted by a nearly constant interval. Appendix D explains design techniques used to take advantage of the incorrectly predicted drag.

With the addition of a blunt flap, the aerodynamic forces were similarly predicted. The lift coefficient, with added flap, nearly identically matched the experimental wind tunnel results. The moment coefficient was also shown to follow the expected trend, although small deviations occurred at extremities where flow became unsteady. Overall, the steady method provides acceptable predictions at moderate attack angles where the flow separation region is statistically stable and no vortices are shed.

In addition, validation of the classical planar jet was presented in section 2.2.3 for the current numerical techniques. A mesh independent grid was first generated for the classical jet geometry, with the planar turbulent jet exiting from a solid wall into a free environment. The potential core length, jet centerline decay, radial self similar velocity profiles, and spread rate were shown to agree very well with experimental data (Rajaratnam 1976, Gutmark and Wygnanski 1976). Theoretical expectations of the jet were also obtained as jet entrained surrounding stagnant air and spread with axial distance. The excellent experimental agreement of the planar free jet provides validation in abilities of the numerical model to predict jet flow behavior with the k-ε turbulence model.

Overall, the numerical techniques explained and implemented in Chapter 2 have validated the modeling capabilities for accurate prediction of aerodynamic forces and planar jet behavior. It should be noted that the one disagreement between current modeling and experiments was that of the drag prediction. Although drag prediction is a general weakness of CFD (Appendix D), correct prediction of the drag force trends should provide sufficient validation for the ground effect parametric studies to be presented in later sections of this thesis.

CHAPTER THREE

WING-IN-GROUND EFFECT RESULTS

Thus far, methods for solving the flow around a standard airfoil with and without a flap in unbounded free flow have been validated (Ch. 2). The flow past an airfoil in the ground effect must now be considered.

The large numbers of viscous numerical and experimental studies of the NACA 4412 airfoil in ground effect (listed below) present an ideal case to validate the numerical techniques. Previous studies include a finite volume method employing the k-ε turbulence model by Hsiun and Chen (1996) with a fixed ground boundary condition. Where a decrease in lift was found in the extreme ground effect due to the boundary layer created along the fixed ground. More appropriate ground boundary conditions were then studied by Barber et al. (1998) who concludes that the fixed ground condition is unrealistic for WIG craft, and propose the use of a moving ground at the vehicle forward speed. A finite difference scheme with the Baldwin-Lomax turbulence model is implemented by Chun and Chang (2003) and presents significant differences in comparison of fixed and moving ground conditions. Firooz and Gadami (2006) then studied the same situation with the commercial code Fluent implementing the Spalart-Allmaras and Realizable k-ε turbulence models. All of the above numerical models using the moving ground boundary condition predict an increase in lift during ground-effect flight. Additional experimental WIG data for the NACA 4412 airfoil with fixed ground (Hayashi and Endo, 1978), and moving ground (Ahmed et al. 2006), (Kikuchi et al. 2002) setups have also been found in the literature.

With this, the viscous, incompressible, planar flow over an NACA 4412 airfoil in ground proximity will be studied. Ground effect parameters such as ground height, angle of attack, and Reynolds number will be varied to determine behavior of aerodynamic forces near the ground.

Comparisons of numerical results with published data will provide insight into ground effect behavior, WIG modeling capabilities, and proper boundary conditions.

3.1 Numerical Model

Once again the governing equations consist of the two-dimensional, incompressible, RANS equations given by Eqs. (2-4) and (2-5). The standard properties of air are used. The pressure velocity coupling is completed using the SIMPLE algorithm. Momentum and turbulence parameters use a 3rd order MUSCL discretization scheme (Van Leer, 1979) while pressure uses a 2nd order discretization method. As in the airfoil validation cases, the Spalart-Allmaras turbulence model is used. For further information on the turbulence model refer to Chapter 2. The overall Fluent WIG solution parameters are shown in Table 3.1 for solutions with near wall techniques applied.

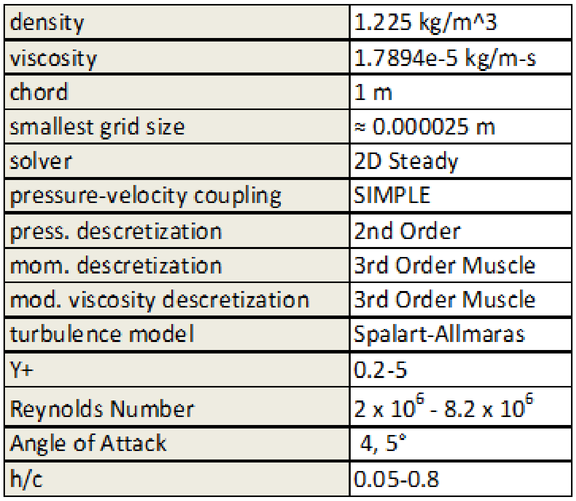

density	1.225 kg/m^3
viscosity	1.7894e-5 kg/m-s
chord	1 m
smallest grid size	≈ 0.000025 m
solver	2D Steady
pressure-velocity coupling	SIMPLE
press. descretization	2nd Order
mom. descretization	3rd Order Muscle
mod. viscosity descretization	3rd Order Muscle
turbulence model	Spalart-Allmaras
Y+	0.2-5
Reynolds Number	$2 \times 10^6 - 8.2 \times 10^6$
Angle of Attack	4, 5°
h/c	0.05-0.8

Table 3.1: WIG solution parameters with near wall approach.

The Wing-In-Ground geometry is presented in Fig. 3.1. Due to its nearly flat bottom surface and wealth of numerical and experimental WIG data, the NACA 4412 airfoil is studied. Aerodynamic coefficients resulting from changes in ground height, h, are the interest of the current study. As shown in Fig. 3.1 the ground height is defined as the distance from the ground to the trailing edge of the airfoil and the chord, c, is the length from leading to trailing edge of the airfoil. The attack angle is measured between the ground plane and line passing through leading and trailing edges of the airfoil. Lastly, the free stream velocity is U and the quarter chord moment coefficient is taken with respect to the location a quarter-chord downstream of the airfoil leading edge. Definition of all force, moment, and pressure coefficients used in Chapter 3 can be found in Appendix A.

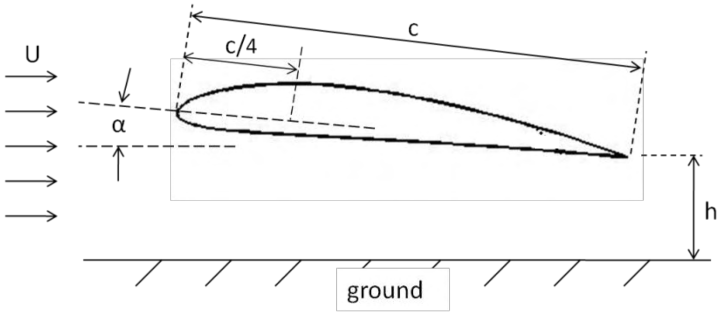

Fig. 3.1: Wing-In-Ground computational domain.

The structured WIG mesh consists of two separate regions of quad elements. Initially a c-mesh surrounds the airfoil to provide an adequate mesh around the airfoil and to capture behavior at the pressure suction peak. Far from the airfoil an h-mesh is applied to set the majority of the cells perpendicular to the flow. All meshes have been created with the near wall approach in order to resolve the viscous sub layer. Non-dimensional wall adjacent cell heights of $y+ \approx 1$ have been used to ensure that the meshes have properly resolved this layer. While using the low Reynolds number Spalart-Allmaras model the flow is integrated directly to the wall with this near wall approach (no need for wall functions).

Individual meshes for ground heights of h/c = 0.05-1.0 and varying angles of attack are created. Due to the different placements of the ground boundary, a separate mesh is required for each ground height and airfoil position. It is also important to understand that as the Reynolds number changes; the mesh will also need to be refined to account for the proper viscous sub layer. Figure 3.2 shows a mesh created for a ground height of h/c = 0.1.

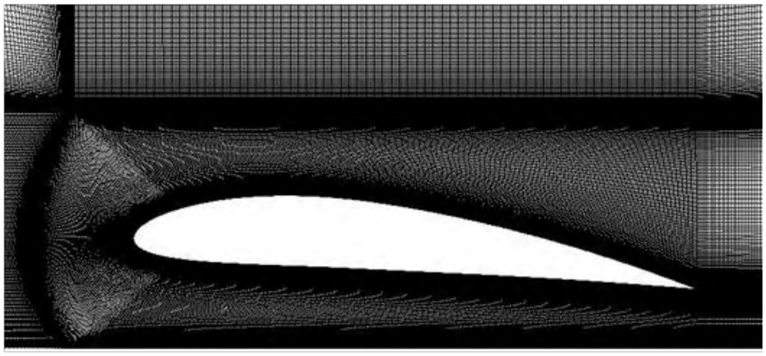

Fig. 3.2: Near wall mesh of NACA 4412 at h/c = 0.1.

The domains used extend 5 chords upstream of the airfoil, 12.5 chords downstream of the airfoil, 8 chord lengths above the airfoil, and the specified ground height below the airfoil. The domain size was chosen as it is similar, if not larger than the common WIG domain used in the references (Hsiun and Chen 1996, Firooz and Gadami 2006). The majority of the boundary conditions applied to the computational domain are exactly as stated for the free-air NACA 4412 analysis in Chapter 2. The one exception is the treatment of the ground underneath the airfoil.

Two separate boundary conditions were used for the ground underneath the airfoil. This condition was set as both a stationary no-slip wall and a no-slip wall moving at the free stream flow speed. The second condition is thought to be the most realistic situation as an aerodynamic vehicle in ground proximity moves past both the air and ground at the forward speed of the vehicle. A comparison of the boundary conditions will give an idea of what to expect when the incorrect boundary condition is implemented.

Lastly, in order to ensure that the aerodynamic forces are independent of the grid, a mesh independence study was completed. For brevity figures are not shown but it was found that with 400,000 cells the lift and drag coefficients yield a mesh independent solution with uncertainties of 0.08% and 0.47% respectively (Roache, 1997). Therefore, all meshes created for WIG flight use these metrics to ensure mesh independence.

3.2 Experimental Comparison

Before beginning a parametric study validation of the current model must be gained. Therefore, the study will begin with a comparison to the limited experimental WIG data available. Experimental WIG data for fixed ground (Hayashi and Endo, 1978), and moving ground (Ahmed et al., 2006), (Kikuchi et al., 2002) setups have been found in the literature. Unfortunately most experimental data found have been for flow of Reynolds number on the order of 10^5. At Reynolds numbers of this size, the flow is known to be laminar for a significant portion of the chord. With the turbulence models provided by Fluent, a fully turbulent flow assumption is forced. Therefore, at mediocre Reynolds numbers errors are expected in the numerical model.

Not only are low Reynolds ranges out of the current modeling capabilities, they are also well below the practical operating range of a Wing-in-Ground vehicle. Therefore, experimental data by (Ahmed et al., 2006), and (Hayashi and Endo, 1978) will not be compared due to lack of validity. However the paper by (Kikuchi et al., 2002) presents experimental towing data for a Reynolds number of $8\text{x}10^5$. Although the flow is still not fully turbulent, a comparison with the fully turbulent numerical solution is shown in Figure 3.3 to compare trends in ground effect.

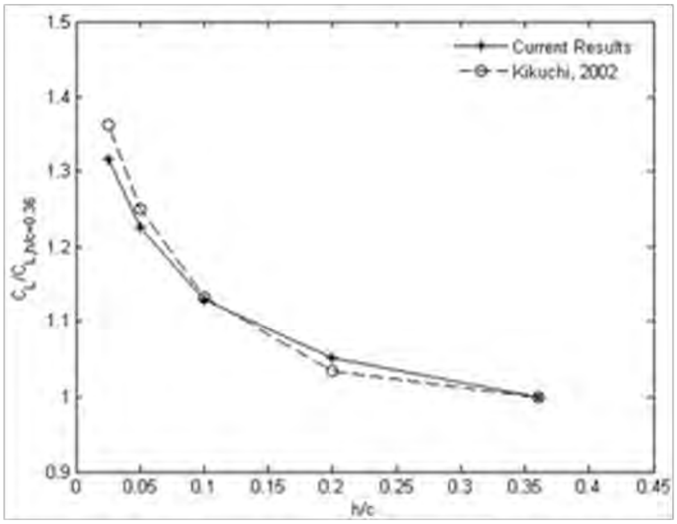

Fig. 3.3: Normalized experimental lift trend comparison in ground effect.

A normalized method is used to compare current numerical methods with experimental towing data for a Reynolds number of $8 \cdot 10^5$ and angle of attack of 6 degrees (Kikuchi et al., 2002) in Fig. 3.3. Each set of data uses its respective lift coefficient $C_{L,0.36}$ at the largest experimental ground height h/c = 0.36 for normalization. It should be noted that both experimental and numerical data become weakly dependent of ground proximity above h/c = 0.36, yielding approximate out of ground values. It is believed that the deviation between the two lines in Fig. 3.3 is a consequence of possible experimental uncertainties in outdoor towing tests and relatively small Reynolds number.

With this limited amount of experimental data, it is difficult to fully validate the modeling of an airfoil in ground effect. However, both experimental and current numerical results predict a lift increase as ground height is decreased. This represents the theoretical ground effect behavior and the good experimental comparison validates our WIG model within an uncertainty of about 5%. Although this leaves an element of error it is thought to be sufficient for the current design study. For a full validation of aerodynamic forces in ground effect a wealth of experimental data in the appropriate WIG range is required.

3.3 Numerical Results

With validation study complete, parametric studies are completed while varying ground height, Reynolds number, attack angle, and the ground boundary condition. The majority of results are for two WIG configurations which correspond to data of other numerical models which are discussed in the literature. The first of these configurations is an NACA 4412 airfoil at 5° angle of attack and a Reynolds number of $2 \cdot 10^6$ (Chun and Chang, 2003), (Firooz and Gadami, 2006), (Hsiun and Chen, 1996), while the second configuration consists of an NACA 4412 airfoil at 4° angle of attack and a Reynolds number of $8.2 \mathrm{x} 10^6$ as studied by Barber et al. (1998). Both of these configurations consist of common WIG parameters while comparisons between the two configurations may provide an idea of the effects of angle of attack and Reynolds number. The current results will be the focus of this study but discrepancies and differences with the referenced studies will also be discussed.

For both configurations, results were first found for the fixed ground boundary condition at ground heights of h/c = 0.8, 0.4, 0.2, 0.1, 0.08, and 0.05, where h/c corresponds to the ground height divided by the chord. Additionally, the same configurations were simulated with the ground boundary condition moving at the free stream velocity. For clarification, the experimental two-dimensional Out of Ground Effect (OGE) data of Abbott and Doenhoff (1959) is included on many of the figures in this Chapter for a reference to unbounded airfoil flight.

Figure 3.4 presents the lift trend of the current numerical procedures while varying the ground height. Figures 3.4a and 3.4c represent the two configurations with fixed ground boundary while figures 3.4b, 3.4d implement the moving ground boundary. For the cases with a fixed ground boundary, at large distances from the ground, the ground effect vanishes and flow similar to the unbounded case is shown. As the ground height decreases, increases in lift occur due to the entrapment of air between the airfoil and the ground (ram effect). However, with the fixed ground condition, a limit is reached in which this trend reverses and the lift begins to decrease. This behavior may be explained by a thick boundary layer which develops between the stationary ground and the moving fluid (Fig. 3.9). It is believed that the boundary layer reduces flow passing underneath the airfoil, yielding a lower flow of momentum which can be trapped between the airfoil and the ground. The critical ground height where the lift behavior reverses appears to reduce with increasing Reynolds number (boundary layer thins). In Figs. 3.4a and 3.4c current trends compare well with other studies at the given configurations (Barber et al., 1998), (Firooz and Gadami, 2006), (Hsiun and Chen, 1996).

When the moving ground boundary condition was implemented in Figs. 3.4b and 3.4d similar results were obtained. Once again the ground effect disappeared at large ground heights. As the airfoil approached the ground the lift again yielded an increasing trend. However, unlike the stationary ground, a large boundary layer is not created between the airfoil and the ground. This results in a continuous increase in lift with decreasing ground proximity with no trend reversal. In comparison of the two configurations it is apparent that the Reynolds number has little effect in cases without development of a boundary layer (moving ground). On the other hand, the increase in angle of attack from 4-5° appears to augment the lift similar to unbounded airfoil studies. Figures 3.4b and 3.4d show good agreement between current results and data in literature (Barber et al., 1998), (Firooz and Gadami, 2006), (Hsiun and Chen, 1996). Small deviations in the magnitude of the aerodynamic forces on the order of 5-10% are visible between numerical models. This scatter in previous numerical modeling data is not expected to lower the accuracy of our approach as we have already shown decent experimental comparisons.

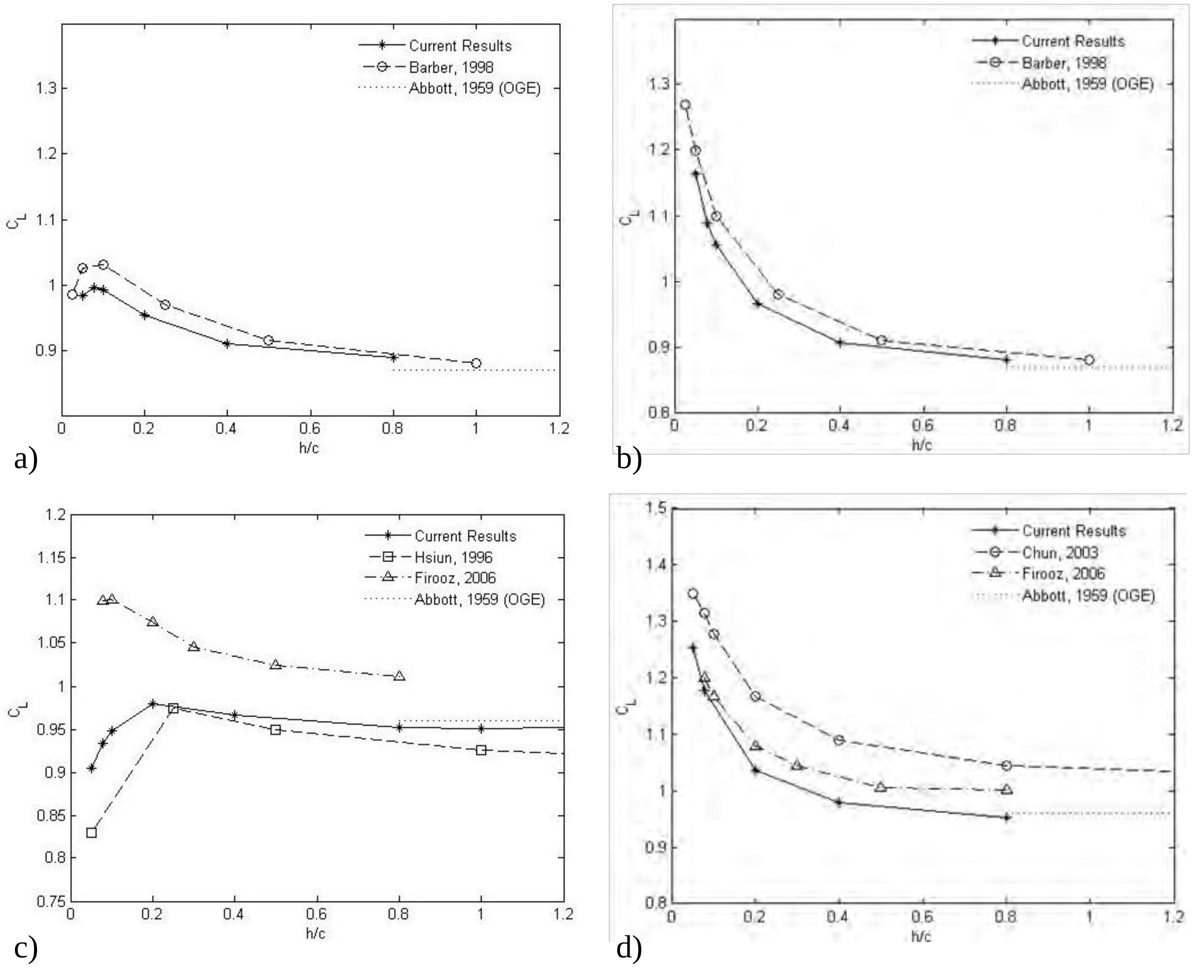

a)

b)

c)

d)

Fig. 3.4: C_L variation with Reynolds number and boundary condition: a) Re = $8.2 \cdot 10^6$, $\alpha = 4°$, fixed ground BC; b) Re = $8.2 \cdot 10^6$, $\alpha = 4°$, moving ground BC; c) Re = $2 \cdot 10^6$, $\alpha = 5°$, fixed ground BC; d) Re = $2 \cdot 10^6$, $\alpha = 5°$, moving ground BC.

The other aerodynamic force of interest, the drag, is shown in Fig. 3.5. The fixed ground boundary is represented in Figs. 3.5a and 3.5c while the moving ground boundary is represented in Figs. 3.5b and 3.5d. Again, the fixed ground boundary will first be discussed. In this case the results show a slight decrease in drag until extreme ground effect. It is thought that the decrease in this weak ground effect region is due to the slowdown of flow (lower viscous drag) before the significant increase in pressure at small ground heights occurs. As the extreme ground effect is realized it becomes apparent that the drag force begins to increase with decreasing ground height. This trend can be explained in terms of the pressure distribution. As the ground height decreases, the pressure drag will increase proportionally to the increase in pressure under the airfoil. This effect will contributed to the drag in all cases in which the airfoil is at a positive angle of attack where the bottom of the airfoil is not perfectly horizontal. With the fixed ground condition an interesting behavior is again shown in ground effect. This directly correlates to the decreased pressure under the airfoil at small distance. In this regime, as a result of the boundary layer, the pressure drag and hence the total drag is shown to decrease.

With a moving ground boundary condition implemented in Figs. 3.5b and 3.5d similar trends are visible. Again the drag slightly reduces as the ground is approached and the viscous forces diminish. Additionally, in the extreme ground effect, where the pressure increases sufficiently, the drag also begins to slowly increase. As was visible in the lift case, with this proper modeling no boundary layer is created and the unrealistic drag decrease is not visible in close ground proximity. It is relatively hard to determine effects of Reynolds number and angle of attack in this case as the drag has shown to decrease with increasing Reynolds number and decreasing attack angle. Both of these trends are expected and additional configurations will be necessary to determine which effect is more prominent in ground effect.

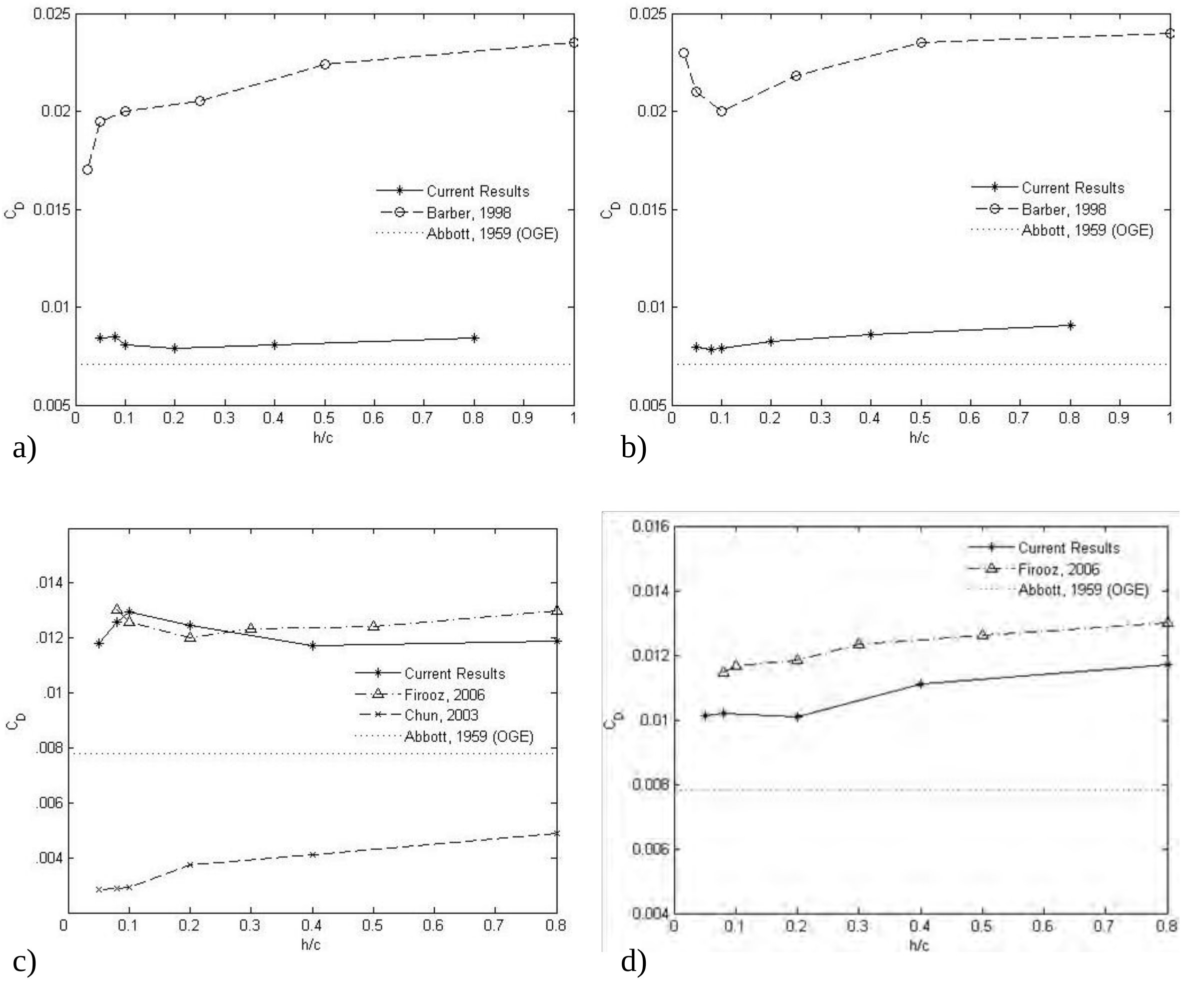

Fig. 3.5: C_D variation with Reynolds number and boundary condition: a) Re = $8.2 \cdot 10^6$, $\alpha = 4°$, fixed ground BC; b) Re = $8.2 \cdot 10^6$, $\alpha = 4°$, moving ground BC; c) Re = $2 \cdot 10^6$, $\alpha = 5°$, fixed ground BC; d) Re = $2 \cdot 10^6$, $\alpha = 5°$, moving ground BC.

It is apparent that in Fig. 3.5 the numerical drag data found in the literature is very erratic. Differences among cases with fixed ground conditions and unrealistic boundary layers will not be discussed further due to improper modeling. The moving ground data (Firooz and Gadami 2006, Barber et al. 1998) appears to match the current trend fairly closely. Similar to the drag validation in Chapter 2, we can see that trends are predicted fairly well, while the magnitude of the drag shows significant error. Some of these reasons are explained by the drag prediction difficulties in Appendix D. Even with the significant error in magnitude of drag, current prediction will be sufficient for determining the optimum vehicle positions which can then be studied further experimentally.

With an understanding of the aerodynamic forces in ground effect, we now have the information needed to determine the most important ground effect parameter, the aerodynamic efficiency. For Wing-In-Ground flight this is defined as the lift-to-drag ratio and its increase is the reason for flying in such close ground proximity. As presented above, in the ground effect an increase in lift coupled with a possible increase in drag is found. Thus the lift to drag ratio will provide a parameter which defines regions in which the ground effect flight will yield greater increases in lift, as compared the possible increases in drag. Figure 3.6 shows how the aerodynamic efficiency increases as the ground height decreases for the moving ground boundary condition. These trends are nearly identical to those of Firooz and Gadami (2006). From this figure we can conclude that the ground effect significantly increases the efficiency and holds promise for improving high speed flight. The data of Firooz and Gadami (2006) with a fixed ground boundary is shown for reference. As expected, the development of the boundary layer which reduced the lift in ground proximity will also reduce the efficiency.

At this point it should be noted that the span based ground effect is neglected in our current numerical model as the two-dimensional assumption approximates zero induced drag and no wingtip vortices.

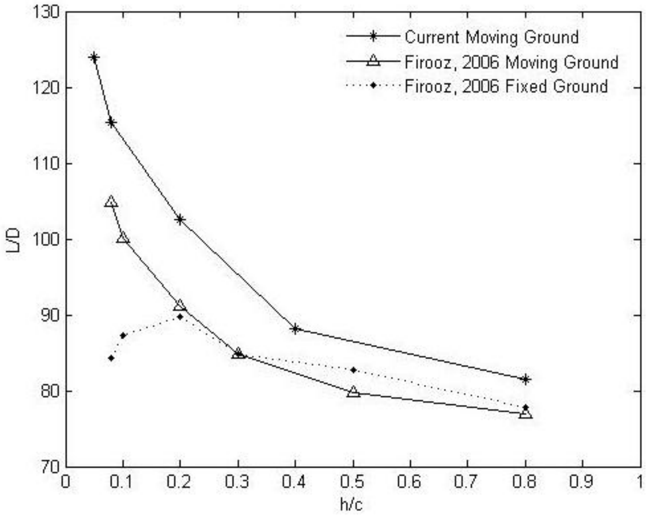

Fig. 3.6: Lift-to-drag ratio at $Re = 2 \cdot 10^6$ and $\alpha = 5°$ for moving ground BC.

A large amount of qualitative information on the aerodynamic forces can also be gathered by plotting the pressure distributions on the airfoil. Figure 3.7 shows the pressure distribution of the airfoil as it approaches the ground with moving ground boundary condition. Focusing on the pressure side of the airfoil, as the airfoil approaches the ground an increase in pressure under the wing occurs due to a slow down of flow. With the moving ground boundary condition, the large boundary layer isn't created, so the underside pressure increase is visible for all ground heights. Although the majority of the pressure increase in ground effect is underneath the wing, the lift also depends on the happenings on the suction surface of the wing. Above the wing an increased suction peak occurs as the wing approaches the ground. As explained by Chun and Chang (2003), the increase in the suction peak is due to the large escape of flow over the airfoil nose (as flow is blocked from passing underneath the airfoil). Ultimately the larger the area between the suction and pressure curves in Fig. 3.7 corresponds to a larger lift. So the moving ground boundary condition matches the theoretical expectation of a continuously increasing lift as the ground height decreases. A curve with the fixed ground boundary condition is presented to allow further understanding of the incorrect boundary modeling. It is apparent that the fixed ground condition does not achieve the pressure cushion underneath the airfoil or the suction peak at the nose. As reiterated above, this is due to the boundary layer developed in the fixed ground condition.

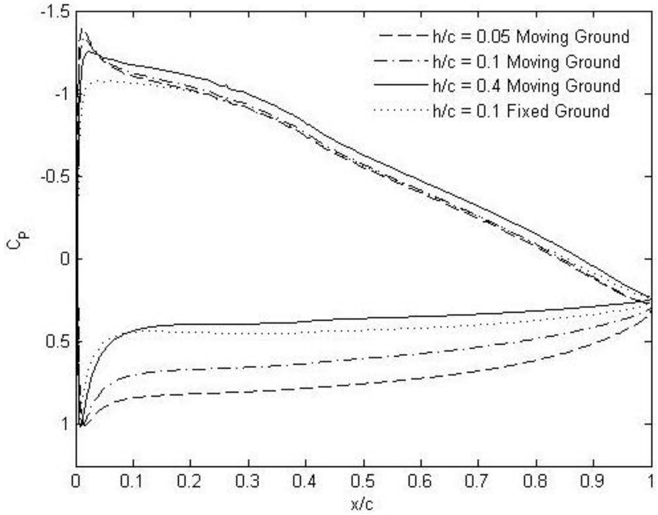

Fig. 3.7: C_P distribution at Re = $2 \cdot 10^6$ and α = 5° for moving ground BC.

For further investigations of attack angle, the flight in ground proximity was studied for Reynolds number of 10^6 and angles of attack of 2° and 6° with the appropriate moving ground boundary condition. Figure 3.8 illustrates the numerical results for lift and quarter-chord moment coefficients for the NACA 4412 airfoil. Similar to figure 3.4 the lift is shown to increase as the airfoil approaches the ground, and is plotted in comparison to the experimental out of ground solution at Re = $3 \cdot 10^6$. As the airfoil leaves the extreme ground effect near h/c = 0.3 this solution is approached. Figure 3.8b shows the quarter-chord moment coefficient, which shows an increase in nose-down pitching moment as the ground is approached. This behavior is explained by the increase in pressure underneath the airfoil creating the nose down moment.

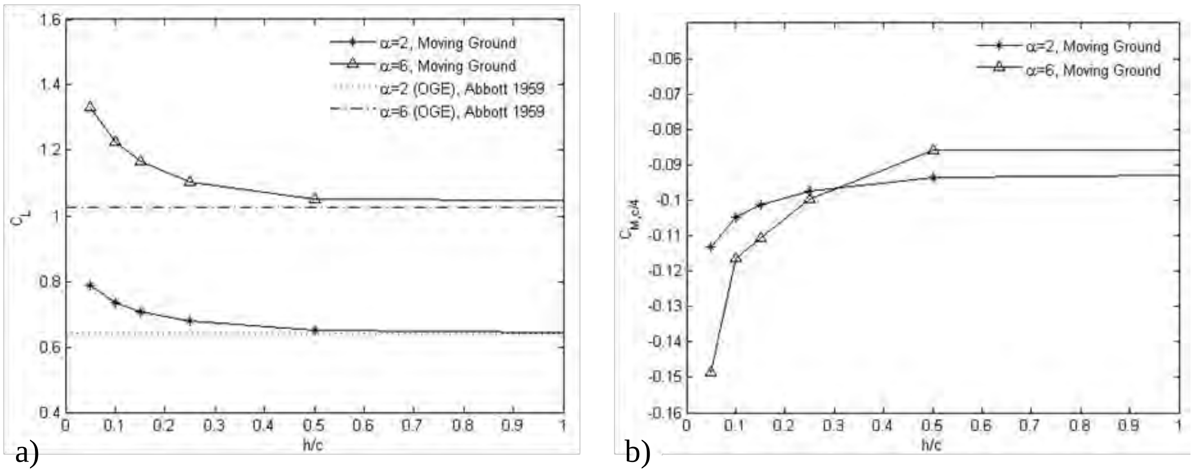

Fig. 3.8: Attack angle effects with moving ground at Re = 10^6: a) lift coefficient; b) quarter-chord moment coefficient.

With the comparison between α = 2° and 6°, further attack angle effects are presented. As expected, with a greater angle of attack, a larger lift is found. From the limited number of cases run, neither of the attack angles appears to augment lift significantly more than the other in ground effect. The nose down moment is also shown to increase with angle of attack in extreme ground effect. Again, in ground effect at larger attack angles the pressure increase simply acts against a larger vertical surface area, providing a greater nose down moment. However, out of ground effect where the forces on the airfoil are dominated by the suction above the airfoil instead of the pressure below, a reduction in nose down pitching moment is shown for larger angles of attack. This agrees with experimental data (Abbott and Doenhoff, 1959), and is expected in cases where larger angles of attack accelerates the flow over the nose, and produces a larger suction above the airfoil surface out of ground effect.

3.4 Ground Boundary Condition

An assessment of different ground boundary conditions presented above can now be discussed. Figures 3.4 and 3.7 show significantly smaller pressures and lifts with the fixed ground boundary condition. As reiterated above, this is attributed to boundary layer development with the fixed ground condition. Figure 3.9 provides a visual of the large boundary layer developed with the fixed ground boundary condition. This boundary layer stems from the velocity gradient between the no-slip ground and the free-flow. The boundary layer slows the flow near the ground, reducing the amount of flow passing under the airfoil, and yielding a decreased momentum and pressure under the aircraft.

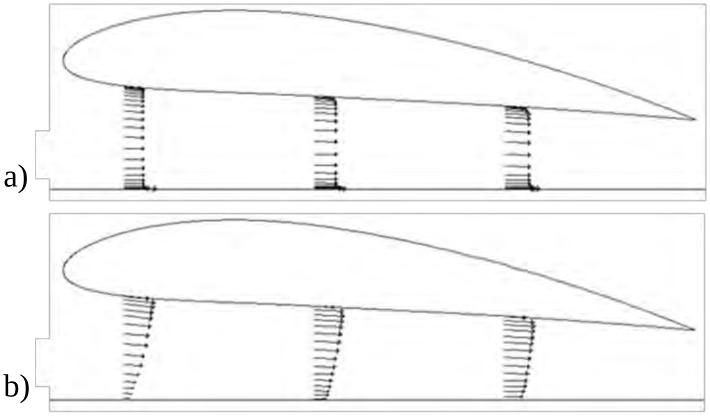

Fig. 3.9: Boundary layer development: a) moving ground boundary; b) fixed ground boundary.

Overall, Fig. 3.9 demonstrates the unphysical nature of the fixed ground boundary condition and confirms the necessity of the moving ground. Barber et al. (1998), Chun and Chang (2003), and Firooz and Gadami (2006) have all observed similar unrealistic behavior in ground proximity with a fixed ground boundary condition and made the same conclusion (necessity of moving ground). In all future aerodynamic studies in ground proximity the moving ground condition will be implemented to account for the realistic flow conditions.

3.5 Discussion

Trends predicted in the ground effect regions are similar to other numerical studies (Hsiun and Chen 1996, Chun and Chang 2003, Firooz and Gadami 2006) and support the claim that flight in ground proximity provides beneficial lift and aerodynamic efficiency. To obtain valid results the moving no-slip wall boundary condition should be used at the ground.

Effects of Reynolds number and attack angle are also found to be significant for several ground effect configurations. Similar to Hsiun and Chen (1996) we found that Reynolds number modifies flow structures in cases with fixed ground boundary conditions where a boundary layer has developed. However, with the moving ground condition the Reynolds number is shown to have little effects other than the well known drag reduction with increasing Reynolds number. The effects of angle of attack are very similar to those of the free air situation. The lift and drag forces increase as the attack angle is increased. Lift augmentation in ground effect appears to be similar for all of the moderate angles studied.

Although the trends of various experimental and numerical studies with moving ground condition match satisfactorily, the results of all numerical studies disagree on the magnitude of the aerodynamic forces in ground effect. It appears that most lift coefficients show a 1-10% variation, while the drag coefficients show a physically correct trend but are predicted differently with each code (Appendix D: Drag Prediction Difficulties). Although numerical differences have been noted, it is important to reiterate the fact that our model has been experimentally validated to within about 5% of experimental measurements. Overall, these comparisons in ground effect validate the ability to predict trends of aerodynamic forces close to the ground for design applications. For additional validation of the magnitude of forces in ground effect, a wealth of experimental data at a sufficiently high Reynolds number is necessary.

CHAPTER FOUR

WING-IN-GROUND BEHAVIOR WITH FLAP

Many WIG vehicles are designed to skim above water or a relatively flat solid surface. At low speeds or on heavily-loaded craft a flap is employed at the trailing edge of the ground-effect vehicle to strongly augment the airfoil lift. By adjusting the flap position, flow around the airfoil can be controlled, in turn providing control of the aerodynamic forces. In many cases where ground height and attack angle are relatively fixed, a flap can be used to regulate the vehicle lift in ground vicinity. It is thought that airfoil-flap configurations will also approximate PAR-WIG vehicles at high speeds where the jet support is unnecessary.

Little published research has been found for the use of a flap in the extreme proximity to the ground. Most studied configurations were complicated PAR systems (e.g., Huffman and Jackson 1974, Krause 1977, Thomas et al., 1979). However, Serebrisky and Biachev (1946) tested Clark-Y sections by the method of images in this region and found that use of flap in ground effect improves the aerodynamic efficiency for small angles of attack. The flap application has also been numerically and experimentally studied by Steinbach and Jacob (1991) in the distant ground effect, with height-to-chord ratios from around one quarter to above one. Their numerical technique consisted of a panel method, which was iterated with boundary layer and rear displacement models to account for viscosity and separation. They conclude that wing systems with excessive flap-slat mechanization are often unfavorable in the distant ground effect due to the large effective camber which produces a negative ground effect. Their results also show that as a high-lift airfoil with a flap approaches the ground, the flap efficiency decreases, and the separation point moves further upstream.

However, nearly flat lower airfoil surfaces and moderate flap deflections and attack angles are known to be quite beneficial in ground proximity (Serebrisky and Biachev, 1946). The goal of this Chapter is to investigate favorable trailing-edge flap configurations that improve aerodynamic efficiency of vehicles operating in the extreme ground effect, where the best aerodynamic properties are found. A numerical study of viscous ground-effect-flap flow is completed. The performance of plain and split flap configurations are compared for different ground heights, flap deflections, Reynolds numbers, and attack angles; ultimately providing a beneficial region of flap use for extreme ground-effect vehicles.

4.1 Numerical Model

For consistency the NACA 4412 airfoil is once again studied as it avoids the Venturi effect (Steinbach and Jacob, 1991). The NACA 4412 geometry with flap and main study parameters are shown in Fig. 4.1. The distance from the tip of the flap to the ground is denoted as h_f, while the distance from the trailing edge of the wing section with undeflected flap to the ground is defined as h. The difference between h and h_f represents the total flap deflection, which is denoted as y_f. The angle of attack is defined as the angle between the chord line connecting the leading and trailing edge of the wing without flap and the horizontal plane, while the quarter chord moment coefficient is found with respect to the location on the camber line one quarter of the chord downstream of the leading edge. Definition of all force, pressure, and moment coefficients used in Chapter 4 can be found in Appendix A.

In the current study, the flap is added to the NACA 4412 airfoil at 80% chord. Simple flap mechanizations are used in ground proximity because the extreme camber of high lift flaps produce a negative ground effect. The plain and split flaps are added to the NACA 4412 airfoil as shown in Fig. 4.2.

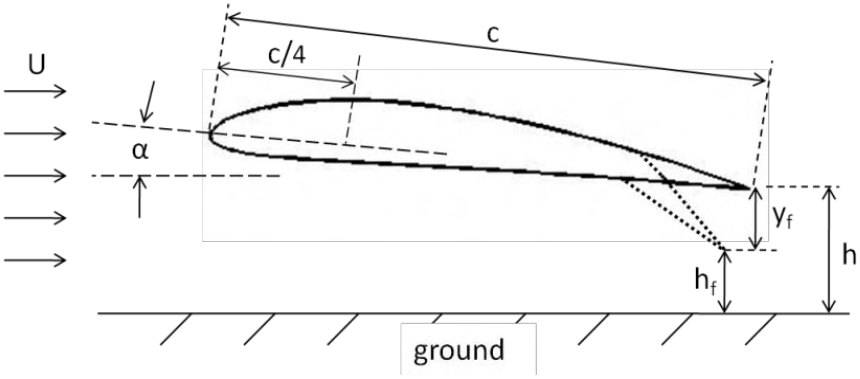

Fig. 4.1. Schematic for modeling airflow around NACA 4412 wing section with plain flap in ground effect.

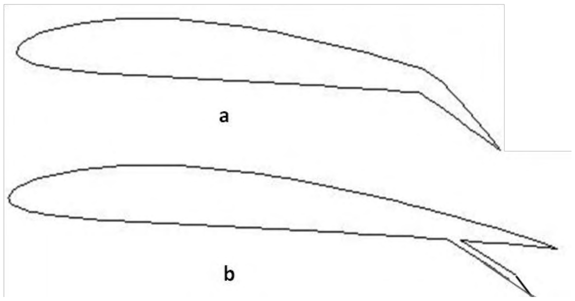

Fig. 4.2. Flap schematics for α = 6° and $y_f/c = 0.1$: a) plain flap; and b) split flap.

In the current simulations turbulent flow is specified over the entire airfoil, similar to other numerical ground-effect studies (e.g., Barber et al. 1998, Chun and Chang 2003, Firooz and Gadami 2006, Hsuin and Chen 1996). The general equations governing the current WIG flow with a flap are the two-dimensional, incompressible, constant viscosity, turbulent Reynolds Averaged Navier Stokes (RANS) equations, Eqs. (2-4) and (2-5). The Reynolds stresses that appear in the momentum equation are once again approximated with the Boussinesq assumption. Closure is provided to the Navier Stokes equations by implementing the Spalart-Allmaras turbulence model. As discussed in Chapters 2 and 3 this model has been implemented because it is computationally inexpensive and has been designed and validated for aerodynamic flows with adverse pressure gradients (Fluent, 2005). A detailed description of this model is given in section 2.1.2. The closed set of governing equations is solved numerically using the Finite Volume Method (FVM) with pressure velocity coupling accounted for with the segregated SIMPLE algorithm. The current research implements the 2nd order discretization scheme for pressure and the 3rd order MUSCL scheme for discretization of momentum and modified turbulent viscosity (Van Leer, 1979). All solution parameters and shown in Table 4.1.

density	1.225 kg/m^3
viscosity	1.7894e-5 kg/m-s
chord	1 m
flap type	Split, plain, or none
Attack angles	2° and 6°
Reynolds numbers	10^6 and 10^7
grid size	400-600 thousand cells
solver	2D steady / unsteady
pressure-velocity coupling	SIMPLE
press. descretization	2nd order
mom. descretization	3rd order MUSCL
mod. viscosity descretization	3rd order MUSCL
transient descretization	2nd order implicit
turbulence model	Spalart-Allmaras
Y+	0-3 (near wall)

Table 4.1. Wing-in-Ground solution parameters with flap implemented.

Generally, the use of a flap creates separation behind the airfoil. As this separation zone increases in size it can lead to unsteady effects such as vortex shedding. However, in most cases it has been observed that as the ground is approached, the separation zone behind the airfoil is limited by the presence of the ground, yielding a limited separation region which is statistically stable and can be studied with a steady-state RANS solution. However, some flap geometries studied yield unsteady effects which prevent convergence. For these cases, the Unsteady RANS

(URANS) equations are used with the Spalart-Allmaras turbulence model. The validity of this approach is acceptable as the turbulent time scales are far separated from the transient flow structures. Additionally, the unsteady flow structures will be shown to play a minor role. Provided only the time-averaged force coefficients are of interest, a complete resolution of the transient effects (e.g. LES) is unnecessary (Ferziger and Peric 1999, Spalart 2000).

The computational domain extends 5 chords upstream, 12 chords downstream, 6 chords above, and the specified ground height below the airfoil. This domain was chosen as it captured all important physical phenomena; and was similar, if not larger, than domains used in other WIG studies (e.g., Hsiun and Chen 1996, Firooz and Gadami 2006). Meshes created for this domain consist of two separate regions of quad elements. Initially a c-mesh surrounds the airfoil to provide an adequate mesh around the nose, while far from the airfoil an h-mesh is applied outside of the c-mesh to provide cells perpendicular to the flow. All meshes use the near wall technique and have been refined into the viscous sub layer, providing a first cell non-dimensional height of $y^+ \approx 1$. A mesh of the airfoil-flap system in ground effect is shown in Fig. 4.3.

The general boundary condition at the ground has been chosen as a moving wall at the free stream velocity. In Chapter 3 this condition was shown to provide a realistic model of the WIG flight, without introducing an unrealistic boundary layer at the ground. The upstream and top boundaries are modeled as velocity inlets at the free stream conditions, while the downstream boundary is defined as a pressure outlet. Lastly, the airfoil surface is modeled as a no-slip wall. A schematic of the computational domain reiterates the boundary conditions in Fig. 4.4.

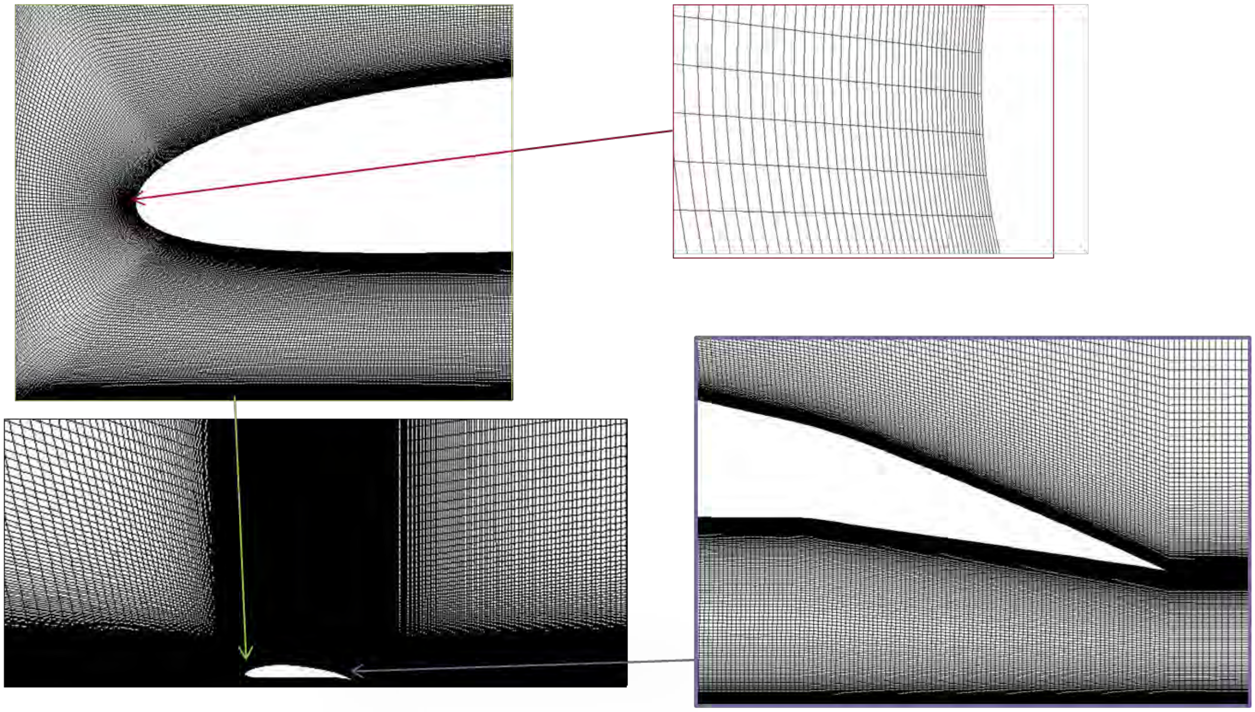

Fig. 4.3. Mesh for use of flap in ground effect with close up on nose, flap, and boundary layer regions.

In this Chapter, Reynolds number, based on the wing chord and incident flow velocity, is selected to be 10^6 for most situations, while Re = 10^7 is also investigated for a few cases. It is known that the dependence on Reynolds number above $5 \cdot 10^5$ becomes generally less significant and more predictable. Increasing Reynolds number above 10^6 in previous WIG studies has shown a minor increase in lift coefficient and more substantial decrease in the drag coefficient (Hsiun and Chen 1996).

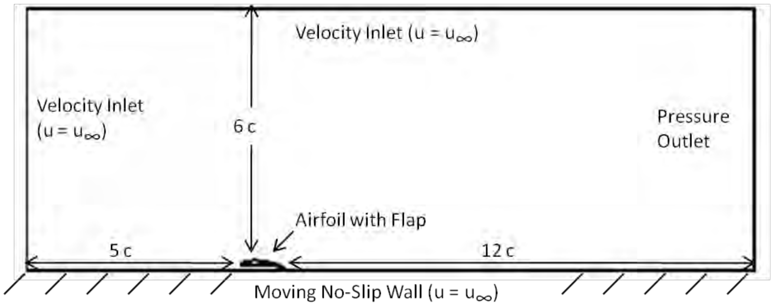

Fig. 4.4. Computational domain with boundary conditions listed.

4.2 Validation of Numerical Techniques

Mesh independence studies were first completed for ground effect flow with a flap. The aerodynamic forces became nearly independent of mesh with a density of 400,000+ cells with mesh uncertainties in lift and drag calculated as 0.2% and 0.27% respectively (Roache, 1997). All meshes strictly follow these metrics to ensure nearly mesh independent solutions.

Confidence in the current results is provided by the validations completed in Chapters 2 and 3. First, the NACA 4412 airfoil with and without a flap was studied out of ground effect (Chapter 2) for comparison to two-dimensional experimental (Abbott and Doenhoff, 1959) and numerical data (Barber et al. 1998), (Chun and Chang, 2003), (Firooz and Gadami, 2006), showing accurate prediction of aerodynamic lift and moment in the pre-stall regime while providing a drag trend which will suffice for the current design study. Additionally, ground effect modeling techniques were validated against experimental and numerical published data (Chapter 3), quantitatively predicting forces within 5% of experimental data.

With validation of our current modeling capabilities a final assessment of varying ground boundary conditions and turbulence models are presented with the addition of a flap in ground effect. Figure 4.5 shows the pressure distribution comparison between fixed, moving, and symmetry ground boundary conditions. It is apparent that compared to moving and symmetry conditions, the fixed ground boundary condition provides a significantly smaller pressure below the airfoil. As discussed in Chapter 3, this effect is due to a boundary layer created between the fixed ground and free stream flow, reducing flow beneath the airfoil and diminishing the pressure ram effect. Barber et al. (1998), Chun and Chang (2003), and Firooz and Gadami (2006) have all observed similar unrealistic behavior of flow in ground proximity with a fixed ground boundary condition. The moving ground and symmetry boundary conditions avoid the ground boundary layer and yield nearly identical results. However, the moving ground boundary condition is used as it most accurately represents the physical situation in ground proximity.

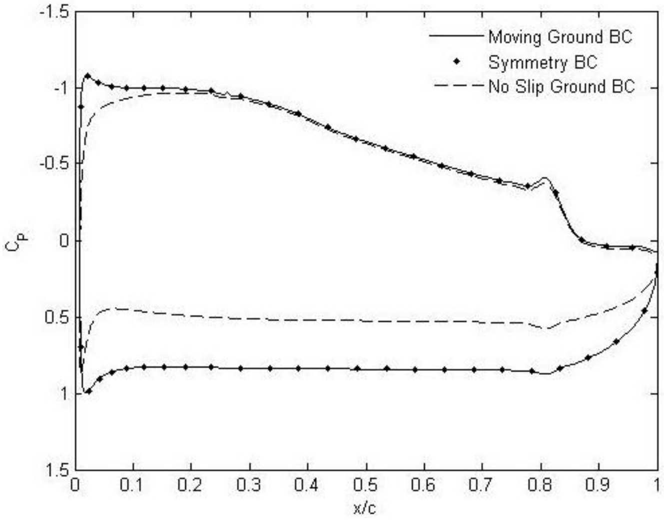

Fig. 4.5. Pressure distribution for various ground boundary conditions at $h/c = 0.1$, $h_f/c = 0.05$, $Re = 10^6$, and $\alpha = 2°$.

Similarly, Fig. 4.6 shows a comparison of pressure distributions for three different RANS turbulence models available in Fluent. The Spalart-Allmaras, k-ε Realizable, and k-ω SST models are all used to determine flow for a case with ground height of $h/c = 0.1$, flap height $h_f/c = 0.05$, $\alpha = 2°$, and Reynolds number of 10^6. All models similarly predict the distributions on the pressure side of the airfoil along with the suction peak above the airfoil. Variation can be seen on the upper surface of the flap where separation begins to occur. However, these variations are of a small scale and have little impact on the aerodynamic forces on the ground-effect vehicle. Therefore, as mentioned above, the Spalart-Allmaras turbulence model is used for all following simulations and other models are expected to behave similarly.

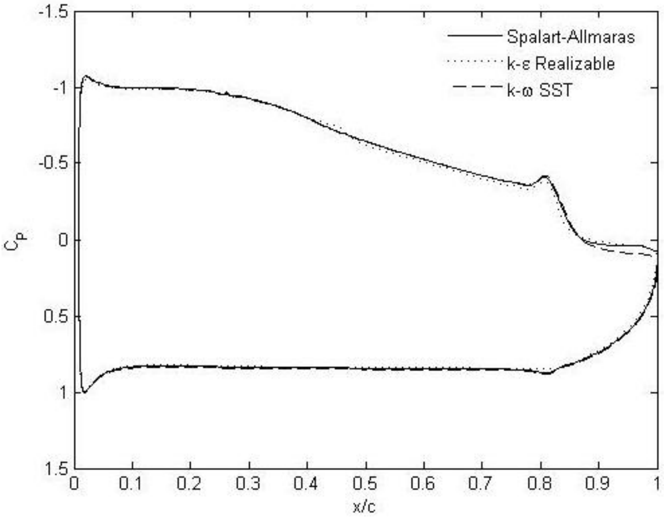

Fig. 4.6. Pressure distribution for various RANS turbulence models at $h/c = 0.1$, $h_f/c = 0.05$, $Re = 10^6$, and $\alpha = 2°$.

Overall, it has been shown that the current numerical techniques provide results that compare very closely to other numerical and experimental data for a variety of flow geometries. Validations of the turbulence model and boundary conditions have also been presented with the added flap to provide increased confidence in the numerical model.

4.3 Parametric Calculations

With the model validated, simulations were completed in order to study the effects of ground height, flap deflection, attack angle, Reynolds number, and flap type for extreme ground-effect vehicles with a trailing-edge flap. Non-dimensional ground heights of h/c = 0.05, 0.1, and 0.15 were studied for several flap deflections including the undeflected case and limiting case with flap touching the ground. The simulations have been repeated for the angle of attack 2° and 6° and Reynolds numbers 10^6 and 10^7. Most combinations have been run with a plain flap, while some selected cases at h/c = 0.05 and 0.1 have been repeated with a split flap for comparison.

The flow field is first shown in Fig. 4.7 with the velocity magnitude contours for the cases of h/c = 0.1 and h/c = 0.15 with $\alpha = 2°$, and Re = 10^6 while varying plain flap heights. Figures 4.7a, e show the airfoil without flap deflected, Figs. 4.7b, c, f, and g present intermediate flap heights, and Figs. 4.7d, h present the limiting case where the flap is touching the ground. As the flap is deployed, increasing amounts of flow are trapped underneath the airfoil, significantly reducing the flow speed in this region. With a reduction in the flow underneath the airfoil, larger amounts of flow are forced over the nose of the airfoil increasing the flow speed on the suction side. As the flap is deflected the stronger adverse pressure gradient on the upper side of the airfoil, coupled with the jet type flow through the diminishing gap at the trailing edge, leads to flow separation on the flap surface. In the limiting case when the flap touches the ground, all flow underneath the airfoil is trapped, creating a large recirculation zone and directing all incident flow above the airfoil. It is observed that as the flap is deflected, the recirculation zone grows on the upper surface of the flap until the limiting case where a large statistically stable recirculation region is created between the flap and the ground. Although only two ground heights (h/c) are presented, the velocity contours of all heights studied (in extreme ground effect) follow the trends mentioned above.

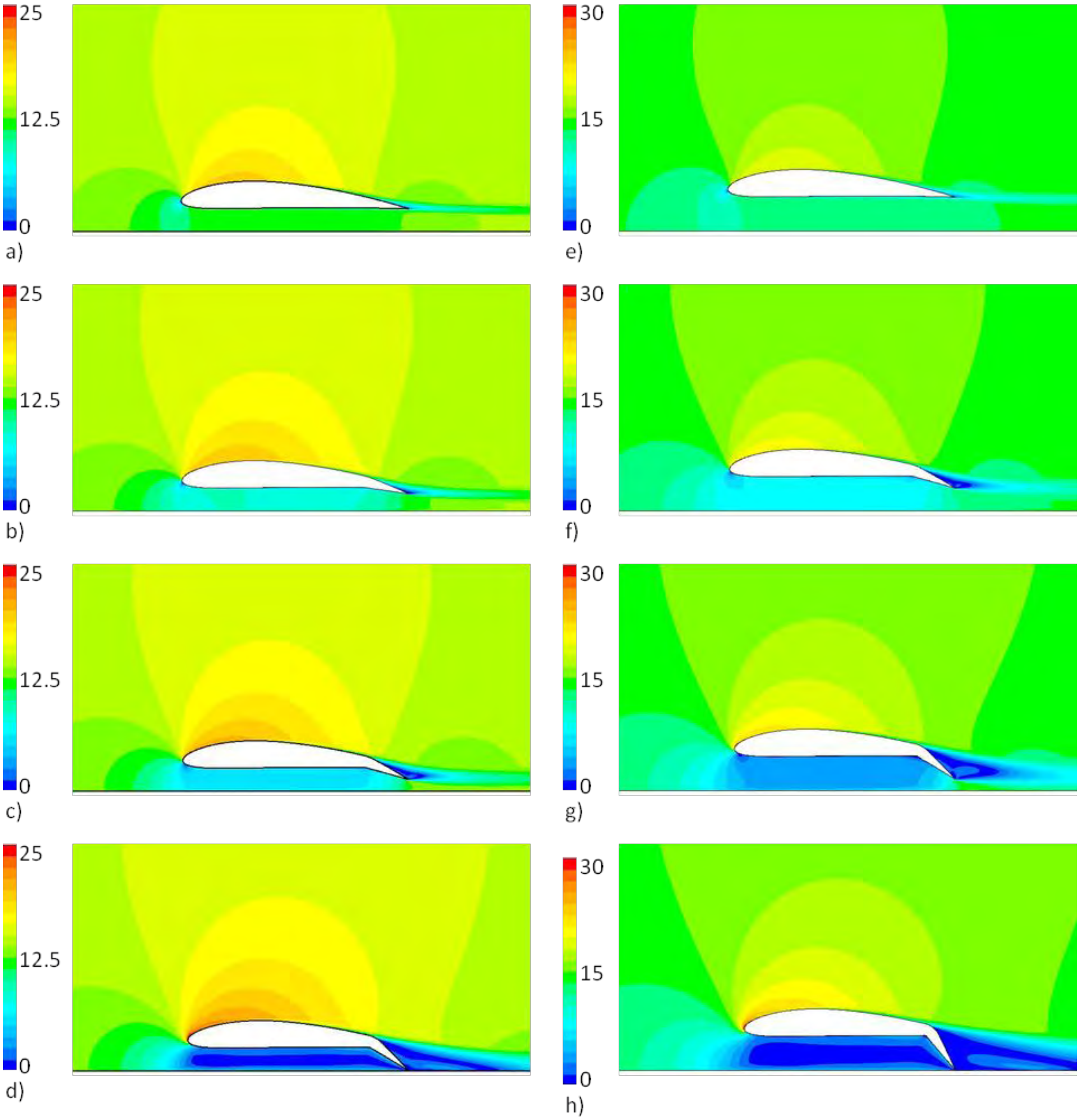

Fig. 4.7. Velocity magnitude contours (m/s) with α = 2° and Re = 10^6: a) $h/c = 0.1$ and $h_f/c = 0.1$; b) $h/c = 0.1$ and $h_f/c = 0.075$; c) $h/c = 0.1$ and $h_f/c = 0.05$; d) $h/c = 0.1$ and $h_f/c = 0$; e) $h/c = 0.15$ and $h_f/c = 0.15$; f) $h/c = 0.15$ and $h_f/c = 0.1$; g) $h/c = 0.15$ and $h_f/c = 0.05$; h) $h/c = 0.15$ and $h_f/c = 0$.

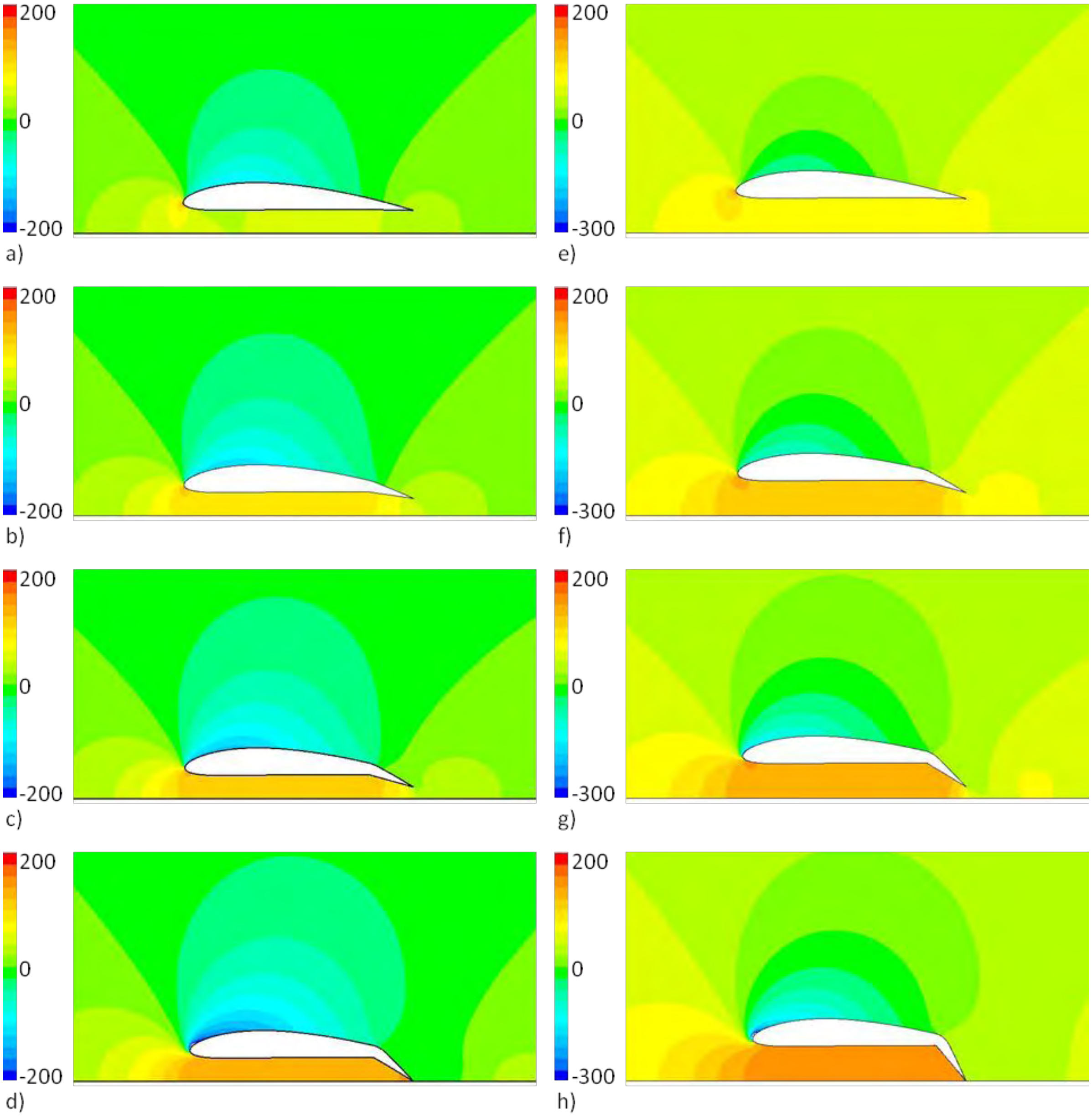

Fig. 4.8. Pressure contours (Pa) with $\alpha = 2°$ and $Re = 10^6$: a) $h/c = 0.1$ and $h_f/c = 0.1$; b) $h/c = 0.1$ and $h_f/c = 0.075$; c) $h/c = 0.1$ and $h_f/c = 0.05$; d) $h/c = 0.1$ and $h_f/c = 0$; e) $h/c = 0.15$ and $h_f/c = 0.15$; f) $h/c = 0.15$ and $h_f/c = 0.1$; g) $h/c = 0.15$ and $h_f/c = 0.05$; h) $h/c = 0.15$ and $h_f/c = 0$.

Similarly, the pressure contours are determined for the same cases and are shown in Fig. 4.8 for varying flap deflection. As the flap is deployed, it is observed that the slowdown and entrapment of flow leads to a significant pressure recovery beneath the airfoil. It appears that the largely augmented suction peak on the upper nose of the airfoil is due to the increased flow over the suction surface, caused by the increased pressure beneath the airfoil forcing large amounts of flow over the airfoil. It is found that the pressure underneath the airfoil and the suction peak continue to increase until the limiting case where the flap is touching the ground. In this limiting case nearly all flow underneath the airfoil is stagnated, creating a high-pressure zone. In which case, the flow forced over the nose creates the beneficial low pressure zone above the airfoil.

A better idea of the flow structures for the above cases can be found in the velocity streamlines of Fig. 4.9. Figure 9 demonstrates the general flow patters as the flap is deflected. With small flap deflections very little separation is found above the flap and the flow moves smoothly past the airfoil. However, at larger flap deflections (approaching limiting case) the separation zone above the flap becomes very large and in the limiting case a large recirculation zone is also found underneath the airfoil.

Further insight into the flow behavior is shown in Fig. 4.10 for the pressure distribution of the case with $h/c = 0.1$, $\alpha = 2°$, and $Re = 10^6$ for varying plain flap heights. As the pressure and velocity contours implied, the pressure underneath the airfoil and the suction peak both increase as the flap is deflected. The general area in between the pressure and suction curves is an indicator for the lift force. Therefore, it is apparent that as the flap is deflected the lift force of the airfoil should significantly increase. When the flap is deflected to the ground the pressure coefficient is shown to approach or even exceed one. It can be noted that the theoretical maximum for the pressure coefficient is one for the completely stagnated flow and two for the ideally reversed flow. The conflicting boundary conditions, which define the flap trailing-edge point as a part of a stationary wing profile and a moving ground boundary, may introduce inaccuracy in the solution near this point. However, the region where flow is influenced by this effect is rather limited and, therefore, has negligible effect on the force coefficients.

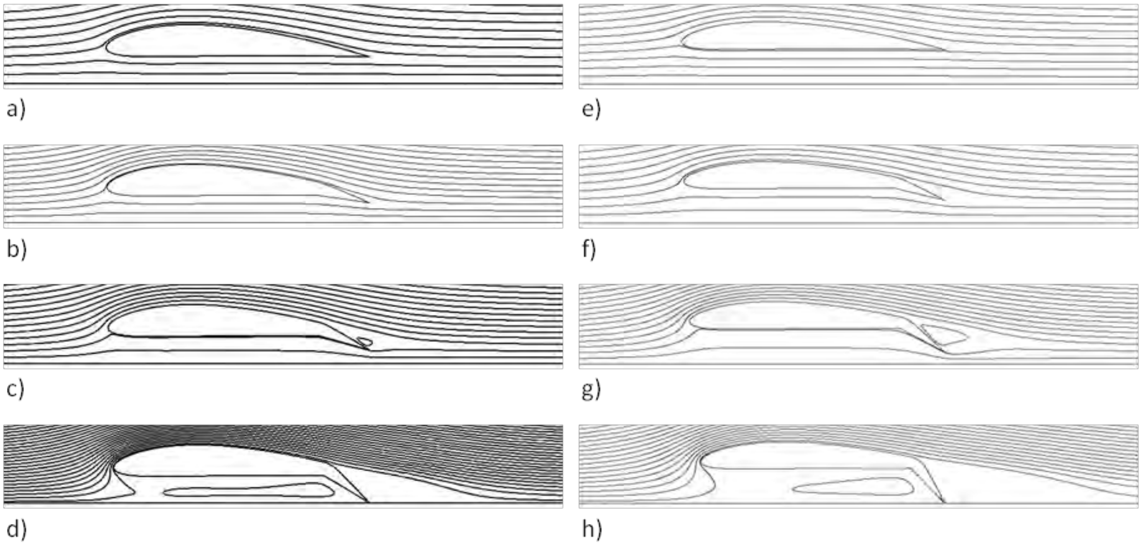

Fig. 4.9. Velocity streamlines with $\alpha = 2°$ and $Re = 10^6$: a) $h/c = 0.1$ and $h_f/c = 0.1$; b) $h/c = 0.1$ and $h_f/c = 0.075$; c) $h/c = 0.1$ and $h_f/c = 0.05$; d) $h/c = 0.1$ and $h_f/c = 0$; e) $h/c = 0.15$ and $h_f/c = 0.15$; f) $h/c = 0.15$ and $h_f/c = 0.1$; g) $h/c = 0.15$ and $h_f/c = 0.05$; h) $h/c = 0.15$ and $h_f/c = 0$.

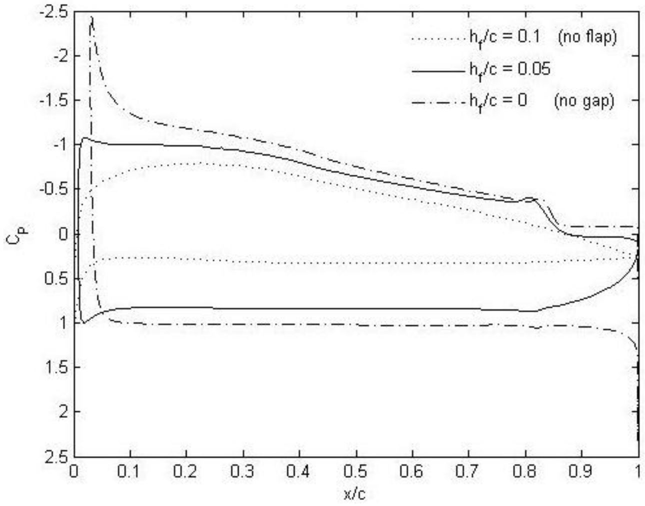

Fig. 4.10. Pressure distribution with deflecting flap at $h/c = 0.1$, $\alpha = 2°$, and $Re = 10^6$.

The aerodynamic lift coefficient, drag coefficient, quarter chord moment coefficient, and lift-to-drag ratio in extreme ground effect flight with a flap are shown in Fig. 4.11 for $\alpha = 2°$, and Re $= 10^6$. As expected, the lift increases when the flap is deflected for all ground heights (Fig. 4.11a). However, the amount of lift augmentation due to the flap appears to lessen as the flap deflection is increased. Therefore, deflecting the flap in extreme ground effect is very effective with small deflections, while the benefit of further deflecting the flap will yield a diminishing gain. Another interesting trend takes place as the ground height h increases with a specified flap height h_f. In this situation the curves for the greater ground heights are above those of lesser ground heights. This lift increase can be explained due to the larger amount of flow which may be trapped beneath the airfoil at a greater ground height with the same distance between the flap and the ground. Lastly, insight can be gained on the situation where an airfoil holds a constant flap deflection, y_f, while approaching the ground. Similar to the ground proximity flight without a flap, with a specified flap deflection the lift is shown to increase as the airfoil approaches the ground. Overall, as shown in the out of ground case, the use of a flap in the extreme ground effect increases the lift of the airfoil up to the limiting case where the flap is touching the ground.

Similarly, the drag coefficient is shown to increase with flap deflection in Fig. 4.11b. This significant drag increase appears to be caused by two contributing pressure drag forces. As shown in Fig. 4.8 the pressure underneath the airfoil increases as the flap is deflected. This increase coupled with somewhat vertical geometry of the deflected flap creates an increasing blunt area perpendicular to the flow resulting in a much greater drag force in the flow direction. In addition to this drag increase, the use of a flap has been shown to increase the separation on the upper surface of the flap providing a low-pressure zone behind the flap and further increasing the pressure drag. Overall, with the same flap deflection, y_f, the ground height appears to have little effect on the drag force, as the large pressure drag due to the flap appears to dominate.

Figure 4.11c presents the quarter chord moment coefficient as the flap is deflected in extreme ground effect. The moment coefficient is defined as the moment at the quarter chord as shown in Fig. 4.1 divided by the free stream dynamic pressure, airfoil surface area, and chord. As the flap is deflected at a specified ground height h, the nose down pitching moment is shown to increase up until the limiting case where flap is touching the ground. This increase in nose down pitching moment is explained by the larger pressure beneath the airfoil acting against the increased area of the blunt flap. Similarly, as the airfoil approaches the ground with constant flap deflection y_f, the nose down pitching moment also increases as pressure beneath airfoil is augmented in ground effect. However, as the airfoil approaches the ground while holding a constant flap height h_f, the nose down pitching moment decreases, as smaller amounts of flow are trapped beneath the airfoil.

The lift-to-drag ratio, which represents the aerodynamic efficiency of flight, is shown in Fig. 4.11d. This characteristic has been one of the selling points of ground-effect vehicles, since near the ground an increase in lift and decrease in induced drag lead to an improvement in the aerodynamic efficiency. As explained above there are two competing contributions to the lift-to-drag ratio: the lift is augmented by the flap, and the pressure drag is increased by flap. In the current study it is observed that small deflections of the flap, where the lift is strongly augmented, lead to an increased lift-to-drag ratio. As the flap is further deflected the pressure drag begins to dominate and the lift-to-drag ratio drops lower than the undeflected flap in ground-effect. The lift-to-drag ratio appears to generally reach a maximum with the flap deflected 2.5% of the chord, and continues to be greater than the undeflected flap up to a deflection of approximately 5% of the chord. Overall, it is shown that the use of a small plain flap deflection in ground effect can increase the aerodynamic efficiency and provide an improved operating region for the considered angle of attack.

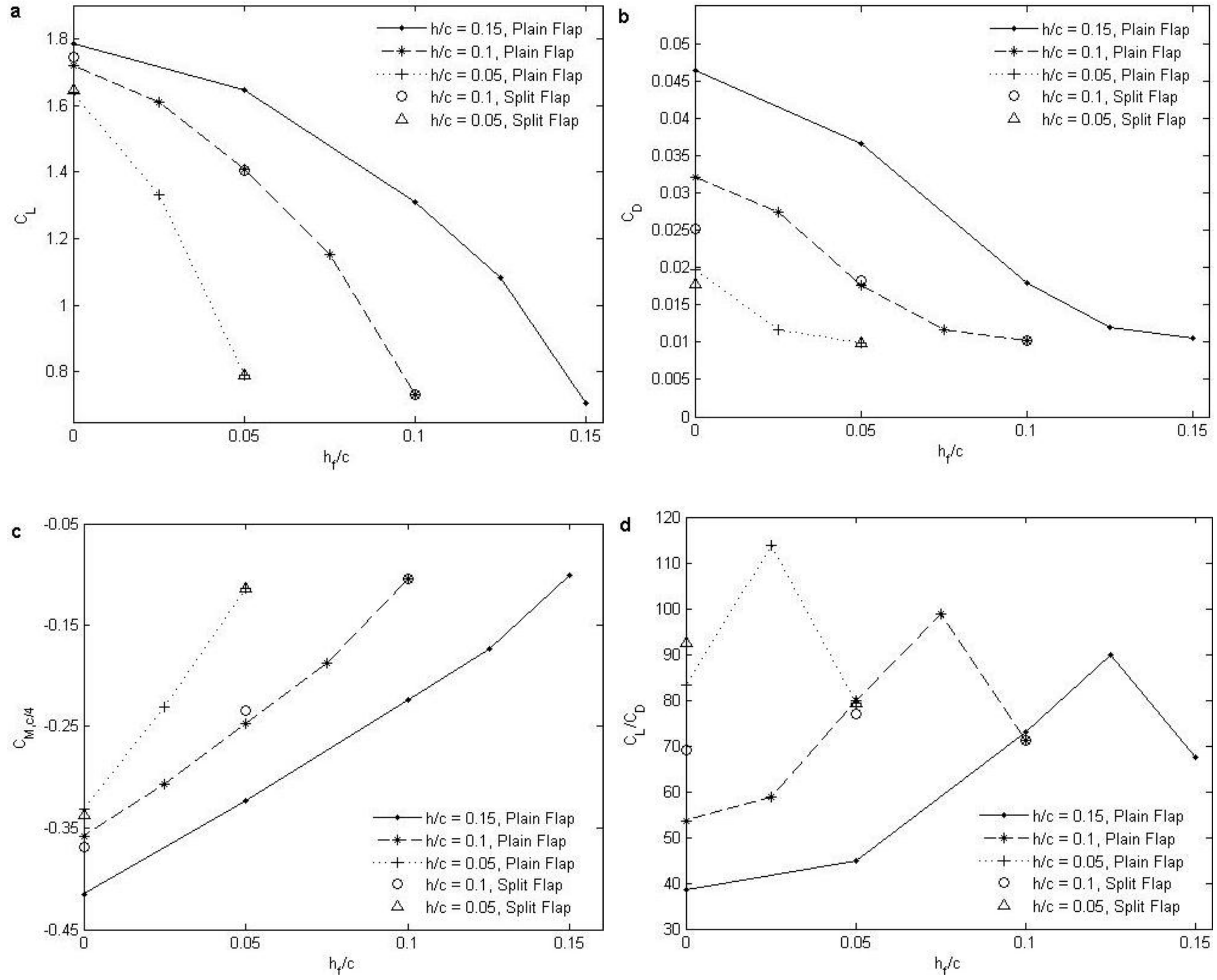

Fig. 4.11. Aerodynamic trends as flap is deflected while approaching the ground at Re=10^6, and α = 2°: a) lift coefficient; b) drag coefficient; c) quarter-chord moment coefficient; and d) lift-to-drag ratio.

Results of the selected split flap simulations are also shown in Fig. 4.11. Differences in the lift and moment coefficients between split and plain flaps are found to be minimal, with the split flap providing slightly higher lift in the limiting case with the flap touching the ground. The drag coefficient is also predicted similarly until the limiting case where the split flap geometry predicts a significantly smaller drag. This reduction in drag may be a result of the smaller separation zone behind the split flap as compared to the plain flap. The split flap does not deflect the rear of the airfoil as in the plain flap case. Instead, an additional flap is added as an attachment to the existing undeflected airfoil. As expected from the lift and drag behavior, the lift-to-drag ratio is very similar to the plain flap data until the limiting case is reached. At this point the split flap provides a much higher lift-to-drag ratio, resulting in improvements over the plain flap in the limiting case with flap touching the ground.

Results for a plain flap with constant flap deflection $y_f/c = 0.05$ at attack angles 2° and 6° and Reynolds number 10^6 are shown in Fig. 4.12. As theoretically expected, the lift and drag increase as the angle of attack is increased. However, as the ground is approached, the lift augmentation gained by increasing angle of attack is reduced. This is apparent for $\alpha = 2°$ and 6° as there is a large difference in lift values out of ground (plotted at $h/c = 1$), while as airfoil with flap approaches extreme ground proximity the curves approach each other, resulting in a smaller lift benefit with increasing attack angles in ground effect. It is also noticed that in the ground height region $h/c \sim 0.5$ the airfoil with flap deflected obtains a lesser lift than the out of ground flap case, which is similar to previous observations (Steinbach and Jacob, 1991). As the airfoil further approaches the limiting case, the flap is shown to then provide improved aerodynamic properties. Unlike the lift, the drag is shown to be significantly higher for the out of ground case, while reducing in ground proximity. Overall, the lift and drag increase with angle of attack, while in some regions the use of flap in weak ground effect yields a smaller lift than the out of ground case.

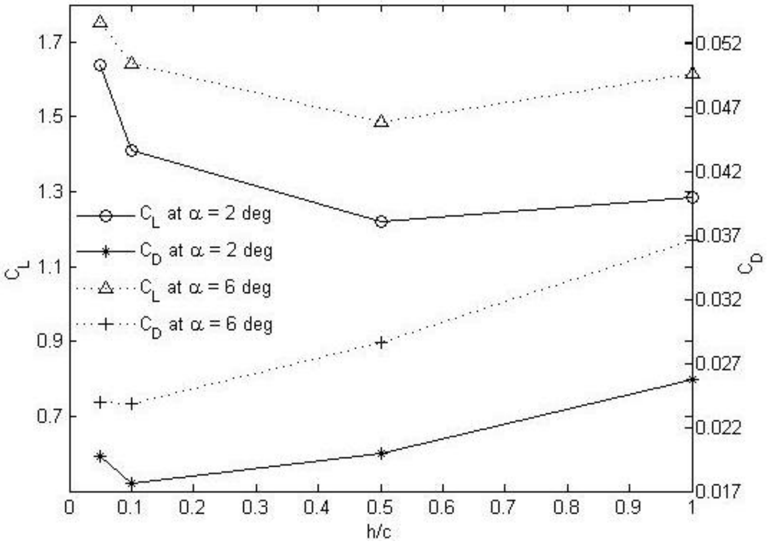

Fig. 4.12. Effects of angle of attack with constant flap deflection of $y_f/c = 0.05$ and Re = 10^6 for plain flap. Data plotted at h/c = 1 correspond to values at $h/c = \infty$.

Reynolds number effects on ground proximity flight with a flap are also of importance. The pressure distributions for h/c = 0.1, α = 2°, while comparing Re = 10^6 and Re = 10^7 are shown in Fig. 4.13. Pressure distributions for both Reynolds numbers appear to behave very similarly. The pressures below the airfoil are shown to slightly increase as the Reynolds number increases. Similarly, the suction pressures above the airfoil are also slightly increased.

Figure 4.14 presents the effect of Reynolds number on the lift and drag coefficients for a ground height h/c = 0.1, flap height $h_f/c = 0.05$, and α = 2°. As expected, the minimal changes in pressure distributions have only led to a very small lift increase with increased Reynolds number. On the other hand, the drag coefficient is shown to significantly decrease with increased Reynolds number. This effect can be related to behavior of the skin-friction coefficient which decreases with the Reynolds number. Overall, an increase in Reynolds number is shown to have small influence on the aerodynamic effects due to flap use in extreme ground effect.

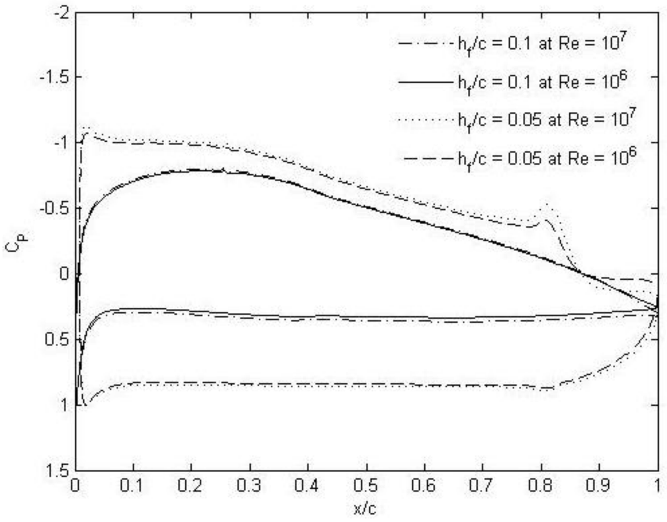

Fig. 4.13. Pressure distribution for varying Reynolds numbers at h/c = 0.1 and α = 2°.

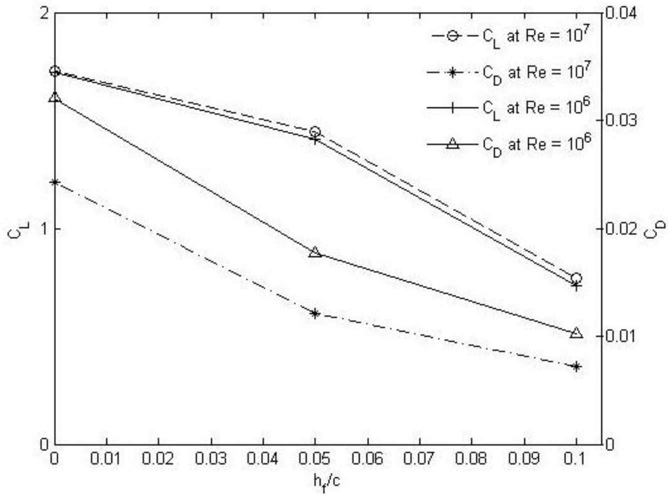

Fig. 4.14. Reynolds number effects on lift and drag coefficients at h/c = 0.1 and α = 2°.

Lastly, a few of the airfoil-flap configurations in ground effect presented small scale unsteady behaviors. In such cases the transient solution was computed with the URANS technique and the aerodynamic forces were time averaged. A visualization of these unsteady effects is presented in Fig. 4.15 with the velocity contours at four different instants in time. The unsteady behavior consists of vortex shedding structures similar to that of a circular cylinder. A shedding Strouhal number of 0.17 was estimated from the limited number of unsteady configurations. Although the unsteady effects are of little importance for the current goals of increasing aerodynamic efficiency, they may be significant for future studies which focus on vibrations or small time scale force fluctuations.

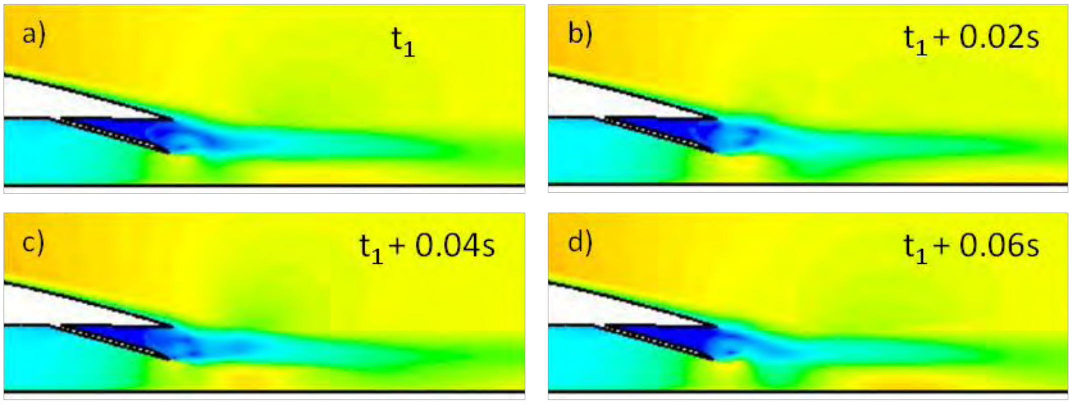

Fig. 4.15. Unsteady split flap configuration studied with URANS: a) t_1; b) t_1+0.02s; c) t_1+0.04s; d) t_1+0.06s;

4.4 Discussion

The turbulent flow around an airfoil in extreme ground effect with a flap was studied with numerical methods implemented in Fluent. The effects of flap deflection, ground height, flap type, angle of attack, and Reynolds number have been studied. Results have provided insight into the aerodynamic characteristics of the flow, as well as regions of enhanced aerodynamic efficiency for extreme ground-effect vehicles using flaps.

As the flap is deflected, flow is trapped beneath the airfoil, leading to a decrease of flow velocities and build-up of the pressure below the airfoil. Simultaneously, the increasing adverse pressure gradient with flap deflection yields a larger flow separation behind the flap. In the limiting case, with flap touching the ground, a large statistically stable recirculation zone develops between the upper surface of the flap and the downstream ground surface.

In extreme ground effect at small attack angles, the lift coefficient increases as the flap is deflected for all ground heights, although the amount of lift augmentation appears to lessen as the flap deflection increases. Additionally, with constant flap deflection, the lift increases as the ground-effect vehicle approaches the ground. The drag coefficient is also shown to increase with deflecting flap. This drag increase is due to larger pressure underneath the airfoil coupled with the growing separation zone behind the flap.

The aerodynamic forces are additionally studied for effects of attack angle, Reynolds number, and flap type. Similar to the unbounded airfoil without a flap, the lift and drag are augmented by increasing attack angle. Split and plain flap configuration appear to provide nearly identical forces in beneficial flight configurations and, lastly, effects of Reynolds number are minimal in the fully turbulent regime.

Overall, beneficial flight regimes appear to be obtainable in ground effect flight for an airfoil with a relatively flat bottom surface using simple flap mechanization. In extreme ground effect it is shown that the use of small flap deflections significantly increases the lift while increasing the drag to smaller extent. Increases in aerodynamic efficiency are found for flap deflections up to 5% of the chord. The position of greatest efficiency appears to correspond to a flap deflection of 2.5% of the chord. This deflection region, yielding increased efficiency, is valid for all ground heights studied.

CHAPTER FIVE

OBLIQUE PROPULSORS FOR AERODYNAMIC APPLICATIONS

5.1 Simplified Propulsor Modeling

For many ground effect applications, vehicles take advantage of devices such as jet propulsors to increase vehicle lift. It is fairly obvious that in many cases these devices cannot be modeled with the classical jet assumptions made previously. For example Power-Augmented-Ram (PAR) (Fig. 1.4) jets are not confined in the upward direction and require modeling of airflow entering the jet source. To properly model applications of this nature, the jet must be an internal component of the flow with the ability to entrain upstream fluid and exhaust it in a downstream jet.

Planar jets are the focus of this study. Jets with nearly two-dimensional characteristics can be generated with large aspect ratio rectangular nozzles, an example being jet flaps used in some aircraft applications. Another phenomenon includes a formation of nearly planar jet formed by a set of circular jets. This problem was experimentally studied by Knystautas (1964) who showed that a row of jets originated from closely located circular nozzles transitioned to a quasi-two-dimensional jet approximately 12 jet spacing's downstream of the exit. Wang (1996) furthered the study by showing that a row of jets will continue to transition to planar flow when cross flow is introduced. With sufficiently small spacing between individual jets, the interaction of a row of radial jets can be closely approximated with an appropriately positioned planar jet. Therefore, the two-dimensional jet models studied here will not only be valid for large aspect ratio rectangular nozzles, but will also model a row of radial jets which are commonly used in ground effect applications (PAR-WIG, PARV).

A few options are available for the modeling of an internal planar jet propulsor. The most thorough technique models all components of the jet; however, modeling an entire propulsor is computationally expensive and emphasizes details which are not relevant for the study of ground-effect vehicles. A much more manageable option is to introduce a momentum source into the flow to account for the forces introduced by the planar jet. Similarly, the jet may also be modeled by fixing velocity and turbulence profiles inside the domain at a specified position. These methods are very convenient as they allow different types of jets to be tested with minimal model adjustments.

The momentum source technique has been used in the past for simplified theoretical models and qualitative viscous jet studies. Batchelor (1973) used a point source to study the analytical solution of a steady laminar axisymmetric jet. Bennett et al. (2001) modeled viscous contaminant spread with an oscillating fan defined by a time varying momentum source. Transient effects of a confined turbulent jet modeled with a momentum source have also shown reasonable results (Guo et al. 2001). Even previous PAR-WIG case studies have modeled laminar (Kwag, 1997) and turbulent (Hirata and Hino, 1997) three-dimensional jets with a momentum source to avoid modeling of aircraft propulsors. However, little attention has been paid to basic flow phenomena of jet propulsor ingestions and jet impingement in close ground proximity. No use of a fixed internal velocity profile was found in the literature, and an exploratory study of its use for jet propulsor applications will be studied.

5.1.1 Defining the Simplified Jet Propulsor Models

Three methods are used to implement the internal free jet: a momentum source, a ducted momentum source, and an internal fixed velocity profile. The momentum source is specified in a single row of cells. When a ducted geometry is used the single row of cells is positioned at mid-span of a Clark-Y airfoil as shown in Fig. 5.1. This airfoil represents the duct geometry with a chord length of two jet widths. With or without an added duct, implementing a momentum source allows control of the momentum distribution in the duct as opposed to the velocity distribution. The total momentum flow is approximated by integration of momentum flux across the duct,

$$M = \int_{-D/2}^{D/2} \rho U_{0,jet}{}^{2} dS \;, \tag{5-1}$$

where $U_{0,jet}$ is the time-average jet velocity at the jet exit, ρ is the density, D is the duct width, and *dS* is a differential distance across the jet exit. The momentum source distribution specified is nearly constant with a slight linear increase towards the jet edges to produce nearly uniform jet velocity profiles at the exit. This momentum source distribution is calibrated to produce a nearly uniform exit velocity profile which satisfies a specific $U_{0,jet}$ based on the jet Reynolds number,

$$Re = \left(\frac{\rho U_{0,jet} D}{\mu}\right). \tag{5-2}$$

It is clear that the above momentum source model is qualitatively similar to the theoretical technique of Batchelor (1973); only, using a finite jet width and implementing turbulence. Unlike the momentum source model, using the internal specified velocity and turbulence profiles is quite easy and provides direct control of the jet propulsor Reynolds number and turbulence exit profiles. User Defined Functions (UDF) are used to apply the momentum source or fixed velocity profile to the correct cells in Fluent with user specification of jet position (angle and distance from ground).

The study of these jet propulsor models will use a method similar to the validation in Chapter 2, modeled by the steady two-dimensional, incompressible, constant viscosity, turbulent RANS equations (2-4) and (2-5). The isotropic Boussinesq approximation is made, with closure provided for the RANS equations by the standard k-ε turbulence model. This closed set of governing equations is solved numerically with the segregated SIMPLE algorithm while implementing the 2nd order discretization scheme for pressure and 2nd order upwind scheme for momentum, kinetic energy, and turbulent dissipation. The numerical methods used are explained in detail in Chapter 2 and current parameters are shown in Table 5.1.

density	1.225 kg/m^3
viscosity	1.7894e-5 kg/m-s
jet width	2 cm
Reynolds Number	11,400
grid size	248,700 cells
solver	2D Steady
pressure-velocity coupling	SIMPLE
press. descretization	2nd Order
mom. descretization	2nd Order Upwind
mod. viscosity descretization	2nd Order Upwind
turbulence model	Standard k-ε
Y+	0.5-1
tot. momentum source	0.85 N/m
fixed velocity specified	8.3 m/s

Table 5.1 Simplified jet propulsor solution parameters using near wall approach.

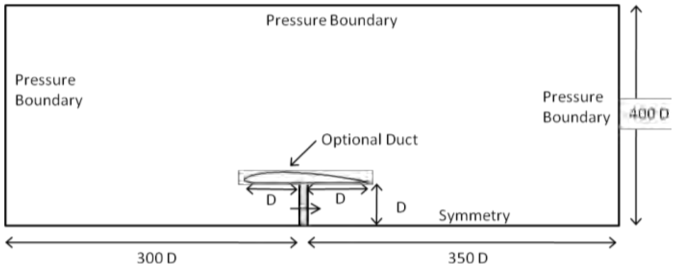

Fig. 5.1: Computational domain for jet propulsor model study. Shaded region represents the area where the momentum source or fixed velocity profile is specified.

The planar turbulent free jet exiting from a wall, in Chapter 2, was not concerned with the jet entrainment or flow upstream of the jet. However the suction and entrainment upstream of the jet source must now be accounted for to properly model the jet propulsor for aerodynamic applications. As shown in Fig. 5.1, the current computational domain is similar to the domain of the planar jet only with an increased upstream domain size. As mentioned above the internal momentum source or fixed velocity is specified in a single column of cells as shown by the shaded region in Fig. 5.1. Although a duct is shown in Fig. 5.1, it is optional and will only be implemented in the study of the ducted momentum source model.

The top, downstream, and bottom boundary conditions are specified as a pressure inlet, pressure outlet, and symmetry respectively. When the duct is included in the simulation it takes a no-slip wall condition. As opposed to the classical jet modeling, the upstream boundary is no longer specified as a wall. Instead it is modeled with a pressure inlet boundary which allows entrainment of fluid into the domain. With the upstream boundary specified as a pressure inlet, the velocity upstream cannot be directly specified. However, the upstream velocity due to the pressure inlet can be considered negligible in comparison to the jet flow behavior.

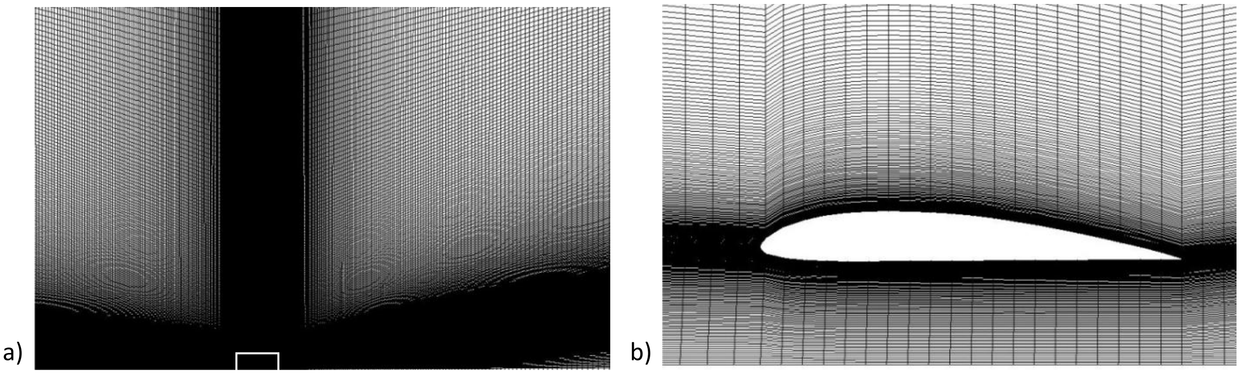

Fig. 5.2: Ducted momentum source mesh: a) full domain; b) close-up of ducted momentum source zone (box in full domain). Symmetry is imposed along domain bottom.

Figure 5.2 shows the mesh created for the computational domain of the ducted propulsor. The structured mesh of the downstream domain is of identical mesh density to the classical turbulent jet which achieved mesh independence at 57,500 cells. However, with the increase in size of the new computational domain, a greater number of cells are needed to provide the same mesh density. The total mesh contains 248,700 cells, providing a mesh independent grid which captures all large scale flow phenomena. When the duct is implemented the no-slip condition requires mesh refinement to the viscous sub-layer. Although the mesh of the ducted jet propulsor is shown, similar meshes were created without the duct as well.

In order to ensure domain size was chosen of a large enough size to capture the physics upstream of the jet propulsor, a domain size independence study was completed. The results of this study are shown in Fig. 5.3 for the regular momentum source model. As shown in Fig. 5.3, the upstream, top, and downstream domains were increased by 50% and compared with the initial computational domain. The centerline decay with increased top, upstream, and downstream domains is nearly identical in the ground effect range of interest below x/D = 30.

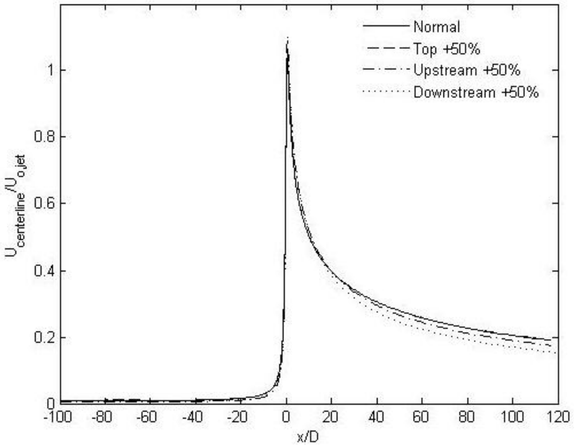

Fig. 5.3: Centerline velocity decay for varying sizes of computational domain.

This domain size study validates that the domain captures the correct trends; however increasing the domain size is not particularly relevant for the jet in stagnant flow because entrainment far from the jet is no longer turbulent, and the fully turbulent assumption yields errors. This modeling error is alleviated when ambient flow is introduced, or in cases where only the near jet region is of interest (e.g. current study).

5.1.2 Choosing an Adequate Jet Propulsor Model.

An adequate jet propulsor model will be chosen for our ground effect studies by fixing the jet geometry and strength, with the jet width and Reynolds number specified at 2 cm and $1.14 \cdot 10^4$ respectively. Each model has been calculated in the above configuration and comparisons are presented below.

Figure 5.4a presents the jet exit velocity profiles for the propulsors defined by momentum source, fixed velocity, and ducted momentum source. A significant amount of information can be gained by comparing the exit profiles to the common jet propulsor profile. With all jets defined the same, it is clear that the regular momentum source method lacks control of the profile width and magnitude. This momentum source method is in reality predicting a much wider jet (than specified) beginning from a near Gaussian profile. On the other hand we can see that when a duct is provided around the momentum source, it is then contained to the specific jet exit area and results in a nearly uniform velocity profile which meets the physical expectations of a propulsor. Lastly, with the fixed velocity profile, complete control of the jet profile is obtained.

Downstream jet flow is also of importance and is shown in Fig. 5.4b with the non-dimensional radial velocity profiles compared to classical jet theory. Before these results are discussed it is important to differentiate between the classical jet (exiting from a wall), and the internal jet propulsor which is currently being studied. Some aspects of these two flows will be different, specifically the flow entrainment. Figure 5.5 shows the streamlines for the ducted momentum source jet in which flow is allowed to enter through the upstream boundary as opposed to the classical case. As the streamlines approach the jet region, fluid feeding into the jet actually entrains more fluid outside but parallel to the jet, qualitatively similar to the theoretical model of Batchelor (1973). With this behavior an increase in flow rate and momentum immediately downstream of the jet is expected. Although small differences (from the classical jet exiting from a wall) develop in the near jet region, the classical flow entrainment mechanism begins less than 5 jet widths downstream of the exit. Therefore, the current unbounded jet can be approximated by the classical jet outside of the near jet region.

In Fig. 5.4b the radial profiles of the ducted momentum source are very near the classical empirical results of Eq. (2-14). As expected the maximum velocity lies along the jet centerline and turbulent mixing diminishes velocity in a Gaussian manner towards the jet edges. The fixed velocity and regular momentum source profiles provide similar trends but require corrections of the position of the virtual origin to provide exact agreement. This error is expected for the momentum source which began from an already developed velocity profile (Fig. 5.4a).

Another important parameter of jet flow is the centerline velocity decay which is shown in Fig. 5.4c. Again the ducted momentum source provides a nearly exact agreement to classical jet theory with closure coefficients chosen as experimentally determined values of $C_1 = 3.78$ and $C_2 = 2.4$ (Rajaratnam, 1976). The erroneous velocity profile of the regular momentum source leads to a very quick decay which is unrealistic for the jet configuration specified. Similarly, the fixed velocity jet predicts a potential core with length of 20 jet widths which is much greater than classical jet theory (6 widths) and is thought to be unrealistic for turbulent jet behavior. Additionally, after the potential core diminishes the jet centerline decays much more rapidly than the classical jet.

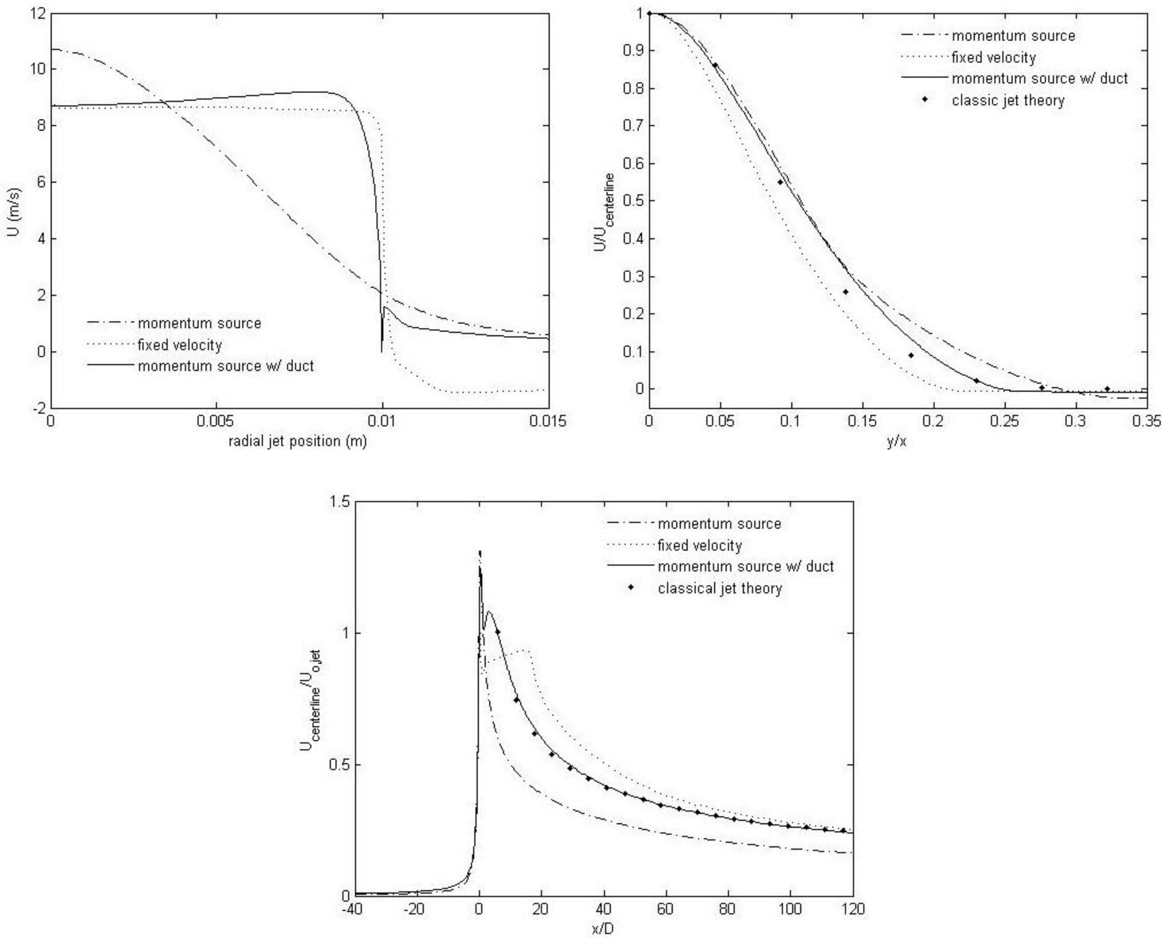

Fig. 5.4: Comparison of propulsor models at Re = $1.14 \cdot 10^4$ and D = 2 cm: a) jet exit velocity profile; b) radial velocity profiles at x/D = 83; c) centerline velocity decay.

As discussed above, the streamlines of the ducted momentum source model are shown in Fig. 5.5. The jet entrains flow through the upstream, top, and downstream boundaries. No unusual structures occur upstream of the jet; flow is slowly entrained from the surrounding environment similar to the theoretical point source jet study of Batchelor (1973). As explained in the classical jet study, the last 50 jet widths of the domain will not be studied due to non-uniform entrainment which occurs near the pressure outlet boundary condition.

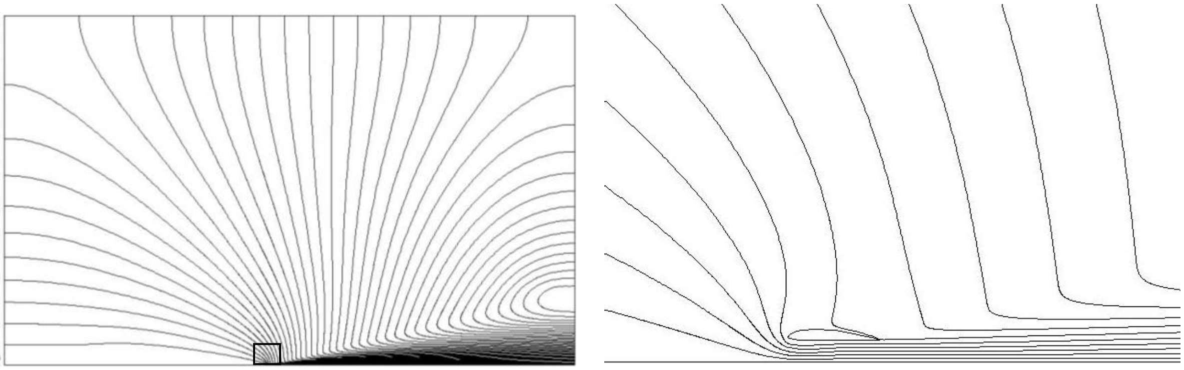

Fig. 5.5: Streamlines of ducted momentum source jet with Re = $1.14 \cdot 10^4$ and D = 2 cm (close-up on right is of jet area in black box).

Of the jet propulsor models presented, one model has performed adequately while the other two methods have presented deficiencies making quantitative jet studies impossible. The fixed velocity profile poorly predicts the jet development and potential core region while yielding additional solution instabilities of unknown source. The regular momentum source predicts the correct trends far downstream of the jet, but its inability to define the exact jet width and position reduces its usefulness for quantitative studies. However, the final model, the ducted momentum source, was able to accurately define the jet and properly predict its downstream behavior. Therefore, ground effect jet studies will implement the ducted momentum source.

With the ducted momentum source model chosen, further validation is presented in Fig. 5.6. Developing radial velocity profiles have been presented in Fig. 5.6a for several x/D jet cross sections. The x/D cross sections are measured with respect to the trailing edge of the duct with positive values downstream. In addition to the good radial profile agreement with the classical jet, the radial velocity profiles become self similar at x/D =40 similar to results of Gutmark and Wygnanski (1976).

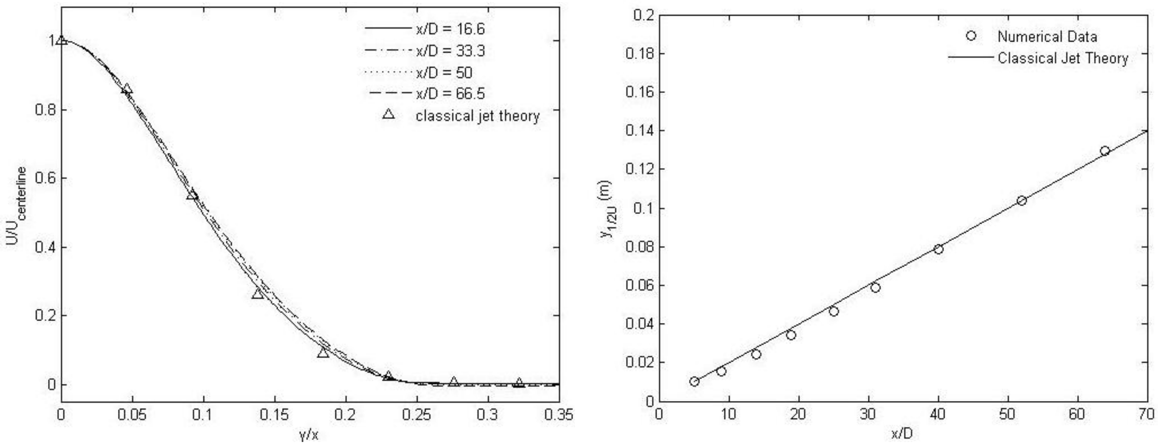

Fig. 5.6: Additional ducted momentum source characteristics at Re = $1.14 \cdot 10^4$ and D = 2 cm: a) developing radial velocity profiles; b) downstream half-velocity spread rate.

The half-velocity jet thickness is shown for the ducted momentum source in Fig. 5.6b; with the solid line representing the classical jet thickness at non-dimensional distances from the trailing edge of the duct. The momentum source jet spreads nearly identically to the classical jet. With this agreement the ducted momentum source method appears to be a valid method for introducing an internal free jet with no need for virtual origin correction.

Overall the ducted momentum source model is chosen for future jet studies. This method allows complete control of the jet geometry, position, and exit profile while agreeing well with classical empirical data (meaning predicts free-jet well). Additionally, the ducted model is similar to theoretical approaches (Batchelor 1973). In the next section this model will be implemented in order to study jet propulsor behavior in common ground effect configurations.

5.2 Oblique Jet Impingement with Cross-Flow

Impinging jets represent a fundamental fluid flow with a broad range of engineering applications. Although the focus of the current study is on jet-supporting aerodynamics, the results are useful for many other applications. Impinging jets are often utilized to enhance heat transfer and mixing in the impingement region. Common applications that take advantage of these enhancements include jets used for heating, cooling, drying of materials (Shi et al., 2003), film and coating thickness control (Tu and Wood, 1996), and production of air curtains (Beaubert and Viazzo, 2003). Without cross-flow, oblique jets are relevant to applications taking place in a stagnant environment, while with cross-flow this model addresses impinging jets translating through a fluid domain.

One aerodynamic application of quasi- planar jets is for support of amphibious Power-Augmented-Ram and Wing-In-Ground vehicles (e.g., Gallington 1987, Matveev 2008). A schematic of the PAR concept was shown in Fig. 1.4. The structure of this vehicle consists of a platform operating in extreme ground effect and side hulls barely touching the ground or water surface. A row of radial jets or a slot jet source is mounted in front of the platform and directed downstream into the nearly two-dimensional channel created by platform, side hulls, and ground. Flow is trapped in this region using a trailing edge flap to create a pressurized air cushion in the channel. Although the PAR-WIG vehicle is a prime example of the use of jets in ground effect, it is common in many ground-effect vehicle designs to use jet support to overcome the inadequate aerodynamic lift at low vehicle speeds. In order to maximize the performance of aerodynamic jet augmented vehicles, a better understanding of the impinging jet is necessary. In addition to an increased fundamental understanding of this flight regime further performance optimization will be studied, providing configurations which avoid unwanted jet propulsor ingestion (Tafti and Vanka, 1992) while at the same time transferring larger amounts of momentum into critical regions.

Several reviews on oblique and normal impinging planar jets with and without cross-flow have been published (e.g., Narayanan et al. 2004, Looney and Walsh 1984, Viskanta 1993). The simplest impinging jet occurs when impingement is normal to a solid surface, creating symmetric wall jets. Experimental pressures, velocities, and shear of planar (Tu and Wood 1996, Maurel and Solliec 2001) and round (Baydar and Ozmen, 2006) normal impinging jets have been extensively investigated. Tu and Wood (1996) demonstrated a near Gaussian and symmetric pressure distributions, while Baydar and Ozmen (2006) presented significant differences in flow structures of jets impinging in and out of a confined channel. Beaubert and Viazzo (2003) studied planar impingement numerically using large eddy simulation (LES) for a slot jet exiting from a wall and found good agreement with data of Tu and Wood (1996). In the experiments of Krothapalli (1987) a cross flow was introduced as the jet exited normally from bottom of an NACA 0018 wing section and impinged on the ground. It was noticed that depending on the cross-flow magnitude and ground proximity a suck-down force was possible due to upstream jet entrainment and formation of ground vortex. Abdon and Sunden (2001) numerically studied a similar case of a normally impinging jet confined in a channel with cross flow. However, the emphasis of that work was on heat transfer properties rather than on flow structure.

Several experimental and numerical investigations have been carried out for obliquely impinging jets. Chin and Agarwal (1991), Akansu et al. (2008), and Beitelmal et al. (2000) conducted two-dimensional experimental studies of obliquely impinging slot jets in the absence of cross flow. Chin and Agarwal(1991) and Akansu et al. (2008) present pressure distributions for several different jet angles and note displacement of the jet stagnation point in the upstream direction as the jet angle deviated from 90°, while Beitelmal et al. (2000) only presents Nusselt number. Roy and Patel (2003) studied the flow patterns of two rectangular oblique impinging jets contained in a confined corner. Shi et al. (2003) introduced cross-flow and numerically solved for the obliquely impinging slot jet confined in a duct using FLUENT with k-ε and

Reynolds Stress turbulence models. The main focus of all of the above studies were on enhanced heat and mass transfer properties while the pressure distribution on the ground was the only information given with relation to flow characteristics.

In the case of conventional V/STOL craft, individual radial jets (not forming a row) generally provide a vectored thrust which creates three-dimensional flow. As V/STOL craft move at forward speed, the jet impinging on the ground creates a ground vortex in front of the craft which bends in a horseshoe shape around the front of the craft (Stewart, 1989). Unconventional V/STOL craft using a row of radial jets or a slot jet spanning a large aspect ratio wing have also been investigated. Several V/STOL studies have made this planar assumption (Kotansky and Bower 1978, Chuang and Ching-Yuan 1991, Chattopadhyay and Saha 2003) while implementing a normal impinging jet exiting from the solid aircraft underside without cross-flow.

Although there is a significant amount of data on obliquely impinging jets, all studies referenced above use jets confined in some sense. The experimental studies use a nozzle for jet creation and, therefore, do not provide any information on the effect of impinging flow on the jet propulsor entrainment and ingestion. Numerical methods have similarly used a nozzle exiting out of a solid wall while in many cases further containing the resulting flow to a channel. It is apparent from Fig. 1.4 that the PAR jets are unbounded in the upstream/upward direction, and therefore, previous approaches of contained jets cannot properly model the front flow of this jet configuration.

In the present study, the jet propulsor is modeled as a ducted momentum source placed inside of the domain with the ability to entrain fluid and exhaust it in an accurate fashion (5.1.3). The remainder of this chapter contains a systematic study of the obliquely impinging jet, which analyzes the basic oblique impingement flow structures with cross flow. Geometries studied consist of ground distances r/D = 4 and 12 and oblique jet angles of θ = 15 and 30°. For these geometries, dependence on cross-flow is analyzed at ambient to jet velocity ratios of 0, 0.1, 0.2, and 0.3. The effect of variable Reynolds number is also investigated. It should be noted that at ground distances r/D = 4 and 12 the model can represent a large aspect ratio rectangular jet such as a jet flap. The greater ground distance of r/D = 12 can also represent a row of radial jets transitioning to a planar jet (row of PAR propulsors).

5.2.1 Numerical Model

The planar impinging jet flow is governed by the steady two-dimensional, incompressible, constant viscosity, turbulent Reynolds Averaged Navier Stokes (RANS) equations, Eqs (2-4) and (2-5). The Reynolds stress term is modeled with the Boussinesq approximation, which assumes turbulent viscosity is isotropic and linearly relates the Reynolds stress tensor to a mean strain rate. The standard k-ε turbulence model is then implemented to provide a model for the turbulent eddy viscosity, μ_T, and provide closure for the Navier-Stokes equations with the Boussinesq approximation. For brevity a full description of the k-ε model is not presented here but can instead be found in section 2.1.3. The k-ε turbulence model has been used as it is robust and computationally inexpensive and has been validated in Chapter 2 for planar jet flows. The closed set of governing equations are solved numerically with the segregated SIMPLE algorithm while implementing the 2nd order discretization scheme for pressure and 2nd order upwind scheme for momentum, kinetic energy, and turbulent dissipation. Solution parameters are shown in Table 5.2, with exception of the validation geometries needed to compare with experiments.

The ducted momentum source is again implemented in the current geometry exactly as described in section 5.1.2. The momentum source is calibrated to produce a nearly constant jet exit profile with a Reynolds number of 20,000. Validation of impingement results with the ducted momentum source is provided with experimental impingement comparisons in the next section.

density	1.225 kg/m^3
viscosity	1.7894e-5 kg/m-s
jet width	2 cm
jet Reynolds Number	20,000
solver	2D Steady
pressure-velocity coupling	SIMPLE
press. descretization	2nd Order
mom. descretization	2nd Order Upwind
mod. viscosity descretization	2nd Order Upwind
turbulence model	Standard k-ε
Y+	0.5-1
r/D	4, 12
impingement angle θ	15, 30°
velocity ratio	0, 0.1, 0.2, 0.3

Table 5.2. Oblique propulsor impingement parameters with near wall approach.

The computational domain is shown in Fig. 5.7 with domain extending 150 jet widths upstream and downstream of the jet impingement, and 100 widths from impingement to top of domain. The use of this large domain in all directions allows for flow to be properly entrained into the jet, while impingement flow patterns show no dependence on boundaries. The jet position is defined with θ representing the angle between the jet centerline and the horizontal plane and r corresponding to the distance along the jet centerline from the jet exit plane to intersection with the ground plane. Whenever x/D is referenced in the results section, the zero reference point is located at this point where the jet centerline intersects the ground plane. Additionally the pressure coefficient and non-dimensional shear stress definitions may be found in Appendix A.

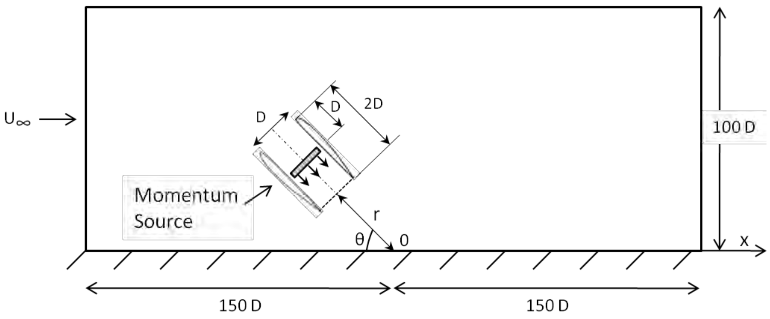

Fig. 5.7: Computational domain and boundary conditions for internal oblique impinging jet.

In cases without cross flow, the upstream, top, and downstream boundaries are modeled with constant pressure boundary conditions. These boundaries are set far enough from the jet impingement that the pressure does not significantly change near domain boundaries. These pressure boundaries also allow fluid to pass in and out of the domain. When cross flow is implemented, the upstream and top boundaries are instead set with a uniform cross-flow velocity. It should be noted that although the pressure boundaries used in the static case allow flow entrainment into the domain, it is small in comparison with velocities at domain boundaries when cross flow is specified.

For all cases the propulsor duct boundary is modeled with a stationary no-slip wall, while the ground condition is a no-slip wall moving at the cross-flow velocity. With zero cross flow, the ground becomes a stationary no-slip wall, whereas the ground moves at a fraction of the jet velocity when cross-flow is implemented. This moving wall technique is generally used in aerodynamic applications where vehicles move past the air and ground at the forward speed of the vehicle. When fixed ground conditions are used with cross flow in ground-vehicle studies, an unrealistic boundary layer develops resulting in an upstream domain dependent solution (Barber et al., 1998). As theoretically expected, the ground vortex will separate much sooner with the moving ground condition, due to the lack of momentum deficit upstream of the wall jet, which is generally caused by the boundary layer (Knowles and Bray, 1991).

The domain has been meshed with a structured grid of quad cells. Refinement of the quad mesh has been applied in the duct, jet exit, impingement, and wall jet spreading regions. The wall adjacent mesh size is chosen to resolve the viscous sub-layer with non-dimensional y+ values of approximately 1 for studied Reynolds numbers. The standard k-ε model is implemented with enhanced wall functions to properly account for the viscous sub-layer. Sufficiently fine meshes are applied that produce mesh-independent results similar to Fig. 2.12.

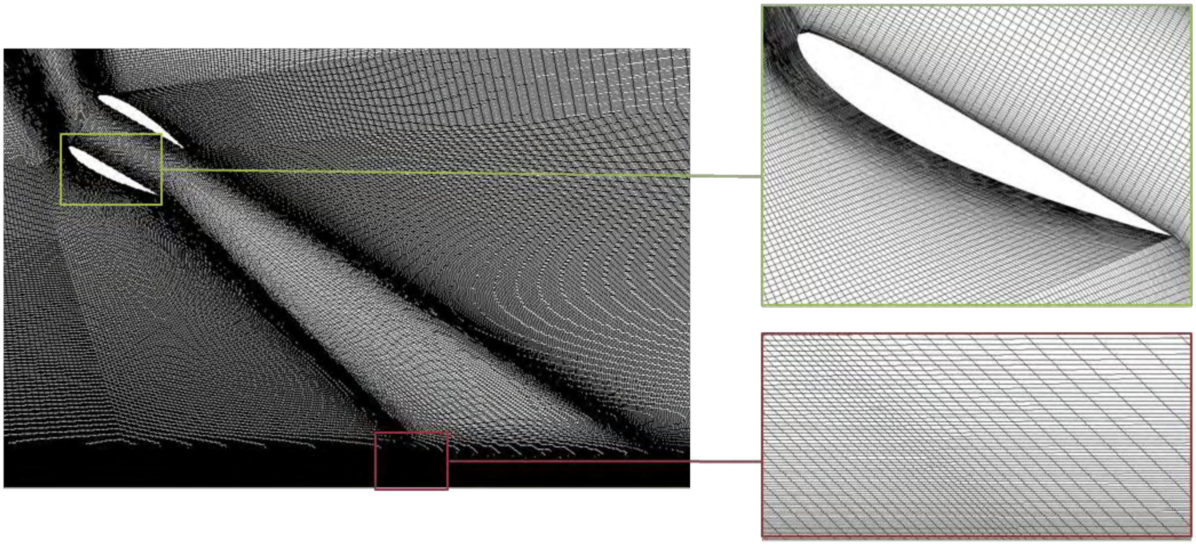

Fig. 5.8: Structured mesh in oblique impinging jet vicinity at r/D = 12 and θ = 30°. Close-ups of the duct and impingement boundary layer mesh are shown due to fineness of mesh.

5.2.2 Normal and Oblique Jet Impingement Validation

Validation of jet impingement is necessary for the current study. Tu and Wood (1996) have presented experimental data for the pressure coefficient and wall shear stress of a normal impinging jet at a Reynolds number of 11,000 and ground distances r/D = 4, 12. The experimental data is compared with numerical simulations in Fig. 5.9 where both static pressure and wall shear stress are non-dimensionalized by the dynamic pressure at the jet exit. The pressure coefficient shows nearly identical agreement with experimental data for r/D = 4 where jet impinging is within the potential core region. As the jet moves further from the ground, to r/D = 12, good agreement is still shown with a slight under prediction of the peak caused by the slightly reduced potential core length in the ducted momentum source jet. Similarly the non-dimensional shear stress also follows experimental trends. At r/D = 4, the peak values are predicted accurately; while farther from jet impingement the numerical model predicts a slightly smaller shear than experiments indicate. Tu and Wood (1996) indicated that the shear stress measurements were limited by their ability to manufacture Stanton tubes with small heights. So, overall the pressure is quantitatively validated for the numerical model, while due to experimental uncertainties only trends in shear can be validated.

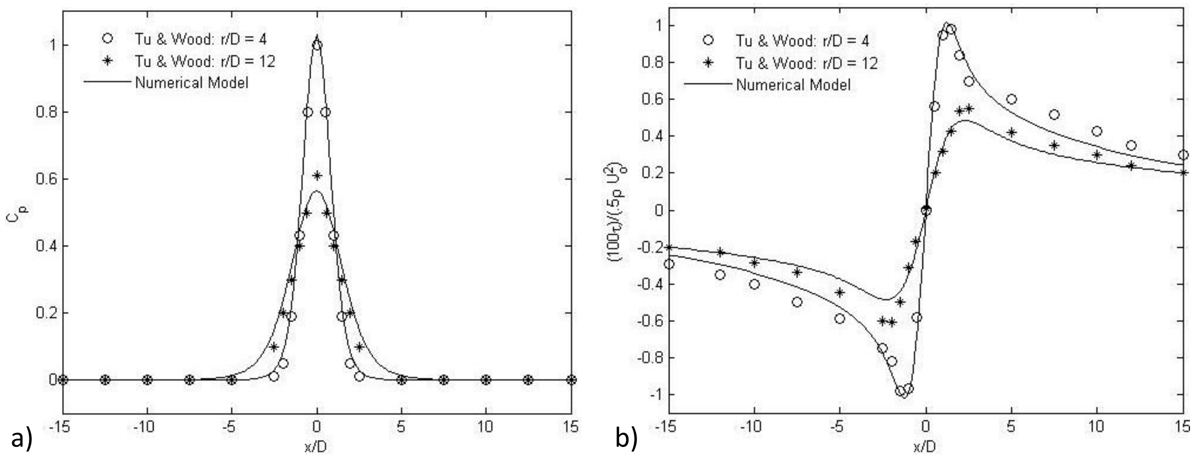

Fig. 5.9: Normal impingement experimental validation at Re = 11,000: a) pressure coefficient; b) non-dimensional shear stress on ground.

Oblique jet impingement has also been compared in Fig. 5.10 to experimental data (Chin, 1991) at Re = 5480, r/D = 4, for θ = 30, 60, and 90°. The figure shows that the pressure peak magnitude at each angle is predicted closely while the stagnation point moves upstream and decreases in magnitude similar to experimental trends with reducing angle. However, large discrepancies are noticed in the distance of upstream shift. The error is not a result of poor modeling, but in comparison of two different physical situations. As will be shown in the results, the jet source suction of the unconfined jet entrains portions of the wall jet when impingement angle is less than 90°. This yields a low pressure zone on the upstream side of the impingement which pulls the stagnation point upstream. With the absence of the jet intake phenomena the extra upstream shift is not expected due to lack of suction pressures at jet inlet. This comparison is thought to validate the general trends of oblique impingement while at the same time confirming that the flow of the unconfined jet is inherently different than the confined jets previously studied.

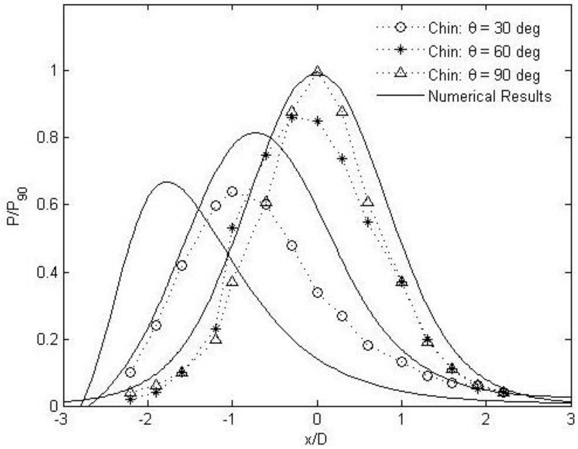

Fig. 5.10: Experimental validation of oblique impingement of ducted momentum source at Re = 5,480, r/D = 4.

5.2.3 Oblique Jet Impingement Results

With the numerical approach validated, the oblique propulsor model is implemented while varying the ratio of upstream cross-flow velocity to average jet exit velocity between 0, 0.1, 0.2 and 0.3. In all studies the average jet velocity at the propulsor exit is kept the same. The ground distance is assigned to be either r/D = 4 or 12, and impingement angle is either θ = 15 or 30°.

The calculated velocity streamlines are shown in Fig. 5.11 and velocity contours in Fig. 5.12. Three configurations are presented to determine effects of ground distance, impingement angle, and cross-flow velocity on an obliquely impinging jet produced by the jet propulsor. Results without cross flow for the three different configurations are shown in Figs. 5.11a, c, e, and 5.12a, c, e. In the case of impingement at small ground distance r/D = 4 and θ = 30° the wall jet component directed upstream of the main jet impingement separates in the zone created between the propulsor and the ground (Figs. 5.11a and 5.12a). The resulting vortex is caused by suction at the jet propulsor entrance and ejection at the propulsor exit. This ground vortex produces the harmful jet propulsor ingestion. As the ground distance is increased at the same impingement angle (Figs. 5.11c and 5.12c) a re-circulating ground vortex is again created between the lower side of the exiting jet and the ground. However, in this case the ground vortex is displaced downstream and does not cause jet propulsor ingestion. As the angle is reduced to 15° (Figs. 5.11e and 5.12e), all of the jet flow is directed downstream, and no significant ground vortex is found in the zone between the jet propulsor and ground.

Figures 5.11b, d, f and 5.12b, d, f present flow patterns with a ratio of cross-flow velocity to jet exit velocity of 0.3. Again, the configuration with r/D = 4 at θ = 30° demonstrates the creation of a ground vortex upstream of the jet impingement (Figs. 5.11b and 5.12b). However, this time the upstream jet component separates much sooner from the ground due to the opposing force of the cross flow and again is entrained into the jet propulsor entrance. As the ground distance is increased to r/D = 12, for both impingement angles, upstream ground vortices are no longer created and the cross flow forces jets downstream, eliminating jet impingement on the ground surface. This behavior occurs due to weaker vertical jet component, which results from larger ground distance or smaller impingement angle.

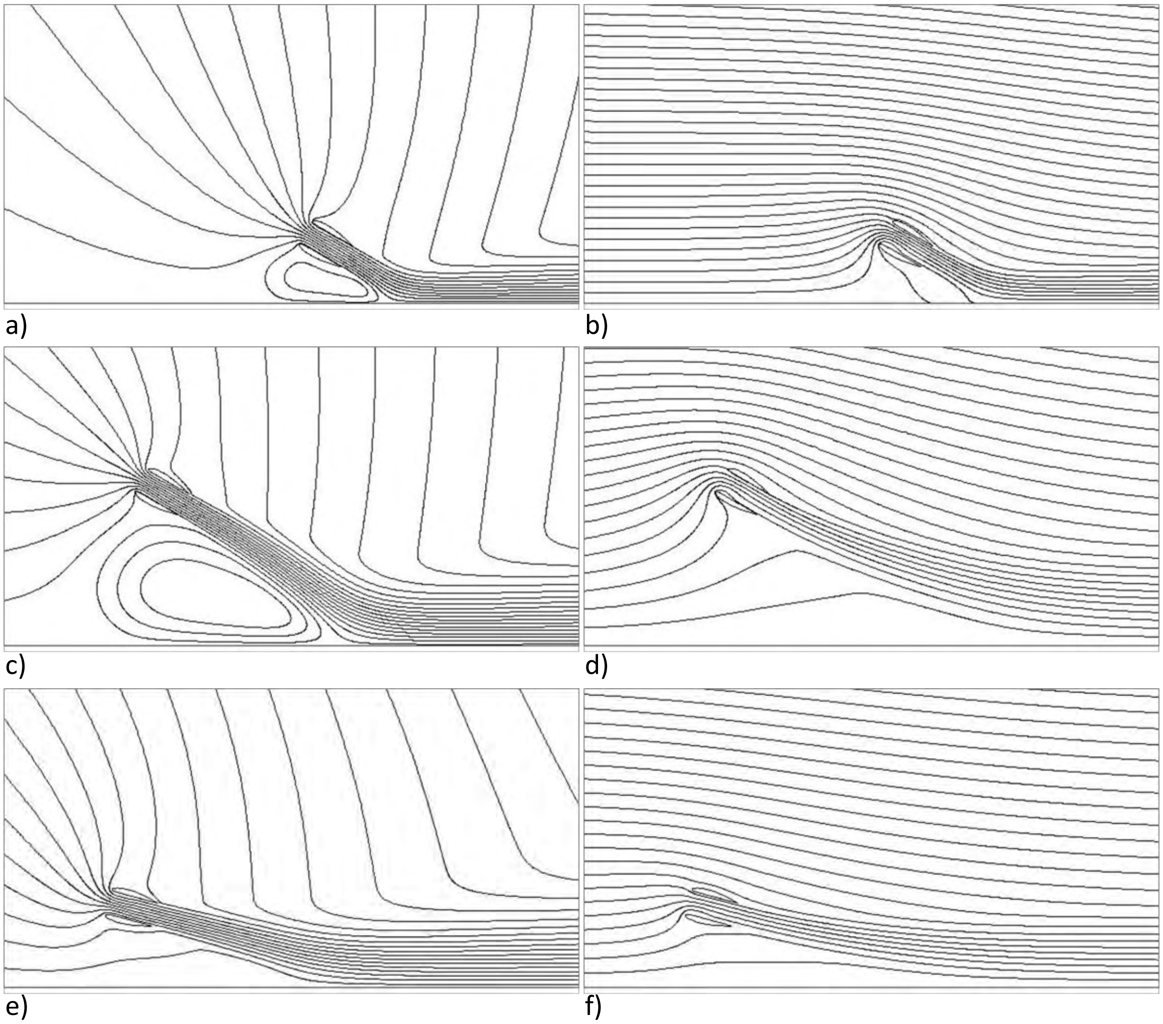

Fig. 5.11: Velocity streamlines for jet Reynolds number Re = $2 \cdot 10^4$: a) r/D = 4, velocity ratio = 0, and θ = 30°; b) r/D = 4, velocity ratio = 0.3, and θ = 30°; c) r/D = 12, velocity ratio = 0, and θ = 30°; d) r/D = 12, velocity ratio = 0.3, and θ = 30°; e) r/D = 12, velocity ratio = 0, and θ = 15°; f) r/D = 12, velocity ratio = 0.3 and θ = 15°.

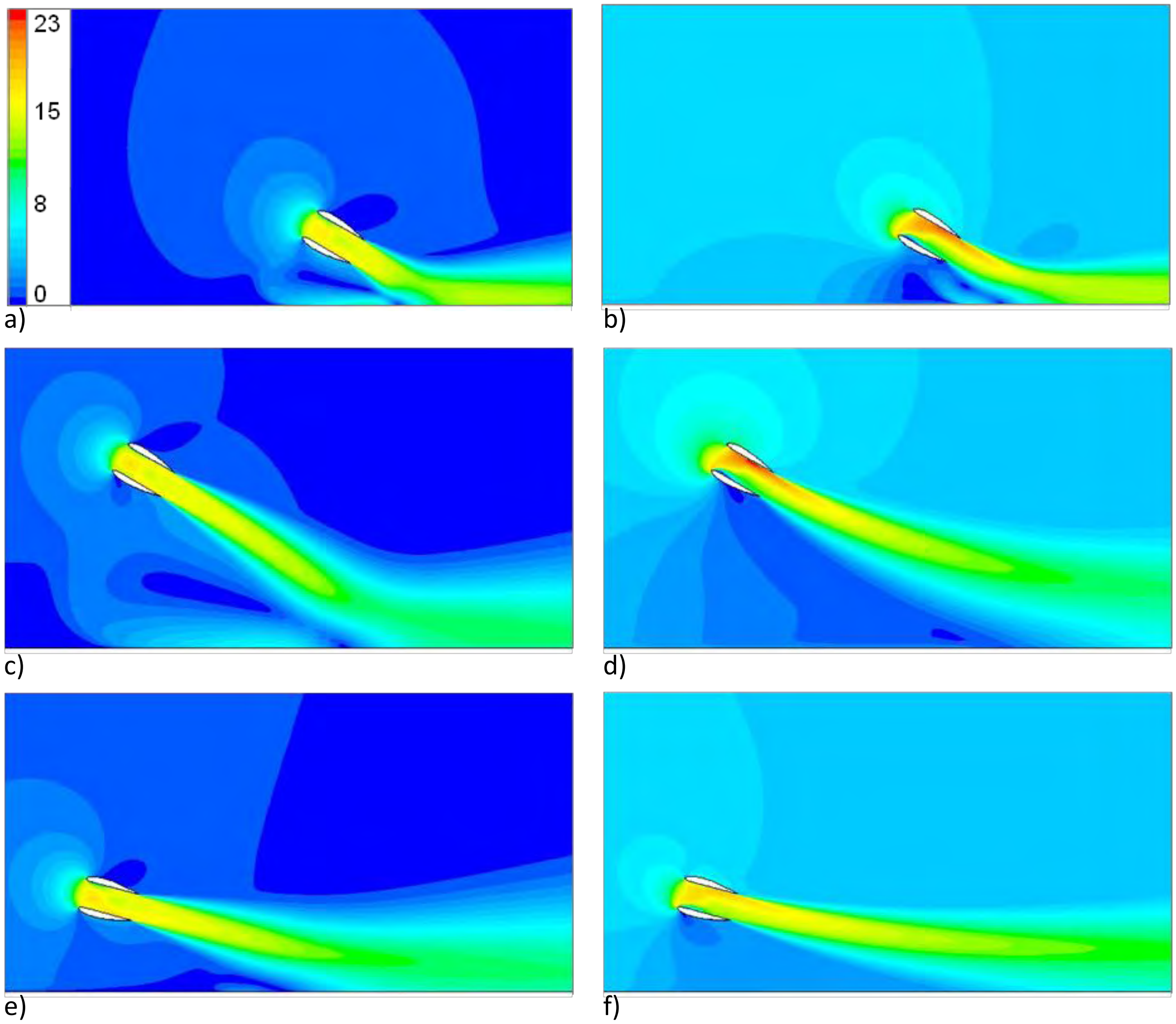

Fig. 5.12: Velocity contours (m/s) for Re = $2 \cdot 10^4$: a) r/D = 4, velocity ratio = 0, and θ = 30°; b) r/D = 4, velocity ratio = 0.3, and θ = 30°; c) r/D = 12, velocity ratio = 0, and θ = 30°; d) r/D = 12, velocity ratio = 0.3, and θ = 30°; e) r/D = 12, velocity ratio = 0, and θ = 15°; f) r/D = 12, velocity ratio = 0.3 and θ = 15°.

Although only the extreme velocity ratios are presented above, Fig. 5.13 shows velocity streamlines at intermediate velocity ratios which support a trend that the upstream ground vortex and ingestion flow are significantly decreased in size as cross flow is increased. Additionally, the smooth transition of flow from an obliquely impinging jet to a jet carried downstream by cross flow is visible. In general it appears that all flow structures change as a smooth function of velocity ratio.

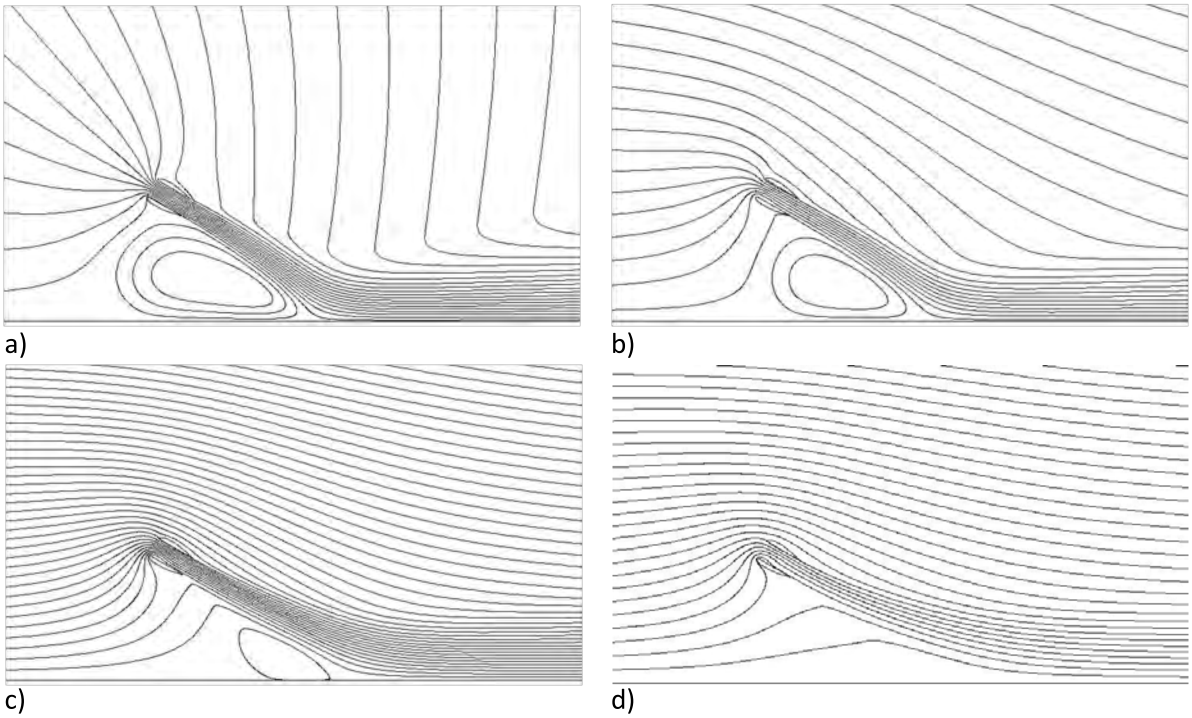

Fig. 5.13: Velocity streamlines presenting a smooth transition with varying cross-flow for r/D = 12, θ = 30°, and Re = $2 \cdot 10^4$: a) velocity ratio = 0; b) velocity ratio = 0.1; c) velocity ratio = 0.2; d) velocity ratio = 0.3.

The calculated pressure coefficients on the ground are shown in Figs. 5.14a, b. These values are defined by the static pressure on the ground surface divided by the dynamic pressure of the jet, ($\frac{1}{2}\rho U_{o,jet}^2$). As shown in the literature (Chin and Agarwal, 1991), the point where the maximum pressure coefficient occurs, analogous with the jet stagnation point, shifts upstream as the jet angle is decreased without cross-flow. This behavior is driven by the low pressure zone between the exiting jet and the ground which draws the jet in the upstream direction. In addition, the pressure magnitude also reduces with decreasing angle, explained by smaller velocity component perpendicular to the ground. At small ground distances the pressure distributions show weaker dependence on velocity ratio than at larger ground distances. The introduction of cross flow significantly reduces or completely eliminates the ground vortex. At large velocity ratio and r/D the jets no longer directly impinge on the surface, and are instead carried downstream by the cross flow (no stagnation peak in Fig. 5.14b).

The wall shear stresses, shown in Figs. 5.14c, d, are non-dimensionalized by the dynamic pressure at the jet propulsor exit. Similar to the pressure distributions, increasing the velocity ratio leads to reductions in the shear stress magnitude. As impingement angle is decreased, an upstream shift of the shear stress pattern is attributed to suction from the upstream low pressure region and is accompanied by a reduction in shear stress magnitude. One of the flow characteristics important for ground effect applications is the point where the upstream shear value returns to zero from a negative minimum. This point corresponds to the upstream wall jet / ground vortex separation point. The size of this negative shear region corresponds to the size of the ground vortex. At the moderate ground distance of r/D = 12 and velocity ratio = 0.3 the ground vortex vanishes as cross flow prevents jet impingement.

The downstream wall jet profiles are shown in Figs. 5.14e, f, at x/D = 10, corresponding to 10 jet widths downstream of the point where the jet centerline crosses the ground plane. It should be noted that the stagnation point occurs at different locations upstream of this cut depending on the configuration. However, for practical applications we are concerned mainly with the profile occurring at a consistent location with respect to the jet source. The jet at small ground distance of r/D = 4 impinges in the potential core region and yields a thin jet of high magnitude. The spreading at larger ground distances increases the wall jet thickness and reduces peak velocity.

For a given r/D it appears that reducing impingement angle only shows significant effects with cross flow imposed. At smaller impingement angle more pronounced jet thinning and larger peak velocity magnitudes are noticed. In addition, the cases at r/D = 12 with velocity ratio of 0.3 confirm that the cross-flow velocity has indeed forced the jet downstream as velocity peaks lie at noticeable distances above the wall.

As suggested by pressure, wall jet, and shear distributions, the varying velocity ratio only has significant effect at moderate to large ground distances. At r/D=4 the minimal variance is due to existence of significant potential core in the jet flow approaching the ground. On the other hand, at larger ground distances impinging jets weaken as they spread over a large spatial distance. These weaker jets show much more pronounced effects of velocity ratio, ground height, and impingement angle. At intermediate values of cross-flow velocity ratios 0.1 and 0.2 (not presented in details here), calculation results show gradual transitions in the discussed flow phenomena similar to the streamlines of Fig. 5.13.

The oblique impinging jet stagnates at the point of highest pressure on the ground. Figure 5.15a shows this point as a function of velocity ratio and jet propulsor position. The observed trends suggest that the stagnation point shifts farther upstream at lower impingement angles, where the entrainment in the zone between the propulsor and the ground pulls the jet to the wall. Again, at small ground distances there are relatively small stagnation point shifts in comparison with the jet flow at the larger ground distances. As the cross flow is increased, the stagnation point is forced downstream by the cross flow with greater shift slopes for larger ground distances. Configurations without impingement have been left off the figure.

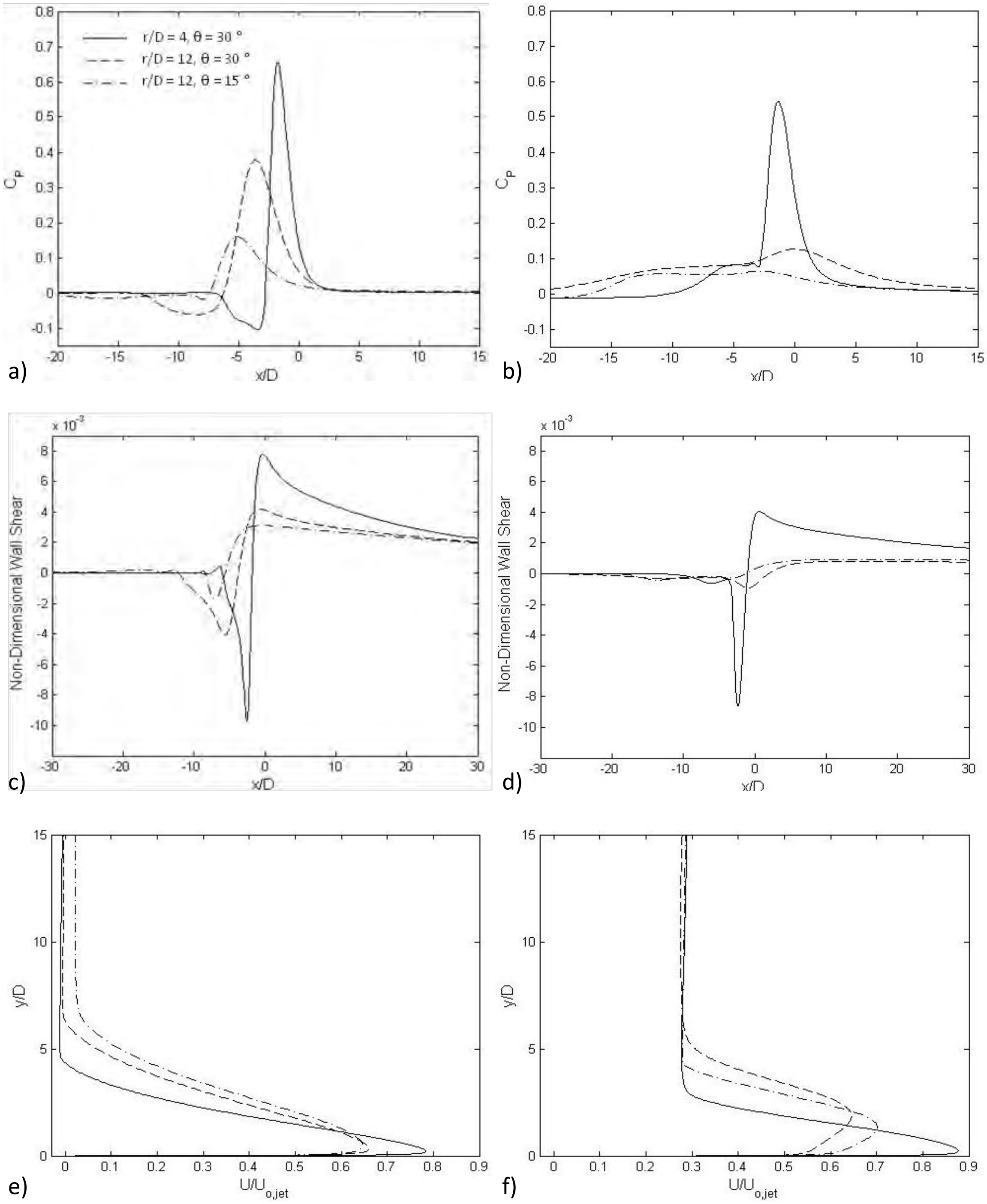

Fig. 5.14: Oblique jet characteristics at wall with Re = $2\cdot10^4$: a) pressure at velocity ratio = 0; b) pressure at velocity ratio = 0.3; c) shear stress at velocity ratio = 0; d) shear at velocity ratio = 0.3; e) wall jet at x/D = 10 and velocity ratio = 0; f) wall jet at x/D = 10 and velocity ratio = 0.3.

The ground vortex, a commonly studied flow phenomenon of V/STOL craft, is clearly observed in Fig. 5.11. The ground vortex separation point shown in Fig. 5.15b corresponds to the point at which the upstream wall jet separates. In contrast to V/STOL craft, the upstream ground vortex is additionally found in the case obliquely impinging jet without cross flow. As mentioned above, in this static regime the ground vortex develops as a result of the jet propulsor entrainment. In all cases, as cross flow is increased, the vortex separation point shifts downstream. As the impingement angle is decreased, the ground vortex separation also shifts downstream. In regimes with small to moderate ground distances and impingement angles chosen, the separation point shifts upstream with increasing ground distance due to the assistance of jet propulsor suction on wall jet separation (meaning early separation at small ground distances). However, at sufficiently larger ground distances this trend is expected to reverse as the jet propulsor will lack significant contribution to the wall jet separation. Cases with no ground vortex are not included in Fig. 5.15b.

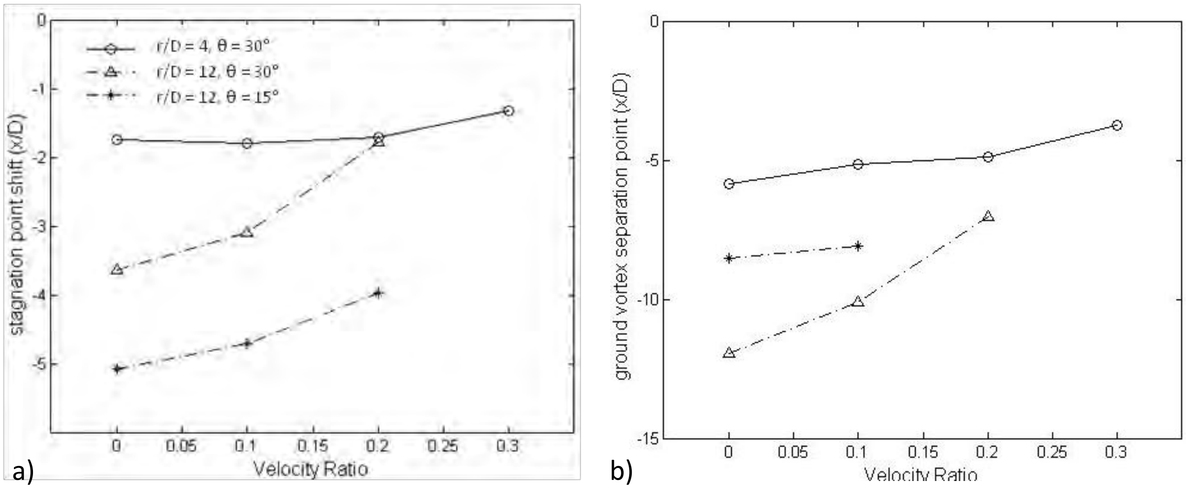

Fig. 5.15: PAR impingement data with Re = $2 \cdot 10^4$: a) stagnation point shift; b) ground vortex separation point.

In addition to the impingement flow structures, the momentum in the downstream wall jet is critical for PAR design applications. As discussed in the introduction, the amount of momentum flow in between the platform and the ground will be proportional to generated lift. Therefore, it is desirable to quantify this parameter for different downstream PAR platform placements. The downstream momentum normalized by the jet reference momentum ($M_0 = \rho U_{o,jet}^2 D$) is defined as,

$$\frac{M_+}{M_0} = \frac{\int \rho U^2 dy}{\rho {U_{o,jet}}^2 D}, \tag{5-3}$$

where U is the mean flow velocity component in the x-direction at a cross sectional cut taken 5 jet widths downstream of the point where the jet centerline intersects the ground and $U_{o,jet}$ is the average velocity at the jet exit. The integral in Eq. (5-3) is computed from the ground surface to a specific height. Figures 5.16a, b, and c show the downstream momentum characteristics for heights of 6D, 2D, and 1D respectively. With reference to Figs. 5.14e, it is clear that Fig. 5.16a corresponds to a case in which the full jet is captured underneath the platform, while Fig. 5.16b and c correspond to the so-called overfilled flow where some fraction of incident jet would pass over the PAR platform. At all heights a greater amount of momentum is transferred downstream with reduced impingement angle at the same r/D. In Fig. 5.16a, where the entire jet is captured, increasing jet propulsor ground distance yields larger downstream momentum due to reduction in cross flow blockage and impingement energy loss when ducted propulsor is further removed from downstream momentum capturing region. When the characteristic platform height is selected to be 1D or 2D, the greatest downstream momentum is achieved with the thin jet of r/D = 4. At these small platform heights, only a fraction of thick downstream jets (originated at large ground distances) will enter under the platform. In the case of r/D = 12 and θ = 30° the jet thickness significantly increases with velocity ratio (Fig. 5.14f) and downstream momentum will be further reduced. However, in the other cases studied cross flow augments the downstream jet momentum.

In determining the optimal location for the PAR platform one must know the effective height of the downstream jet centerline. This characteristic height can be defined by the equation

$$h = \frac{\int \rho\left(U^2 - {U_\infty}^2\right) y dy}{\int \rho\left(U^2 - {U_\infty}^2\right) dy}, \tag{5-4}$$

where y is the vertical distance from the point of interest to the ground and U_∞ is the upstream cross-flow velocity. Figure 5.16d shows this parameter while integrating to a height of 6D, encompassing all downstream wall jet behavior. Clearly, the jet configuration at small ground distance of r/D = 4 produces the smallest jet height, while as cross flow is implemented the jet spreading reduces and the jet height decreases. This phenomenon also appears to take place for larger ground distances at static to low cross-flow velocities. However, for the jet configurations at larger ground distances there is a critical cross-flow velocity in which the trend reverses and the jet begins to further spread with cross flow yielding larger jet height. In the case of the configuration with small impingement angle this occurs when the jet no longer impinges and is carried above the ground surface in the downstream direction. However, when the jet source is at r/D = 12 and θ = 30°, the downstream jet thickens quickly at large cross-flow velocities, and the jet height significantly increases. Depending on the jet configuration, a chart similar to that of Fig. 5.16d can be used to determine the proper platform placement in order to effectively utilize jet momentum for generating the platform air cushion.

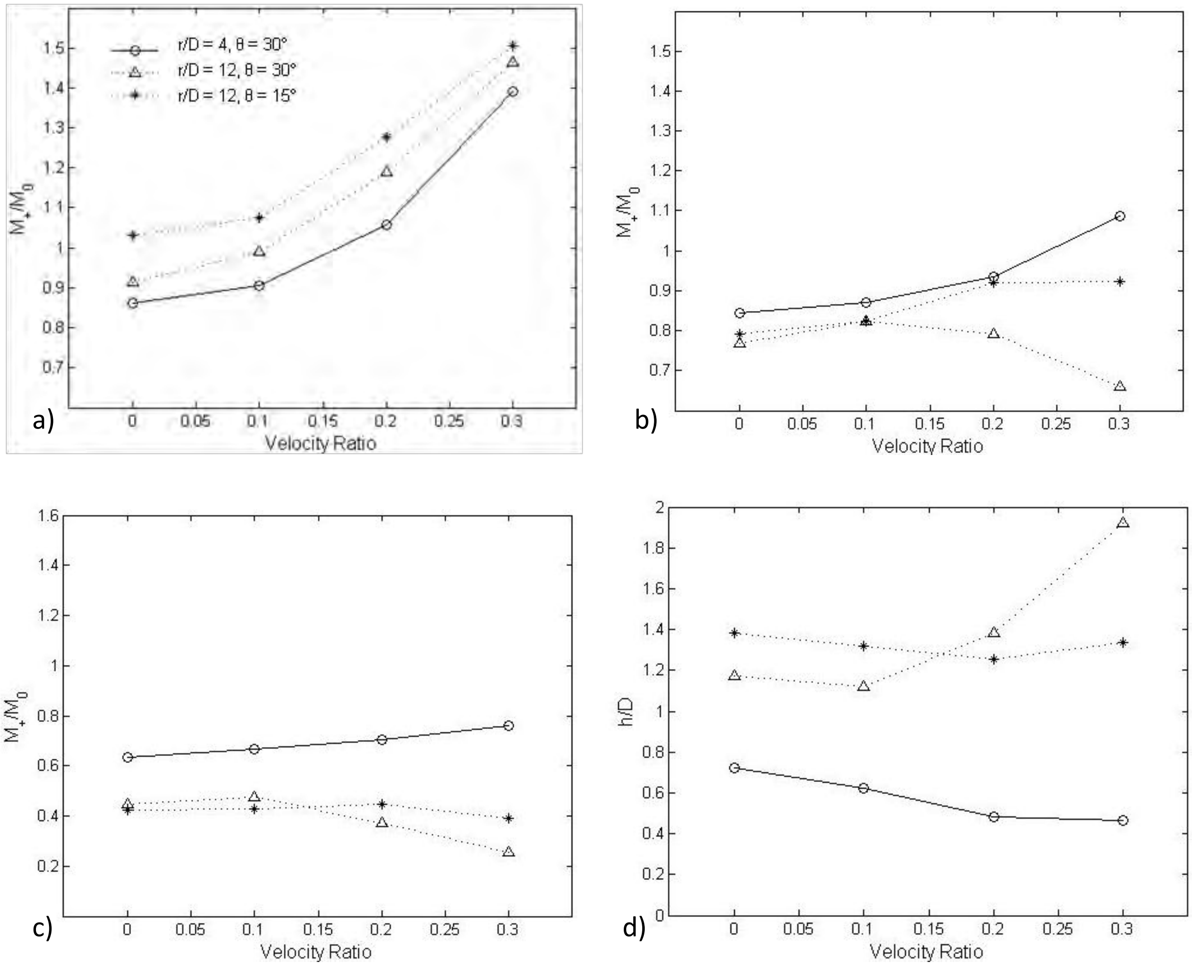

Fig. 5.16: PAR momentum parameters with Re = $2\cdot10^4$ at x/D = 5: a) downstream momentum ratio for height = 6D; b) downstream momentum ratio for height = 2D; c) downstream momentum ratio for height = 1D; d) downstream jet centerline height.

With many applications of impinging jets, it is important to understand variations in flow behavior for a variety of scales. Oblique impingement scale dependence has been studied for Reynolds numbers of $1\cdot10^3$, $5\cdot10^3$, $2\cdot10^4$, and $4\cdot10^4$ for jet configurations of r/D = 12, θ = 30°, and velocity ratios of 0 and 0.3. The ground pressure distributions and downstream wall jet profiles are shown in Fig. 5.17. The pressure distributions without cross flow in Fig. 5.17a demonstrate a weakening jet (lower peak stagnation point) at low Reynolds numbers where contributions of viscous forces are more prominent. However, as the Reynolds number increases, solutions tend to converge to a common stagnation pressure profile. In the case where cross flow carries the jet downstream, no significant pressure changes with Reynolds number are apparent (Fig. 5.17b). Similar scale effect behavior is presented in the downstream wall jet profiles of Figs. 5.17c and 5.17d. At sufficiently large Reynolds numbers in the studied range, changes in scale have little effect on the flow. However, the wall jet profiles clearly show the increased viscous jet spreading at lower Reynolds numbers. This increased jet thickness and reduced peak velocity are present in both cases with and without cross flow.

Scale effects on other jet characteristics are shown in Fig. 5.18. Figure 5.18a presents an upstream stagnation point shift with reducing Reynolds number, which implies that the thicker and weaker jet is pulled further upstream before impingement. The downstream momentum flow results depend on scale and are shown in Figs. 5.18b, c, d. At low Reynolds numbers the momentum height significantly increases (Fig. 5.18b) in accordance with the thickening downstream velocity profile (Fig. 5.17c, d). In contrast, the downstream momentum ratio is nearly constant when calculated over the full wall jet (vertical integration up to 6D from the wall), as shown in Fig. 5.18c. However, at the lower reference height (Fig. 5.18d) the momentum transferred in the downstream region of interest is reduced as portions of the thicker jet pass over this height at low Reynolds numbers. In the range of Reynolds numbers studied, scale effects are found to be significant only at very small Reynolds number conditions where the obliquely impinging jet spreads much more quickly.

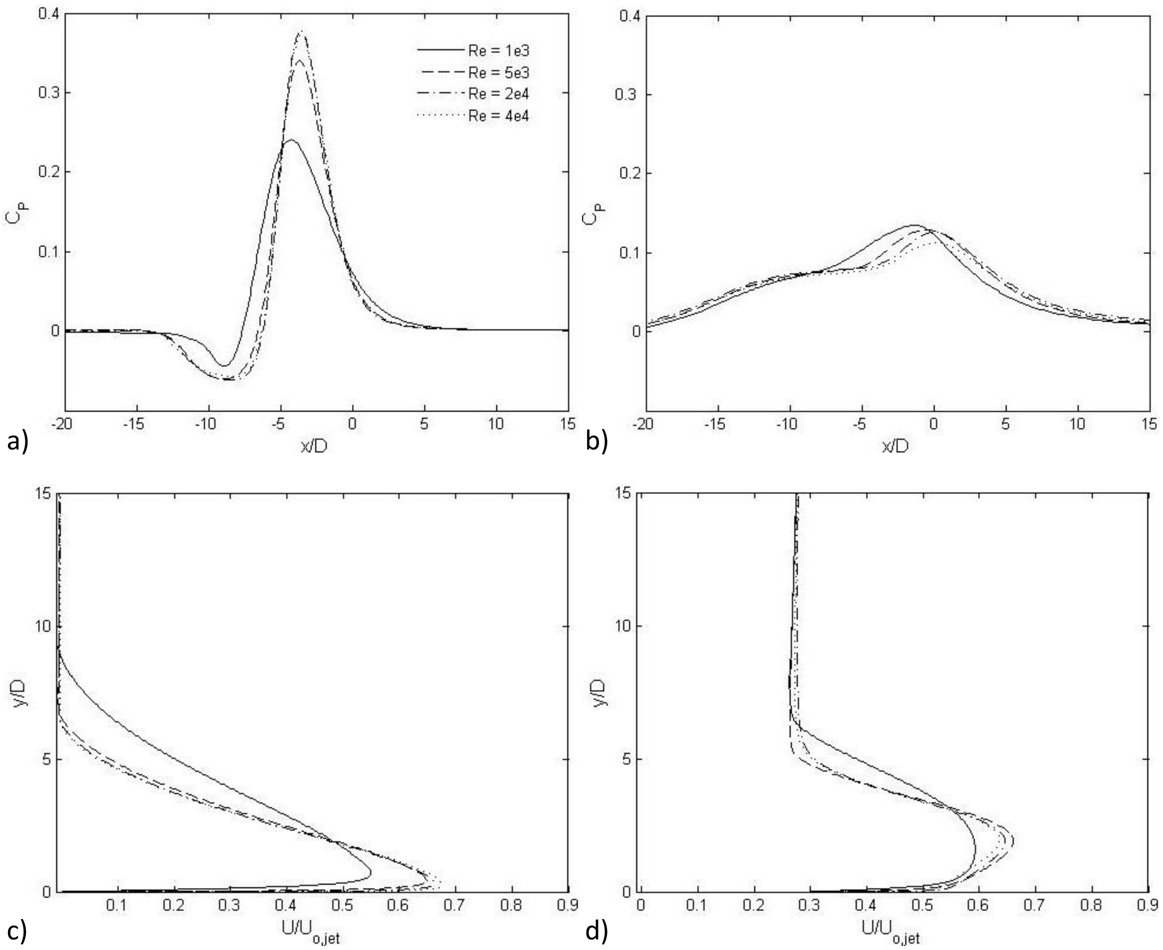

Fig. 5.17. Scale effects on flow with r/D = 12, θ = 30°: a) ground pressure without cross flow; b) ground pressure with velocity ratio of 0.3; c) downstream wall jet profile at x/D = 10 without cross flow; d) downstream wall jet profile at x/D = 10 with velocity ratio of 0.3.

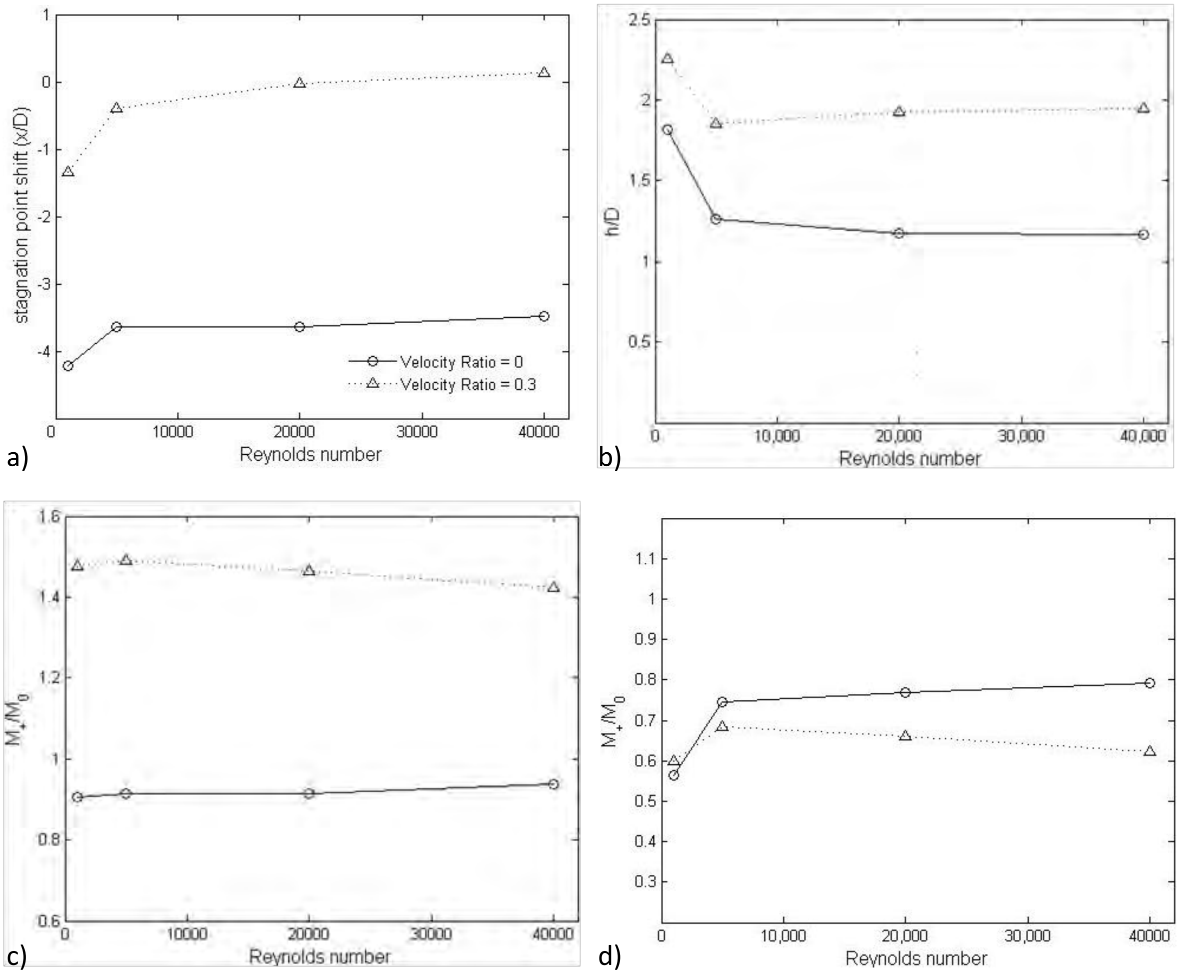

Fig. 5.18. Scale effects on performance with r/D = 12, θ = 30°: a) stagnation point shift; b) momentum height at x/D = 5; c) downstream momentum ratio with integration limit at 6D; d) downstream momentum ratio with integration limit at 2D.

5.3 Concluding remarks

A two-dimensional numerical model of a jet propulsor is developed for applications where modeling of the propulsor suction and entrainment are essential. The ducted momentum source is shown to reasonably agree with empirical data for free jet, and jet normally and obliquely impinging on the ground. Additionally it is similar to theoretical jet models (Batchelor, 1973).

In the calculated oblique jet configurations relevant to Power-Augmented-Ram and ground effect systems, the jet ingestion phenomenon is observed for relatively large impingement angles and small ground distances. As opposed to V/STOL vehicles with much higher jet angles, this ingestion behavior occurs at zero speed and is reduced with increase of cross flow. The ingestion regimes should be avoided on PAR vehicles as the jets may pass unwanted material or exhaust through the jet propulsor with the possibility of causing propulsor failure or reduced efficiency.

The accomplished parametric study provides insight on operating parameters for a PAR propulsor. Greater ground heights are beneficial as they avoid jet propulsor ingestion. Similarly, a reduction of impingement angle also yields a small or non-existent ground vortex while simultaneously transferring a greater amount of momentum downstream. However, it should be kept in mind that higher jet propulsor placement at smaller angles could lead to an undesirably large increase of the front part of vehicles unusable for payload placement. Increasing cross flow (i.e., PAR vehicle forward speed) also reduces chances for ingestion and depending on configuration can also increase the momentum flow downstream.

It has also been shown that both the ground shear stress and pressure stagnation point shift upstream and reduce in magnitude with reducing impingement angle. Similarly, as the cross-flow velocity increases both the ground shear stress and pressure stagnation values significantly decrease due to the lack of impingement or downstream displacement of the stagnation point. Although the impingement angle and cross-flow velocity have shown to have an impact in most configurations it is apparent that there is reduced dependence on all parameters when small ground distances are used.

For the PAR vehicle design it is important to know characteristics of the momentum distribution in the flow approaching the platform, such as the total momentum and the position of maximum momentum flux. For generating higher PAR lift at low speeds, lower platform height suggests using lower jet propulsor position. Smaller jet propulsor angles are favorable as long as most of the downstream jet passes under the platform. While reducing platform height is usually beneficial on flat underlying surfaces, the operating conditions on rough ground or water surfaces may require higher clearances.

Lastly, the Reynolds number effects in the studied range have shown to be relatively insignificant at moderate to high values, while small Reynolds numbers appear to yield jets with much more prominent viscous effects which thicken the jets and reduce their peak velocities.

Although Chapter 5 presents important jet propulsor impingement data for the common use on a ground-effect vehicle, an in depth study of the PAR vehicle will be approached in Chapter 6. This will included a description of the fundamental flow patterns including a discussion of the interaction between the jet propulsor and PAR platform in ground proximity.

CHAPTER SIX

PAR PLATFORM WITH JET AUGMENTATION AND FLAP

6.1 Introduction

With the focus of this thesis on the study of ground-effect vehicles with flap and jet components; Chapter 6 ties the previous studies together by studying a ground-effect vehicle with both jet augmentation and flap implemented. Configurations have been chosen which correspond to practical ground-effect vehicles with focus on the beneficial operating regimes of both the platform flaps (Chapter 4) and jet propulsors (Chapter 5). Although the performance optimization of the PARV is the driving force for this work, only an exploratory design study of fundamental interactions between the jet propulsor and platform-flap system are currently undertaken. These results not only apply to the current PARV design, but may also provide beneficial information for PAR-WIG, V/STOL craft, and common aircraft operation during takeoff and landing.

Although the results may benefit many areas, the application of focus for the current Chapter is the PARV concept under development (Gallington 1987, Kirillovyh and Privalov 1996, Matveev and Malhiot 2007, Matveev 2008). For a detailed explanation of this concept refer to section 1.4.2 and Chapter 5. The intention of introducing jet augmentation to ground-effect vehicles is to provide vehicle support at low speeds where passive aerodynamic lift is not sufficient. In such cases the PAR concept uses a row of jet propulsors upstream of the platform flap system in order to inject momentum under the platform. The trailing edge flap traps this flow under the platform, creating a pressure cushion which provides the necessary lift.

Studies of PARV with flap control have yet to be approached with viscous numerical methods in the literature. As mentioned earlier in this thesis, inviscid solutions (Smithey et al., 1977) have been used for limited flap studies, but viscous methods (Hirata and Hino 1997, Kwag 1997) have not considered effects of a flap. Additionally, results of previous viscous methods are questionable as they assume laminar flow or lack validation of jet propulsor modeling procedures. The only known experimental data for current PARV are platform pressure distributions and recovered thrust data taken in static conditions by Soderlund and Matveev (2008) and Matveev (2008). Other PAR-WIG studies have used simplifying assumptions to analyze expected cruising performance and design feasibility (Ando, 1993). Due to the lack of reliable numerical PARV or PAR-WIG literature, the current model builds on the previous work by validating and studying the viscous PARV with trailing edge flap.

With relatively little information on PARV operating conditions, the current exploratory study will determine vehicle performance for three fundamental PARV flight regimes. First, the static case will be studied in which the flap is significantly deflected in the hovering configuration with jets solely augmenting the lift. The second regime will consider low vehicle forward speed where jet propulsor provides both lift and thrust. The final configuration studies jet propulsor configurations at high speeds. In such cases we have previously assumed that the jet propulsor was unnecessary and approximated the high speed PAR flight with a platform-flap system and no jet propulsor. In this section the validity of this assumption will be tested, and any interactions between the jet propulsor and platform-flap system at high speeds will be noted.

6.2 Numerical Techniques

The jet propulsor and trailing edge flap are introduced to the ground-effect vehicle as shown in Fig. 6.1. This geometry represents the PARV described in section 1.4.2 with platform approximated with a flat plate similar to the radio controlled PAR models developed at Washington State University (Matveev, 2007). The jet propulsor width and length are D and L_D

while it is located a distance L_j above the ground surface, a distance H_j in front of the platform leading edge, and rotated at an angle θ from the horizontal. The platform of length L_p is then positioned a distance h above the ground with a plain flap of length L_f whose trailing edge is a distance h_f above the ground surface. The current geometry imposes an attack angle of 0° with the cross-flow velocity entering horizontally from the left side of the domain at a value of U_∞. It should be noted that in configuration 6 (Table 6.2) the flat plate platform is replaced with an NACA 4406 airfoil at an attack angle of 1° and a plain flap of length L_f. In all configurations the force and pressure coefficients used are defined as in Appendix A.

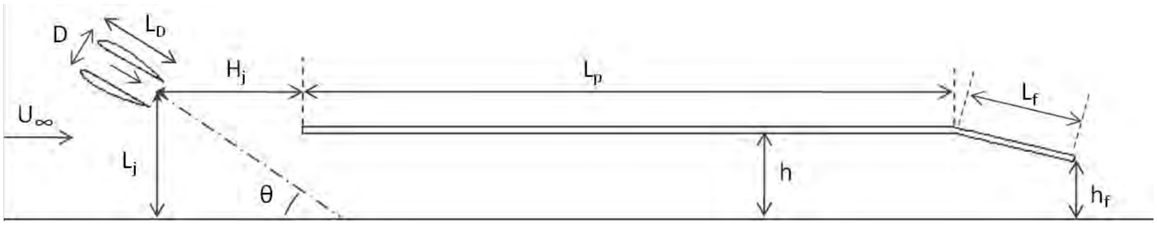

Fig. 6.1. PAR geometry and parameter definitions.

With the geometry defined, the governing equations and numerical methods must be established. Due to the successful use and validation of the steady, two-dimensional, incompressible, constant viscosity, turbulent RANS equations (2-4, 2- 5) for individual jet propulsor and platform-flap configurations, they will also be employed for the PARV study. Similar to previous jet propulsor studies the isotropic Boussinesq approximation is made, with closure provided for the RANS equations by the standard k-ε turbulence model. Although the Spalart-Allmaras model worked well for the airfoil-flap configuration, it is not used for the PARV application as it cannot accurately predict the spreading of a free jet (Wilcox, 2006). It should be noted that the use of the k-ε model is also questionable for strong adverse pressure gradients, but it will be validated against experimental data in section 6.3 and is thought to be sufficient for the current design study (as exact drag values are of minor importance). This closed set of governing equations formed by the RANS equations with the k-ε turbulence model are solved numerically by FLUENT 6.3 with the segregated SIMPLE algorithm while implementing the 2nd order discretization scheme for pressure and 2nd order upwind scheme for momentum, kinetic energy, and turbulent dissipation. In addition, the oblique jet propulsor upstream of the platform will be defined in an identical fashion to the detailed explanation in section 5.1.1 which is similar to the theoretical jet of Batchelor (1973). In which a momentum source is defined as a single row of cells across the ducted propulsor created from two Clark-Y airfoils. Chapter 5 emphasizes the performance of this model and its ability to model a physical jet propulsor. All solution parameters for the PARV study can be found in Table 6.1.

The boundary conditions applied to the current computational domain are very similar to those applied to the two components of the flow individually. In the static conditions, without cross flow, the upstream, top, and downstream boundaries have been set at ambient pressure conditions while the ground condition is a stationary no-slip wall condition. When cross flow is present, the upstream and top boundaries specify the uniform free-stream velocity (vehicle forward speed) while the downstream boundary again uses the ambient pressure. As mentioned in previous chapters, in ground proximity with cross flow present the ground boundary condition is specified as a no-slip wall moving at the free stream velocity (Barber et al., 1998). In all cases the duct and platform are modeled as no-slip stationary walls.

The domain extends one vehicle length upstream, downstream, and above the PARV while the distance to the bottom of the domain is specified by the ground heights of the different components of the vehicle (H_j, h, h_f). This domain size was chosen as it is larger than the size of any jet impingement structures found in the oblique impinging jets studied in Chapter 5. Additionally, it was observed in Chapter 4 that the ground effect suppressed unsteady effects and contained platform-flap effects to the near vehicle vicinity. Although this domain is relatively small, it should be sufficient for this initial PARV design study.

density	1.225 kg/m^3
viscosity	1.7894e-5 kg/m-s
jet width	0.03 m
duct length	0.08 m
impingement angle	0° and 30°
cross flow velocity	0, 5, and 10 m/s
jet thrust	0, 18 N/m
solver	2D steady
pressure-velocity coupling	SIMPLE
press. descretization	2nd order
mom. descretization	2nd order upwind
mod. viscosity descretization	2nd order upwind
turbulence model	Standard k-ε
Y+	0-1 (near wall)

Table 6.1 Solution parameters for PARV configuration studies.

The mesh used in the current study is a structured quad mesh as shown in Fig. 6.2. Due to the extreme mesh density, details of the jet exit and platform-flap regions are shown as close-ups under the schematic of the full PARV. In the jet exit and impingement regions the cells are aligned in the flow direction to reduce any numerical dissipation. As the flow approaches the underside of the platform the mesh then aligns in the horizontal direction with near wall refinement to a mesh size of 0.05 mm. This near wall cell height lies in the viscous sub-layer with a non-dimensional y^+ value of approximately 1. To account for the near wall behavior, enhanced wall functions are used with the k-ε turbulence model. Although the flat plate platform mesh is shown, configuration 6 uses a similar mesh density only with a modified geometry. The mesh density was chosen according to the mesh independent solutions found for the individual components studied in Chapters 4 and 5. All major flow patterns are captured with this mesh and due to the exploratory nature of the current design study, a full independence study is not completed for PARV.

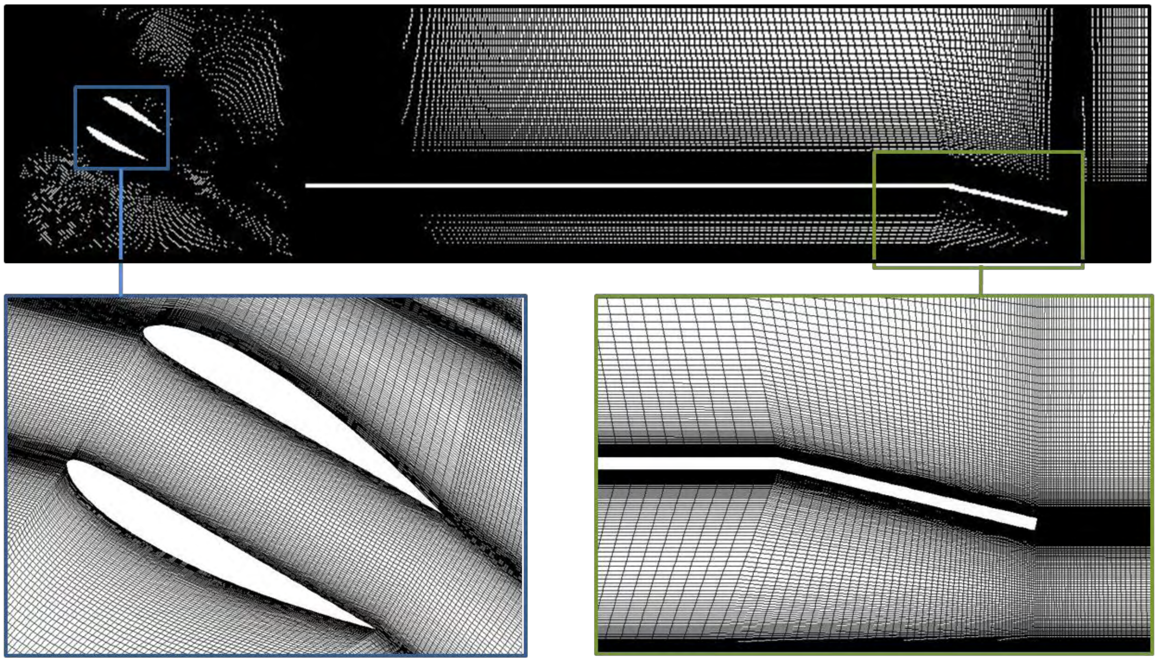

Fig. 6.2 Computational near-wall mesh with close-up views of ducted propulsor and trailing edge flap. Only a portion of the mesh is presented, domain extents further in upstream, top, and downstream directions.

6.3 Experimental Validation

Validation in modeling the interactions between a jet and aerodynamic platform in ground effect is provided by comparisons with experimental data of a static PAR craft taken by Soderlund and Matveev (2008). The experimental setup uses similar parameters to those shown in Fig 6.1, where a flat plate platform is sandwiched in between two endplates, with no gaps between the endplates and the ground. The upstream jet propulsor is created with a blower placed a distance L_j = 14 cm upstream of the platform leading edge, a distance H_j = 9 cm above the ground plane, and rotated an angle θ = 30° from the horizontal. Additionally the platform height is h = 7 cm, the platform length is L_p = 63 cm, and the flap length is L_f = 17 cm. It should be noted that the jet geometry studied here corresponds to a common PAR configuration. The blower used a large aspect ratio rectangular nozzle which created an approximately two-dimensional flow exiting from a jet width of D = 2 cm. Nearly constant pressure readings taken at several span-wise locations provide increased confidence in the two-dimensional assumption made for the PAR vehicle.

With the use of a blower for jet creation, the experimental studies neglected the behavior upstream of the jet exit and focused solely on the under platform pressures. Therefore, for validation runs, our computational domain will be further reduced in the upstream direction. Instead of internally specifying the jet, for this validation we have specified the jet inlet at a constant velocity along the upstream boundary. This modified domain is presented in Fig. 6.3a. The remaining boundaries are specified identically to the above explanation of numerical modeling techniques for the static case. The modified mesh is shown in Fig. 6.3b, and is of similar mesh density to the mesh shown in Fig. 6.2 only with a reduced upstream boundary to better model the experimental situation.

The blower velocity exit profile was experimentally taken with a pitot tube 3 cm downstream of the jet exit. The numerical data taken at the same location is compared with experiments in Fig. 6.4. It is apparent that the velocity profiles match up very nicely. The peak velocity occurs numerically at 15.3 m/s, corresponding to the numerical average exit velocity determined from the known blower momentum of 5.59 N. Small discrepancies are shown between the two sets of data and are expected as the blower exits with a fully turbulent flow which does not yield the potential core which is predicted with the velocity inlet. Even with these discrepancies it is apparent that the numerical mean flow at the exit is of a very similar nature to the experimental values and provides a good approximation of the experiments.

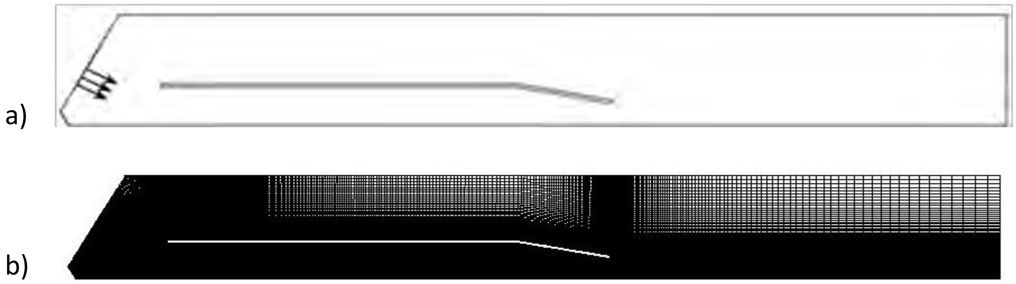

Fig. 6.3. PAR numerical model schematic with $h_f = 4$ cm: a) computational domain; b) meshed domain.

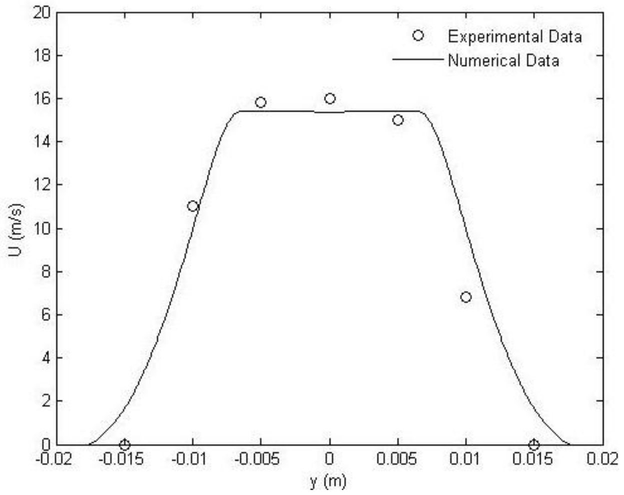

Fig. 6.4. Jet exit velocity distributions of 2 cm jet width taken 1.5 jet widths downstream.

Comparisons of pressure profiles along the bottom of the platform are compared with experimental values in Fig. 6.5. Experimental and numerical data show relatively good agreement at moderate to large flap heights of $h_f = 4$ and 6 cm. In the case of $h_f = 6$ cm the suction pressure is predicted at the channel entrance where the jet thickens via upstream entrainment. Although pressures in this suction region are slightly lower than experimental data, the pressures along the rear half of the platform match experiments very closely. At h_f = 4 cm the pressure trend at the entrance to the channel is very accurate while the rear half of the pressure distribution is slightly high. The small deviations seen in these two cases are acceptable as they are on the order of the experimental accuracy. With the flap nearly closed at h_f = 2 cm the numerical and experimental data begin to largely deviate. The numerical results significantly over-predict the pressure. Although the experimental uncertainty is highest in this case, it appears that the numerical error does not only surpass this, but also predicts the pressure cushion penetrating much nearer to the leading edge than experiments show.

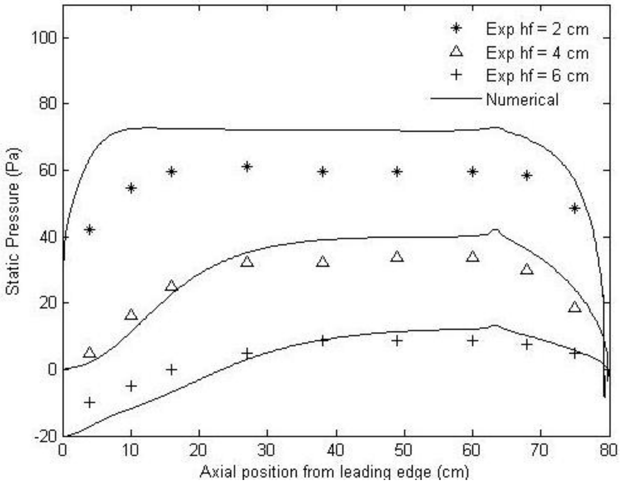

Fig. 6.5. Experimental comparison of platform pressure distributions. Average experimental error is approximately 5 Pa.

These experimental comparisons for static PAR performance validate predictions of jet-platform interactions and aerodynamic forces for moderate to small flap deflections. As the flap deflection is increased the qualitative trends still move in the correct direction; however, due to poor comparison with experimental data, no quantitative studies should be attempted in this region. Although this limits the models applicability; as shown in Chapter 4, the most beneficial regions of flap deflection lie well within the current capabilities (e.g. 5% of chord).

6.4 Results

The PARV geometry to be studied corresponds to the latest radio controlled model developed at Washington State University. The jet propulsor in the numerical model has a width of D = 3 cm, a length of L_D = 8 cm, and is placed a distance L_j = 15 cm upstream of the platform leading edge at a height of H_j = 13 cm. The platform length of L_j = 67 cm is located a height of h = 9 cm above the ground plane with a trailing edge flap of length L_f = 13 cm. Several configurations are studied which vary the jet impingement angle between 0 and 30° and the jet thrust (momentum source) between 0 and 18 N/m and platform type. Additionally the vehicle forward speed is varied between 0, 5, and 10 m/s while the flap height is varied between 3 and 6 cm.

The six configurations shown in Table 6.2 are studied to determine the general flow patterns and operating conditions of the PARV. Configuration 1 corresponds to the static condition using jet thrust and large flap deflection to augment lift in cases with no aerodynamic support. Configuration 2 mimics a PARV at small forward speeds where the aerodynamic lift is not sufficient to lift the vehicle. In this case the jet propulsor will provide additional vehicle lift and horizontal recovered thrust. Lastly, configurations 3-6 study the high speed PARV where aerodynamic lift will generally support the vehicle and jet augmentation is thought to be unnecessary. In this situation the jet propulsor will be implemented at 30° with and without jet thrust, and at 0° with jet thrust. With horizontal propulsor, the effects of platform type will be studied via a comparison of flat plate platform and an NACA 4406 wing section. Therefore, we may determine the best jet propulsor use in regimes where it is not necessarily a lifting device.

Configuration	U_∞ (m/s)	T_{jet} (N/m)	θ_{jet} (°)	h_f (m)	**Platform Type**
1	0	18	30	0.03	Flat plate
2	5	18	30	0.06	Flat plate
3	10	18	30	0.06	Flat plate
4	10	0	30	0.06	Flat plate
5	10	18	0	0.06	Flat plate
6	10	18	0	0.06	NACA 4406

Table 6.2 PARV configuration parameters.

Flow patterns for configuration 1 in the “hovering” regime are shown in Fig. 6.6. The velocity streamlines in Fig. 6.6a and pressure contours in Fig. 6.6c show that the jet impinges on the ground surface just upstream of the platform-flap structure. The majority of the flow is trapped underneath the platform while a fraction of the jet is re-directed upstream as a wall jet. As discovered in the oblique jet studies of Chapter 5, this upstream wall jet separates from the ground and creates a relatively large ground vortex upstream of the jet propulsor. Although this large vortex doesn’t appear to be directly entrained in the ducted jet source, it is expected to possibly detach particles from the ground surface or water from the water surface and ingest them into the jet propulsor. Therefore, the PARV design should attempt to minimize its operation in the hovering regime unless it can operate at reduced impingement angles or greater ground heights (Chapter 5). Although this configuration has poor ingestion properties, the majority of the flow is trapped under the platform, creating a pressure cushion which provides the necessary static lift. In static conditions no unusual interactions between the ducted propulsor and downstream platform are noticed.

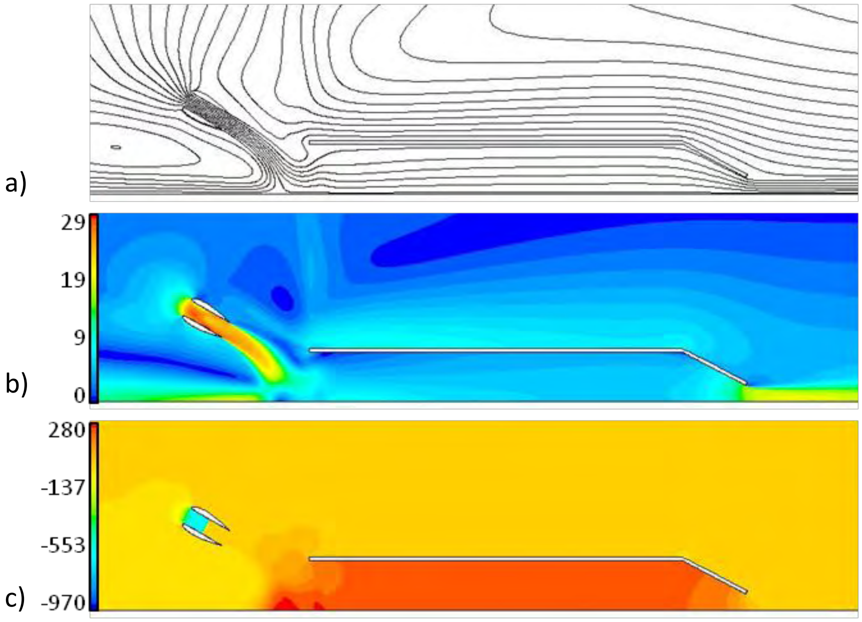

Fig. 6.6 Flow patterns for configuration 1: a) streamlines; b) velocity contours (m/s); c) static pressure contours (Pa).

The PARV is then set at a moderate forward speed (velocity ratio of ≈ 0.15) while reducing flap deflection (h_f = 6 cm) to increase forward speed efficiency by significantly reducing the pressure drag. The flow patterns of configuration 2 are presented in Fig. 6.7. The jet impinges on the ground with the majority of the flow being trapped underneath the platform. Again, a small portion of the impinging jet is re-directed upstream into the ground vortex. At these small forward speeds the ground vortex size is reduced but the upstream jet suction continues to cause jet propulsor ingestion. In such configurations the vehicle should ideally use a smaller impingement angle or greater ground height to avoid the propulsor ingestion. At these moderate speeds the majority of the jet momentum passes underneath the platform to partially augment the lift. Additionally, with the smaller flap deflection a larger portion of the jet momentum is used to increase the horizontal recovered thrust while the vehicle forward speed also contributes to the lift. Minimal interactions are noticed between the jet propulsor and the downstream platform.

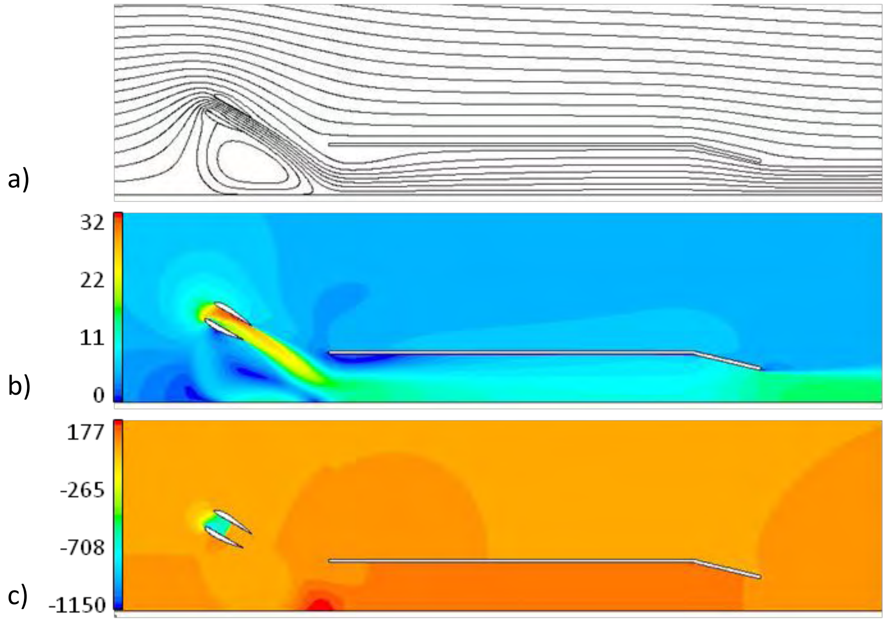

Fig. 6.7 Flow patterns for configuration 2: a) streamlines; b) velocity contours (m/s); c) static pressure contours (Pa).

In configuration 3, the vehicle forward speed is increased from a moderate value to a high speed (10 m/s). The flow patterns of configuration 3 are shown in Fig. 6.8. At high speeds the cross flow to jet velocity ratio is around 0.3. Similar to the previous impinging jet study, at such large velocity ratios the cross-flow velocity carries the jet downstream before it impinges on the ground surface. In this case the jet impinges on the front of the PAR platform instead. This behavior can be observed in the velocity and pressure plots of Fig. 6.8. Ultimately, this jet impingement creates a large drag on the vehicle which reduces the recovered thrust at high speeds. Although this causes a decrease in performance, ingestion is avoided at high forward speeds. Additionally, direct interaction between the jet propulsor and platform is observed. The jet propulsor accelerates a region of the fluid which impinges on the front of the platform and is split between upper and lower regions of the platform.

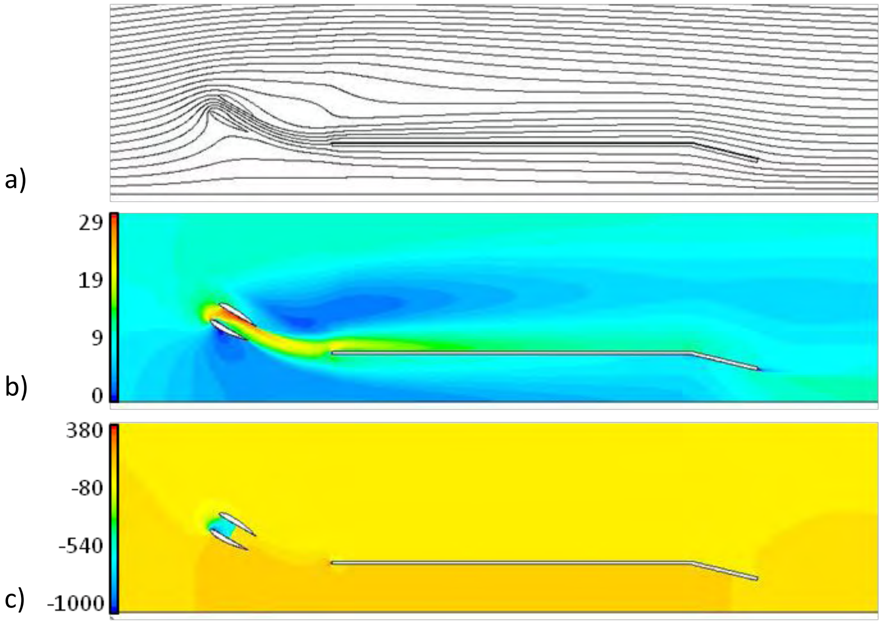

Fig. 6.8 Flow patterns for configuration 3: a) streamlines; b) velocity contours (m/s); c) static pressure contours (Pa).

In an attempt to avoid direct jet impingement on the platform, configuration 4 is studied with the same geometry as configuration 3, only with upstream jet propulsor shutoff (providing zero thrust). The flow patterns of configuration 4 are shown in Fig. 6.9. As hoped, no jet impingement occurs and flow patterns originate from the forward speed of the vehicle only. In this configuration significant interactions are observed between the upstream jet propulsor and the downstream platform-flap system. Without propulsor thrust, no flow is entrained along the jet propulsor axis, and the propulsor duct acts as a blunt body with a large separation zone on its upper side. Due to the pressure cushion underneath the vehicle, increased amounts of flow are forced between the platform and the propulsor, causing additional separation at the leading edge of the platform. These separation zones significantly modify the platform flow while increasing the vehicle drag. With the PAR propulsor shut off in this configuration, other devices would be necessary to overcome the vehicle drag.

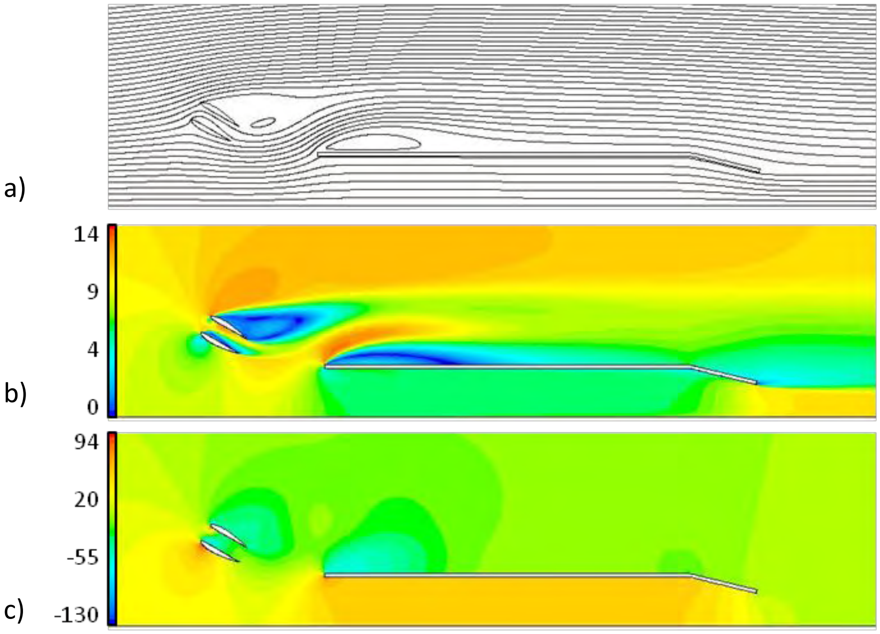

Fig. 6.9 Flow patterns for configuration 4: a) streamlines; b) velocity contours (m/s); c) static pressure contours (Pa).

In an effort to increase high speed PARV performance, the jet propulsor is implemented in a horizontal position while providing thrust. Ideally this placement will avoid the increased blunt body drag at high speeds while recovering a significant portion of the jet propulsor horizontal thrust. This setup is demonstrated by flow patterns in Fig. 6.10 where the horizontal ducted propulsor reduces blunt body behavior and avoids platform impingement. Although the jet is not directly feeding the vehicle pressure cushion, it is expected to slightly improve the lift by accelerating flow over the nose of the platform (which reduces separation and increases upper surface suction). As shown in other high speed configurations, interactions occur between the jet propulsor and downstream platform-flap system. The jet propulsor accelerates flow over the upper side of the vehicle.

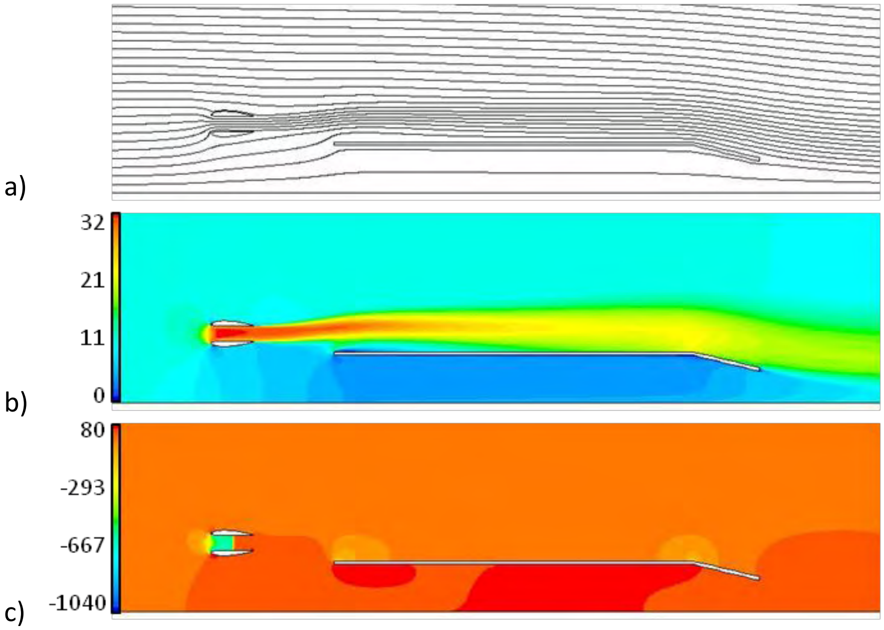

Fig. 6.10 Flow patterns for configuration 5: a) streamlines; b) velocity contours (m/s); c) static pressure contours (Pa).

Lastly, the high speed setup in configuration 5 is repeated for a modified platform geometry. In configuration 6, the flat plate platform is replaced by an NACA 4406 wing section with identical ground height and plain flap deflection. In order to provide a nearly flat bottom surface the wing section has been rotated to an attack angle of 1°. The flow patterns shown in Fig. 6.11 are very similar to those of configuration 5. The only significant differences in flow appear to be in the greater thickness of the airfoil and the curved upper surface which is more effective in reducing separation along the leading or trailing edges of the platform.

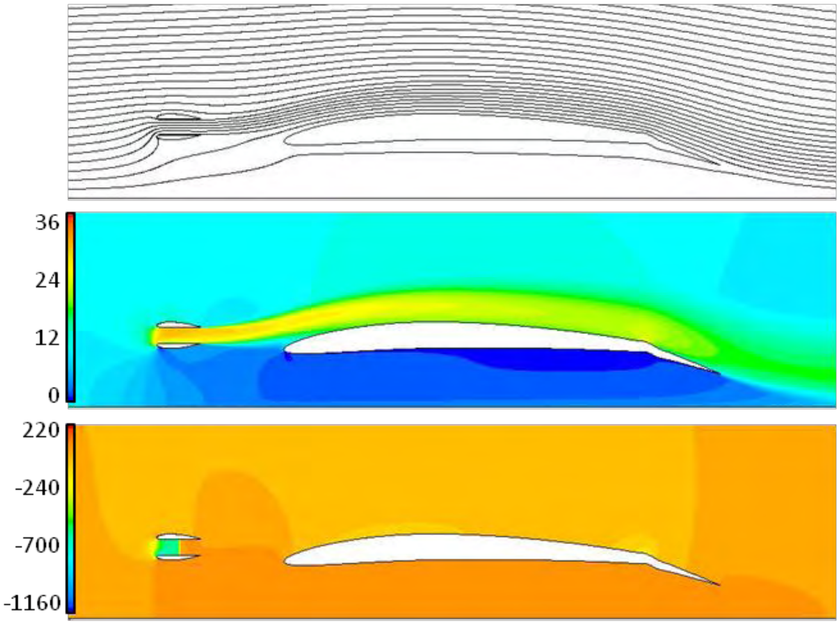

Fig. 6.11 Flow patterns for configuration 6: a) streamlines; b) velocity contours (m/s); c) static pressure contours (Pa).

For further understanding, the platform pressure distributions have been compared in Fig. 6.12. It should be noted that the large spikes in pressure at the leading edge of the platform are due to the nose impingement and jet behavior around the sharp edge. These extremities are confined to small areas and, therefore, have little impact on the aerodynamic lift which is approximated by the area between upper and lower platform surfaces. Configuration 6 has been left out of this comparison due to its modified geometry which prevents easy comparison.

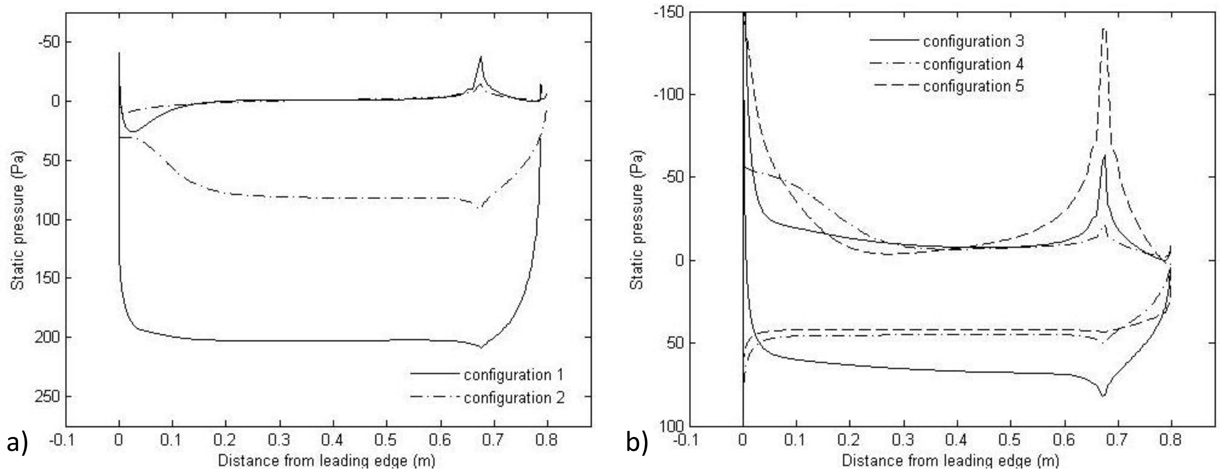

Fig. 6.12 Static pressure distributions on platform: a) zero to moderate speed; b) high speed.

While the flow patterns for configurations 1-6 have provided a conceptual idea of the component interactions for each configuration, aerodynamic forces on the PARV are still required for proper comparison of configurations. As only a select set of configurations have been run, the aerodynamic performance parameters for all six configurations have been presented in Table 6.3. The lift and drag forces have been presented for platform only. Forces on the idealized upstream jet propulsor have been neglected in this study as they are a small fraction of the platform values, and a three dimensional model or empirical correlation would be necessary to account for jet propulsor supports. Additionally the platform lift-to-drag ratio is presented and PARV recovered thrust is defined as,

$$T_R = T\cos(\theta) - D'_{platform} , \tag{6-1}$$

where T is the user specified propulsor thrust and D'_{platform} is the platform drag. The recovered thrust is the vehicle thrust in the horizontal direction after the platform drag is subtracted. A value of zero recovered thrust corresponds to a constant vehicle speed while positive and negative values indicate acceleration or deceleration respectively. This recovered thrust value is expected to decrease with increasing vehicle forward speed due to drag originating from the vehicle forward speed.

In analyzing the performance characteristics of the static and moderate forward speed configurations, a few relationships are visible. It is clear that at greater flap deflections a larger amount of flow is trapped, and the increasing pressure cushion yields increased lift and drag. Therefore, as the PARV transfers from the "hovering" configuration to the moderate forward speed it sees a reduction in lift (although aerodynamic lift increases) and a reduction in drag. The significant reduction in drag with reduction of flap deflection nearly quadruples the recovered thrust and doubles the aerodynamic efficiency. This behavior clearly yields an increase in the vehicle forward speed, and a much more beneficial operating regime. However, when static operation is necessary, the large flap deflection will successfully support the PARV.

Configuration	**L'$_{platform}$** (N)	**D'$_{platform}$** (N)	**L'/D'$_{platform}$**	**T$_R$** (N)
1	154.35	11.72	13.17	3.87
2	57.49	2.48	23.18	13.11
3	62.17	5.12	12.14	10.468
4	48.77	1.79	27.24	-1.79
5	54.82	3.02	18.15	14.98
6	81.68	5.08	16.08	12.92

Table 6.3 PARV aerodynamic forces and performance measures.

In addition to the viscous numerical lift values we have obtained, we can also use the two-dimensional, steady, potential flow solution originally developed by Gallington et al. (1976) and later modified by Matveev (2008). This simplified model predicts the platform lift, L'$_{platform}$,

$$L'_{platform} = T\left(\frac{1-(h_f/h)^2}{2h_j}\right)\left(\frac{1+\cos\theta}{2}\right)\left(L_p + L_f\right), \quad (6\text{-}2)$$

where h_j represents the jet thickness entering the channel between the PAR platform and the ground and L_p and L_f are the lengths of the platform and flap. This method is valid when the below criteria is satisfied,

$$h_j > h_f + \frac{h(1-h_f/h)}{4}. \tag{6-3}$$

The only configuration which meets this "overfilled" criterion is configuration 1 where flow visibly fills the channel and is pushed over the front of the platform. In this case, the jet thickness at the platform leading edge is approximated by the height of the most extreme streamline in Fig. 6.6a. This is the outermost streamline which passes under the platform at a height of about h_j = 4.5 cm instead of being forced above. The approximate potential flow lift is obtained for this configuration as $L'_{platfrom}$ = 132.7 N. Although the current jet height is an approximation, the lift is within 15% of the viscous results and likely could be much more accurate with a more precise determination of jet height. Overall the simplified potential flow theory is limited in its applicability, but validates that the current viscous numerical results are adequate.

With reasonable results at low and moderate speeds, we turn our attention to the performance characteristics for the 4 high speed configurations. As expected the drag decreases when jet propulsor is moved horizontal or is shutoff. This is explained as configuration 3 yields a large drag when the jet impinges on the platform, horizontal configurations 5 and 6 avoid this jet impingement and reduce drag; a further drag reduction is obtained by shutting off the propulsor thrust. The increased drag with airfoil implemented is due to the increased platform thickness in comparison with the flat plate. In a situation with the airfoil and platform of similar thickness it is expected that the streamlined airfoil will yield a smaller drag.

On the other hand, flat plate platform lift is greatest for configuration 3 in which the jet partially augments the pressure cushion and produces vehicle lift. Configurations 4 and 5 rely mainly on passive aerodynamic lift, with configuration 5 producing a greater lift due to the above platform jet acceleration increasing suction pressure and avoiding leading edge separation. However, the airfoil configuration yields the greatest lift due to the platform curvature which significantly accelerates flow over the upper surface. The lift-to-drag ratio or aerodynamic efficiency increases in the same order as drag decreases. For this reason it appears that vehicle drag is a driving force for PARV efficiency, and configurations with zero jet thrust are most efficient. However, when jet thrust is necessary to increase lift or vehicle thrust, the most beneficial high speed configurations consist of small impingement angles.

When jet thrust is implemented the high speed vehicle shows positive recovered thrust, with the greatest recovered thrust in configurations 5 where jet propulsor is horizontal with a reduced drag of the thin flat plate platform. The negative recovered thrust of configuration 4 is due to shutoff propulsor. In this regime another jet propulsor placed elsewhere on the vehicle must provide thrust to maintain vehicle forward speed.

The current exploratory PARV investigation focuses on some basic PARV operating regimes and the interactions between upstream jet propulsor and the downstream platform-flap configuration. In this study, the vehicle weight and thrust were not specified and no configurations were optimized to provide the required vehicle lift. Although results are limited in scope, they provide insight into the fundamental interactions and flight regimes of the PARV including aerodynamic force prediction as geometry and flight regime are varied. In the future, an accurate parametric study will be required to study a specific PARV design in a detailed quantitative fashion.

6.5 Concluding Remarks

Overall, the numerical techniques developed for viscous ground effect studies have been validated in this thesis; ultimately providing confidence in the flow structures and pressure predictions of jet-platform-flap configurations (PARV) at small to moderate flap deflections. With the jet and flap behaviors determined in Chapters 4 and 5, the interactions between the two components in a PARV are now discussed. It is observed that the jet propulsor and platform have minimal interactions at static and moderate PARV forward speeds. However, in the high speed regime interactions begin to take place. When thrust is applied, the propulsor jet will be carried downstream before impingement and provide a narrow stream of accelerated flow over the platform. On the other hand, at high speeds with jet propulsor shut off, the duct structure then becomes a blunt body in the flow which causes separation on the propulsor and at the front of the platform. It appears that the PARV cannot be approximated by a simple platform-flap system at high speeds when non-horizontal jet propulsor configurations are utilized (create a blunt body upstream of the platform). The jet propulsor behavior is essential for accurate PARV modeling in these conditions but will become less important with horizontal propulsor.

As discussed in the introduction, three general PARV regimes were studied. The first case corresponds to the hovering regime with zero forward speed and large flap deflection. With this setup, jet flow is directed under the platform yielding the entire vehicle lift. The high-pressure cushion coupled with the large flap deflection creates a relatively large drag. Even with the large drag a positive recovered thrust results in the vehicle accelerating forward with the given parameters.

As the PARV is set at moderate forward speeds the vehicle lift is no longer solely from jet augmentation, an additional lift contribution results from passive aerodynamic forces at forward speed. In this condition, the flap deflection is reduced and the lift and drag decrease, yielding a larger recovered thrust and greater efficiency. Once again, the recovered thrust is positive, meaning the vehicle will accelerate unless drag arising from other vehicle components will hold velocity constant. Additionally, propulsor ingestion is observed in hovering and moderate forward speed configurations. Therefore, the operation in these ranges should be minimized. If flight in such a region is necessary, as studied in Chapter 5, the impingement angle should be reduced or the jet should be located further from the ground surface.

Interesting flow phenomena are observed in platform-jet interactions at high speeds. With jet propulsor positioned with a positive non-zero impingement (pointing down), an increase in drag and reduction in efficiency will occur (opposed to horizontal propulsor). In our limited study, if additional recovered thrust or lift is necessary, it appears that best configuration will place jet propulsor in a horizontal position. On the other hand, if lift is sufficient and vehicle has other means of forward thrust, the greatest high speed PAR efficiency occurs with propulsor shutoff. In all high speed cases the jet propulsor recovered thrust is non-zero. Therefore, all cases will accelerate, with the exception of the zero thrust propulsor.

Overall, the six configurations studied provide insight into PARV trends. Perhaps the most apparent trend is the large lift and drag increase with flap deflection. Other notable trends include the drag and passive aerodynamic lift increase with vehicle forward speed and the increase in high-speed vehicle lift with airfoil platform implemented. All other behaviors appear to be strongly coupled to the propulsor flow behavior, and additional studies are required to fully understand such trends.

As mentioned above, the configurations in Chapter 6 were simply chosen as they mimic the PARV flow in a few fundamental flight regimes which provide an initial overview of important flow behaviors. It is clear that the results do not correspond to a specific PARV. Future studies are necessary which will focus on aerodynamic forces and operational regimes with fixed vehicle weight and specified recovered thrust. Additionally, studies of scale effects, stability characteristics, and varying ground conditions are essential.

CHAPTER SEVEN

DISCUSSION AND CONCLUSIONS

This thesis studies the viscous numerical modeling of several advanced ground-effect concepts. Although Wing-in-Ground benefits, such as increased aerodynamic efficiency, have previously been heavily studied, development difficulties occur for heavily loaded craft in the low-speed regime where the passive aerodynamic lift cannot sufficiently support the vehicle. For heavy payload applications, a trailing edge flap can be implemented to significantly increase the lift. However, in many situations, such as the ground-effect vehicle in static or takeoff conditions, jet augmentation becomes necessary to provide low speed vehicle support. A set of parametric design studies have been completed, providing insight into flow patterns and optimal performance regimes for ground-effect vehicles with flap and jet components implemented.

As mentioned above, efficient low-cost numerical methods are used for ground effect parametric design studies. Although these methods are ideal for the current case where various configuration changes are necessary, they also provide a technique which avoids the complex experimental setups such as the wind tunnel with moving ground. The numerical method consisted of a two-dimensional, steady-state, incompressible, finite volume method utilizing RANS turbulence models; where airfoil configurations implement the Spalart-Allmaras model while planar jet studies used the standard k-ε turbulence model. Grid generation and solution of the Navier-Stokes equations are completed using commercial code Fluent 6.3.

In addition to gaining an understanding of advanced ground-effect flows, this thesis attempts to provide a general framework for modeling of Wing-In-Ground vehicles where modular components (airfoil, jet, flap) can easily be added or removed while the numerical method and equations are universal. In order to validate this numerical model, and allow its use by future researchers, experimental comparisons have been completed for all individual components separately and combined. Lift and moment forces of an airfoil outside of ground effect were first validated with and without trailing edge flap with near exact experimental agreement (Abbott and Doenhoff, 1959). Drag trends predicted the correct behavior but were off by a nearly constant increment. With acceptable agreement, the airfoil was moved into ground proximity, which quantitatively agreed with experimental data (Kikuchi et al., 2002). In addition, prediction of the planar turbulent free jet agreed with Rajaratnam's (1976) empirical data, while ground impingement configurations compared well with experiments (Tu and Wood, 1996). Finally, airfoil, jet, and flap were combined into the static PARV model of Soderlund and Matveev (2008) which shows agreement with experimental pressure distributions at small and moderate flap deflections. Overall, validation is obtained for the numerical prediction abilities for ground-effect applications with flap and jet augmentation.

Initially, the effects of simple flap mechanization were studied on a NACA 4412 airfoil in ground proximity. As the flap was deflected, flow was trapped beneath the airfoil, resulting in a decrease of flow and build-up of pressure below the airfoil. It has been observed in some configurations that the use of small flap deflections significantly increases lift while minimally increasing drag. Beneficial increases in aerodynamic efficiency are found for flap deflections up to 5% of the chord. The position of greatest efficiency appears to correspond to a flap deflection of 2.5% of the chord. This deflection region, yielding increased efficiency, is valid for all ground heights studied, and should be implemented in future designs.

With flap modeling completed, a simplified planar model of an aircraft jet propulsor, the ducted momentum source, is developed for applications modeling upstream jet suction and downstream jet spreading. Initially, the jet propulsor model is studied in an oblique impinging configuration with cross flow to determine practical ground effect operating regimes. Harmful propulsor ingestion is observed at large impingement angles and small ground distances. Results show that ingestion is avoided and downstream momentum is maximized for small impingement angles and moderate ground distances ($\theta = 15°$, $r/D = 12$). Lastly, with increasing cross flow, the upstream ground vortex reduces in size. Also, the downstream jet shows reduced spreading.

With jet and flap behaviors individually studied, components are combined in an exploratory configurational study of a PAR vehicle. First, a hovering configuration at zero forward speed and large flap deflection shows vehicle lift produced solely from jet flow directed under the platform. Then, the PARV is set at moderate forward speed where vehicle lift has contributions from jet augmentation and passive aerodynamic lift. At forward speeds, reduced flap deflection yields a larger recovered thrust and increased efficiency. At these static and moderate PARV forward speeds, propulsor ingestion is observed at an impingement angle of 30°. Although minimal platform-jet interactions are observed at static and moderate forward speeds, the high speed PARV regime creates such interactions. With thrust applied, the jet is carried downstream before impingement, providing a narrow stream of accelerated flow over the platform. On the other hand, at high speeds with jet propulsor shut off, the duct structure then becomes a blunt body in the flow which causes separation on the propulsor and at the front of the platform. Overall, no propulsor ingestion occurs at high speeds and the greatest high speed PARV performance consists of horizontal configuration with or without thrust.

Limited PARV configurations only provide insight into important flow behaviors. In the future, it is necessary for a complete study to examine PARV aerodynamic forces for a fixed vehicle weight and specified recovered thrust. In general, this thesis provides important insight into the general flow patterns and modeling techniques for advanced ground-effect vehicles.

References

[1] Abbott I, Doenhoff A. Theory of wing sections. New York: Dover Publications; 1959.

[2] Abdon A, Sunden B. Numerical investigation of combined impingement and convection heat transfer. Annals of New York Academy of Sciences 2001; 934: 417-423.

[3] Ahmed M, Takasaki T, Kohama Y. Aerodynamics of a NACA 4412 airfoil in ground effect. AIAA Journal 2007; 45(1): 37-47.

[4] Akansu YE, Sarioglu M, Kuvvet E, Yavuz T. Flow field and heat transfer characteristics in an oblique slot jet impinging on a flat plate. International Communications in Heat and Mass Transfer 2008; in press.

[5] Anderson E, Spall R. Experimental and numerical investigation of two-dimensional parallel jets. Journal of Fluids Engineering 2001; 123: 401-406.

[6] Ando S. A systematic computation scheme of PARWIG cruising performance. Transactions of the Japan Society of Aeronautical and Space Sciences 1993; 36(112): 92-106.

[7] Barber T, Leonard E, Archer D. Appropriate CFD techniques for the prediction of ground effect aerodynamics. In: WISE up to ekranoplan GEMs workshop. Sydney; 1998; p. 55-67.

[8] Batchelor GK. An Introduction to Fluid Dynamics. Cambridge University Press; 1973.

[9] Baydar E, Ozmen Y. An experimental investigation on flow structures of confined and unconfined impinging air jets. Heat Mass Transfer 2006; 42: 338-346.

[10] Beaubert F, Viazzo S. Large eddy simulations of plane turbulent impinging jets at moderate Reynolds numbers. International Journal of Heat and Fluid Flow 2003; 24: 512-519.

[11] Beitelmal AH, Saad MA, Patel CD. The effect of inclination on the heat transfer between a flat surface and an impinging two-dimensional air jet. International Journal of Heat and Fluid Flow 2000; 21: 156-163.

[12] Bennett J, Crouch K, Shulman S. Control of wake-induced exposure using an interrupted oscillating jet. AIHA Journal 2003; 64: 24-29.

[13] Bradbury LJS. The structure of a self preserving turbulent plane jet. Journal of Fluid Mechanics 1965; 23: 31-64.

[14] Chattopadhyay H, Saha SK. Turbulent flow and heat transfer from a slot jet impinging on a moving plate. International Journal of Heat and Fluid Flow 2003; 24: 685-697.

[15] Chin DT, Agarwal M. Mass transfer for an oblique impinging slot jet. Journal of Electrochemical Society 1991; 138: 2643-2650.

[16] Chuang S, Ching-Yuan W. Computations for a jet impinging obliquely on a flat surface. International Journal for Numerical Methods in Fluids 1991; 12: 637-653.

[17] Chun H, Chang R. Turbulence flow simulation for wings in ground effect with two ground conditions: fixed and moving ground. International Journal of Maritime Engineering 2003; 145: 51-68.

[18] Constantinescu G, Chapelet M, Squires K. Turbulence modeling applied to flow over a sphere. AIAA Journal 2003; 41(9): 1733-1742.

[19] Cosentino G. CFD to flight: some recent success stories of x-plane design to flight test at the NASA Dryden flight research center. In: Frontiers of computational fluid dynamics workshop. Davis, CA; Doc ID: 20070022848, 2007.

[20] Dinham-Peren TA, Craddock C, Lebas A, Ganguly A. Use of CFD for hull form and appendage design assessment on an offshore patrol vessel and the identification of a wake focusing effect. In: RINA Marine CFD 2008, Southampton, UK.

[21] Doolan C. Numerical simulation of a blunt airfoil wake using a two-dimensional URANS approach. In: Proceedings of 16th Australasian fluid mechanics conference. University of Queensland; 2007.

[22] Ferziger J, Peric M. Computational methods for fluid dynamics. New York: Springer; 1999.

[23] Firooz A, Gadami M. Turbulence flow for NACA 4412 in unbounded flow and ground effect with different turbulence models and two ground conditions: fixed and moving ground conditions. In: Int. conference on boundary and interior layers. Gottingen; 2006.

[24] Fluent. Fluent 6.2: Users manual; 2005.

[25] Gallington RW, Chaplin HR, Krause FH. Recent advances in Wing-in-Ground effect vehicle technology. In: AIAA/SNAME advanced marine vehicles conference. Arlington, VA; AIAA paper No. 76-874, 1976.

[26] Gallington RW. Power augmentation of ram wings. In: Proceedings of the conference on RAM wings and ground effect craft. RINA, London UK; 1987.

[27] Guilmineau E, Piquet J, Queutey P. On the use of turbulence models for the simulation of incompressible visous flow past airfoils at high-lift static and dynamic incidence. In: Fifteenth Intl. conference on numerical methods in fluid dynamics. 1997.

[28] Guo B, Langrish T, Fletcher D. An assessment of turbulence models applied to the simulation of a two-dimensional submerged jet. Applied Mathematics Modeling 2001; 25: 635-653.

[29] Gutmark E, Wygnanski I. The planar turbulent jet. Journal of Fluid Mechanics 1976; 73: 465-495.

[30] Haussling BH. Two-dimensional linear and nonlinear stern waves. Journal of Fluid Mechanics 1980: 97: 759-769.

[31] Hayashi M, Endo E. Measurement of flow fields around an airfoil section with separation. Transactions of the Japan Society for Aeronautical and Space Sciences 1978; 21: 69-75.

[32] Hirata N. Simulation on viscous flow around two-dimensional power-augmented ram wing in ground effect. Jour., Soc., Naval Arch. of Japan 1993: 174; 47-54.

[33] Hirata N, Hino T. Investigation of a three-dimensional power-augmented ram wing in ground effect. In: 35th aerospace sciences meeting & exhibit. Reno, NV; AIAA paper No. 97-0822, 1997.

[34] Hsiun C, Chen C. Aerodynamic characteristics of a two-dimensional airfoil with ground effect. Journal of Aircraft 1996; 33(2): 386-392.

[35] Huffman JK, Jackson CM Jr. Investigation of the static lift capability of a low-aspect-ratio wing operating in a powered ground-effect mode. NASA Technical Memorandum X-3031, 1974.

[36] Huminic A, Lutz T. CFD study of ground simulation techniques. In: 4th international conference on heat transfer, fluid mechanics and thermodynamics. Cairo, Egypt, 2005.

[37] Iaccarino G, Ooi A, Durbin P, Behnia M. Reynolds averaged simulations of unsteady separated flow. International Journal of Heat and Fluid Flow 2003; 24: 147-156.

[38] Jachowski J. Assessment of ship squat in shallow water using CFD. Archives of Civil and Mechanical Engineering 2008: 8: 27-36.

[39] Kalita K, Dewan A, Dass AK. Prediction of turbulent plane jet in crossflow. Numerical Heat Transfer 2002; 41: 101-111.

[40] Katz J, Plotkin A. Low-speed aerodynamics – from wing theory to panel methods. New York: McGraw-Hill; 1991.

[41] Kikuchi M, Hirano K, Yuge T, Iseri K, Kohma Y. Measurement of aerofoil characteristics by method of towing. Transactions of the Japan Society of Mechanical Engineers 2002; 68(676): 3378-3385.

[42] Kirillovikh VN. Russian ekranoplans. In: Twenty-first century flying ships. University of New South Wales, Sydney, Australia, 1995.

[43] Kirillovykh VN, Privalov EI. Transport amphibious platforms: a new type of high-speed craft. In: Proceedings of the workshop on ekranoplans and very fast craft. University of New South Wales, Sydney, Australia; 1996.

[44] Knowles K, Bray D. Computation of normal impinging jets in cross-flow and comparison with experiment. International Journal for Numerical Methods in Fluids 1991; 13: 1224-1233.

[45] Knystautas R. Turbulent jet from a series of holes in line. Aeronautical Quarterly 1964; XV: 1-28.

[46] Kornev NV, Matveev KI. Complex numerical modeling of dynamics and crashes of Wing-in-Ground vehicles. In: 41st aerospace sciences meeting & exhibit. Reno, NV; AIAA paper No. 2003-0600, 2003.

[47] Kotansky DR, Bower WW. A basic study of the vtol ground effect problem for planar flow. Journal of Aircraft 1978; 15: 214-221.

[48] Kotsovinos N, Angelidis P. The momentum flux in turbulent submerged jets. Journal of Fluid Mechanics 1991; 229: 453-470.

[49] Krause FH. Evaluation of a Power-Augmented-Ram wing operating free in heave and pitch over water. DTNSRDC Report ASED-385, 1977.

[50] Krothapalli A. Effects of a ground vortex on the aerodynamics of an airfoil. In: The 1987 Ground Vortex Workshop; N89-10855: 147-166.

[51] Kwag SH. Numerical study on 3-dimensional power-augmented ram wing in ground effect. In: Proceedings of the seventh international offshore and polar engineering conference. Honolulu; 1997; p.704-710.

[52] Looney MK, Walsh JJ. Mean-flow and turbulent characteristics of free and impinging jet flows. Journal of Fluid Mechanics 1984; 147: 397-429.

[53] Mahon S, Zhang X. Computational analysis of a inverted double-element airfoil in ground effect. Journal of Fluids Engineering 2006; 128: 1172-1180.

[54] Mathew S, Keith TG, Nikolaidis E. Numerical simulation of traveling bubble cavitation. International Journal of Numerical Methods for Heat & Fluid Flow 2006; 16(4): 393-416.

[55] Matveev, K.I. On the limiting parameters of artificial cavitation. Ocean Engineering 2003; 30: 1179-1190.

[56] Matveev, K.I., Three-dimensional wave patterns in long air cavities on a horizontal plane. Ocean Engineering 2007a; 34, 1882-1891.

[57] Matveev KI, Malhiot ZJ. Construction and testing of radio-controlled Power Augmented Ram models. In: Proceedings of the international mechanical engineering congress & exposition. Seattle, WA; ASME Paper No. IMECE2007-41136, 2007.

[58] Matveev KI. Static thrust recovery of PAR craft on solid surfaces. Journal of Fluids and Structures 2008; 24: 920-926.

[59] Maurel S, Solliec C. A turbulent plane jet impinging nearby and far from a flat plate. Experiments in Fluids 2001; 31(6): 687-696.

[60] Morrison J, Park M, Lee-Rausch E, Buning P, Rivers S, Rumsey C. CFD sensitivity analysis of a drag prediction workshop wing/body transport configuration. In: 21st AIAA applied aerodynamics conference. Orlando, Fl; AIAA 2003-3400; 2003; p.1-14.

[61] Narayanan V, Seyed-Yagoobi J, Page RH. An experimental study of fluid mechanics and heat transfer in an impinging slot jet flow. International Journal of Heat and Mass Transfer 2004; 47: 1827-1845.

[62] Nasr A, Lai JCS. A turbulent plane offset jet with small offset ratio. Experiments in Fluids 1998; 24: 47-57.

[63] Patankar S. Numerical heat transfer and fluid flow. Taylor & Francis; 1980.

[64] Rajaratnam N. Turbulent jets. New York: Elsevier; 1976.

[65] Rhee SH, Makarov BP, Krishinan H, Ivanov V. Assessment of the volume of fluid method for free-surface wave flow. Marine Science and Technology 2005; 10: 173-180.

[66] Roache, PJ. Quantification of uncertainty in computational fluid dynamics. Annual Review of Fluid Mechanics 1997; 29: 123-160.

[67] Roy S, Patel P. Study of heat transfer for a pair of rectangular jets impinging on an inclined surface. International Journal of Heat and Mass Transfer 2003; 46: 411-425.

[68] Rozhdestvensky KV. Aerodynamics of a lifting system in extreme ground effect. Heidelberg, Germany: Springer; 2000.

[69] Rozhdestvensky KV. Wing-in-ground effect vehicles. Progress in Aerospace Sciences 2006; 42: 211-283.

[70] Rumsey CL, Ying SX. Prediction of high lift: review of present CFD capabilities. Progress in Aerospace Sciences 2002; 38(2): 145-180.

[71] Serebrisky YM, Biachev SA. Wind-tunnel investigation of the horizontal motion of a wing near the ground. NACA Technical Memorandum 1095, 1946.

[72] Shi Y, Ray MB, Mujumdar AS. Numerical study on the effect of cross-flow on turbulent flow and heat transfer characteristics under normal and oblique semi-confined impinging slot jets. Drying Technology 2003; 21: 1923-1939.

[73] Smithey W, Papadales BS, Chaplin H. Effect of turbulent jet mixing on the static lift performance of a power-augmented-ram wing. David W. Taylor Naval Ship Research and Development Center – Report ASED 389: 1977; 1-13.

[74] Soderlund R, Matveev K. Jet-induced pressure distribution under platform in ground effect, International Journal of Aerodynamics 2008; submitted.

[75] Spalart P, Allmaras S. A one-equation turbulence model for aerodynamic flows. In: 29th aerospace sciences meeting; AIAA-92-0439, 1991.

[76] Spalart PR. Strategies for turbulence modeling and simulations, International Journal of Heat and Fluid Flow 2000; 21: 252-263.

[77] Stack J, Lindsey W, Littell R. The compressibility burble and the effect of compressibility on pressures and forces acting on a airfoil. NACA Annual Report 25; 1939; p.73-96.

[78] Steinbach D, Jacob K. Some aerodynamic aspects of wings near ground. Transactions of the Japan Society for Aeronautical and Space Sciences 1991; 34(104): 56-70.

[79] Stewart VR. The characteristics of a ground vortex and its effect on the aerodynamics of the stol configuration. In: The 1987 Ground Vortex Workshop; N89-10850: 1-38.

[80] Tafti DK, Vanka SP. Hot gas environment around stovl aircraft in ground proximity – part 2: numerical study. Journal of Aircraft 1992; 29.

[81] Thomas JL, Paulson JW, Margason RJ. Powered low-aspect-ratio wing in ground effect (WIG) aerodynamic characteristics. NASA Technical Memorandum 78793, 1979.

[82] Tu CV, Wood DH. Wall pressure and shear stress measurements beneath an impinging wall jet. Experimental Thermal Fluid Sciences 1996; 13: 364-373.

[83] Van Dam CP. Recent experience with different methods of drag prediction. Progress in Aerospace Sciences 1999; 35(8): 751-798.

[84] Van Leer B. Toward the ultimate conservative difference scheme. IV. A second order sequel to Godunov's method. Journal of Computational Physics 1979; 32: 101-136.

[85] Versteeg H, Malalasekera W. An introduction to computational fluid dynamics: the finite volume method. Pearson Prentice Hall; 1995.

[86] Viskanta, R., 1993. Heat transfer to impinging isothermal gas and flame jets. Experimental Thermal Fluid Sciences 6, 111-134.

[87] Wang HJ. An experimental study of single and multiple jets in a co-flowing ambient environment. MPhil Thesis, Dept. of Civil and Structural Engineering, The Hong Kong University of Science and Technology, Hong Kong, 1996.

[88] Wilcox DC. Turbulence modeling for CFD: third edition. DCW Industries, Inc: La, Canada, CA; 2006.

[89] Windall SE, Barrows TM. An analytic solution for two- and three-dimensional wings in ground effect. Journal of Fluid Mechanics 1970; 41(4): 769-792.

Appendix A: Nomenclature and Abbreviations

Equation Nomenclature

The nomenclature used within this work requires a short description. All governing equations are written in Cartesian tensor notation with summation convention. This method is commonly used in the literature. Indices which appear once in a term are called "free indices" and can take on values in any coordinate direction (e.g. x, y, and z). On the other hand, "repeated indices" (in a single term), are summed over all coordinate directions. In common tensor analysis the number of free indices defines the rank of the tensor. Zero, first, and second order tensors correspond to scalars, vectors, and matrices respectively.

Common Abbreviations

AMG	-	Algebraic Multigrid Solver
CFD	-	Computational Fluid Dynamics
DES	-	Detached Eddy Simulation
FVM	-	Finite Volume Method
LES	-	Large Eddy Simulation
MUSCL	-	Monotone Upstream-centered Schemes for Conservation Laws
OGE	-	Out of Ground Effect
PAR	-	Power Augmented Ram
PAR-WIG	-	Power-Augmented-Ram Wing-in-Ground Vehicle (wing section platform)
PARV	-	Power-Augmented-Ram Vehicle (using flat plate platform)
PRESTO	-	Pressure Staggered Option
RANS	-	Reynolds Averaged Navier Stokes Equations
SA	-	Spalart-Allmaras

SIMPLE - Semi-Implicit Method for Pressure-Linked Equations

URANS - Unsteady Reynolds Averaged Navier Stokes Equations

VOF - Volume of Fluid

WIG - Wing-in-Ground

Common Symbols

A - Area.

(AR) - Aspect Ratio.

b - Span.

c - Chord.

C_D - Drag coefficient: $C_D = \frac{Drag}{\frac{1}{2}\rho {u_\infty}^2 c}$.

C_f - Friction coefficient: $C_f = \frac{\tau_w}{\frac{1}{2}\rho {u_\infty}^2}$.

C_L - Lift coefficient: $C_L = \frac{Lift}{\frac{1}{2}\rho {u_\infty}^2 c}$.

$C_{m,c/4}$ - Quarter-chord moment coefficient: $C_{m,c/4} = \frac{Moment_{\ c/4}}{\frac{1}{2}\rho {u_\infty}^2 c^2}$.

C_P - Pressure coefficient: $C_P = \frac{P-P_\infty}{\frac{1}{2}\rho {u_\infty}^2}$.

D - Planar jet width.

D’ - Drag (prime simply differentiates from the jet width).

Fr, Fr_h - Froude number based on step submergence.

h - a) Distance from trailing edge of airfoil to the ground.

b) Submergence height (Appendix B).

H - Step height with respect to ship bottom (Appendix B).

H_j - Height from ground plane to centerline of propulsor exit plane

h_f - Distance from trailing edge of airfoil flap to the ground.

k, K	-	Constants as explained in text under implementation.
L’	-	Lift.
L_f	-	Length of PARV flap.
L_j	-	Distance from platform leading edge to centerline of propulsor exit plane.
L_p	-	Length of PARV platform.
P_∞	-	Atmospheric free stream pressure.
r	-	Distance along jet centerline from jet exit to intersection with ground.
Re	-	Reynolds number, ($Re = \rho UD/\mu$).
S	-	Source term.
t	-	Airfoil thickness.
τ_w	-	Shear stress at the wall.
U, u	-	Velocity.
U_o	-	Time averaged velocity at jet exit plane
$U_{centerline}$	-	Velocity along centerline of free jet.
U_∞	-	Oblique impingement cross-flow velocity or airfoil/ PARV forward speed.
V	-	Volume.
VR	-	Ratio of cross flow velocity over jet exit velocity (U_o) in jet studies.
y_f	-	Total flap deflection, $y_f = h\text{-}h_f$.
α	-	Angle of attack.
ρ	-	Density.
θ	-	Jet impingement angle measured with respect to horizontal ground.
μ	-	Dynamic viscosity.

Appendix B: Volume of Fluid Modeling of Air Cavity Ships

Introduction

Many ships produce air cavities along the hull to significantly reduce the hydrodynamic drag. In such applications, the air cavity is generally maintained by injecting air along the underside of the craft. Although this technique will achieve a drag reduction of 15-30% (Matveev, 2003), it comes with an increased cost in forcing air underneath the ship. The injection of air for a well designed Air Cavity Ship (ACS) is roughly 2% of the total propulsive power (Matveev, 2003). Overall, the common ACS provides a large drag reduction, with a simple, inexpensive, and easily maintainable design. The coupling of these benefits shows great potential for use of the ACS applications on high-speed marine vehicles.

However, the ACS performance can be greatly improved if the power needed for air injection is reduced or completely avoided. The current exploratory research looks to address the topic of completely avoiding the need of air injection. The specific approach taken will modify the air cavity ship with a vent underneath the ship; ideally allowing air to be naturally sucked underneath the ship with no external forcing. The performance of this technique is relatively unknown and the current research will attempt to determine if the naturally vented cavity is a viable solution for the air injection dilemma. Additionally, the feasibility of commercial code Fluent for these ACS simulations will be addressed.

Numerical Modeling

The vented underside of a ship is modeled with the simplified geometry shown in Fig. B.1. This geometry is two-dimensional and assumes the vent occurs behind a step like structure. At significantly large Froude numbers, based on a constant step height of h = 9.5 mm ship forward speed U = 0.684 m/s, and varying step submergence H ($Fr > 2.3$),

$$Fr_H = \frac{U}{\sqrt{gH}}, \tag{B-1}$$

the water will separate from the step (Haussling, 1980) and impinge further downstream on the bottom of the ship. This behavior may yield unsteady flow structures which can entrain air from the vent and convect it downstream underneath the ship. Therefore, this flow is governed by the unsteady two-dimensional, incompressible, constant viscosity, turbulent URANS continuity and momentum equations,

$$\frac{\partial}{\partial x_i}(\overline{u_i}) = 0, \tag{B-2}$$

$$\frac{\partial}{\partial t}(\rho \bar{u}_i) + \frac{\partial}{\partial x_j}\left(\rho \bar{u}_i \bar{u}_j\right) = -\frac{\partial \bar{p}}{\partial x_i} + \frac{\partial}{\partial x_j}\left(\mu \frac{\partial \overline{u_i}}{\partial x_j}\right) + \frac{\partial}{\partial x_j}\left(-\rho \overline{u_i' u_j'}\right) + \rho \vec{g} + \vec{F}\ , \tag{B-3}$$

where $\bar{u}_i$ is the time averaged velocity in the i-direction, and symbols ρ, μ, and $\bar{p}$ correspond to the density, molecular viscosity, and time averaged pressures, respectively. The single term in the continuity equation accounts for the advection of mass over the domain and the first and second terms on the left-hand side of the momentum equation are the transient and momentum advection terms. The terms on the right-hand side of the momentum equation are the pressure force, viscous term, Reynolds stress, gravitational body force, and surface tension force. It should be noted that Eqs. (B-2) and (B-3) above differ from general ground effect equations (2-4) and (2-5) with the added gravitational body and surface tension forces. The Reynolds stress term in Eq. (B-3) is unknown and contains the mean of the product of turbulent fluctuating velocities which is modeled with the Boussinesq approximation,

$$-\rho \overline{u_i' u_j'} = \mu_t \left(\frac{\partial \overline{u_i}}{\partial x_j} + \frac{\partial \overline{u_j}}{\partial x_i}\right) - \frac{2}{3}\left(\rho k + \mu_t \frac{\partial \overline{u_i}}{\partial x_i}\right)\delta_{ij}\,, \tag{B-4}$$

where μ_t and k represent the turbulent viscosity and turbulent kinetic energy. The Boussinesq approximation as shown by Eq. (B-4), linearly relates the Reynolds stress tensor to a mean strain rate. With this approximation the turbulent viscosity is assumed to be isotropic.

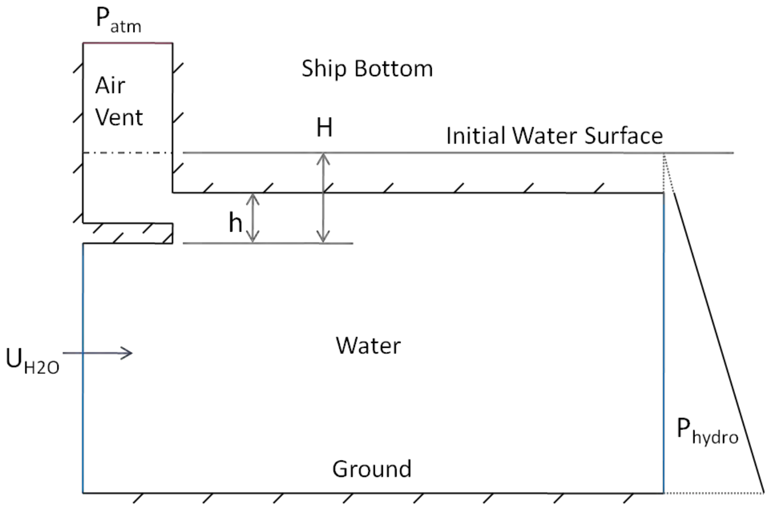

Figure B.1: Simplified air cavity ship geometry schematic.

The standard k-ε turbulence model is then implemented to provide a model for the turbulent eddy viscosity, μ_T, and provide closure for the Navier-Stokes equations with the Boussinesq approximation. The standard k-ε model solves two additional equations for turbulent kinetic energy, k, and turbulent dissipation, ε.

$$\frac{\partial}{\partial t}(\rho k) + \frac{\partial}{\partial x_i}(\rho k \overline{u_i}) = \frac{\partial}{\partial x_j}\left[\left(\mu + \frac{\mu_t}{\sigma_k}\right)\frac{\partial k}{\partial x_j}\right] + G_k - \rho\epsilon + S_k \tag{B-5}$$

$$\frac{\partial}{\partial t}(\rho \epsilon) + \frac{\partial}{\partial x_i}(\rho \epsilon \overline{u_i}) = \frac{\partial}{\partial x_j}\left[\left(\mu + \frac{\mu_t}{\sigma_\epsilon}\right)\frac{\partial k}{\partial x_j}\right] + C_{1\epsilon}\, G_k \frac{\epsilon}{k} - C_{2\epsilon}\rho\frac{\epsilon^2}{k} + S_\epsilon \tag{B-6}$$

In Eq. (B-5) ρ, μ, μ_t, σ_k, k, and ε represent the density, viscosity, turbulent viscosity, turbulent Prandtl number, turbulent kinetic energy, and dissipation. The first two terms on the left hand side of (B-5) are the transient and convection of turbulent kinetic energy while the first through fourth terms on the right hand side represent the diffusion, production (G_k), dissipation, and source (S_k) of turbulent kinetic energy.

In the dissipation equation, Eq. (B-6), $C_{1\varepsilon}$ and $C_{2\varepsilon}$ are constants and $G_{k,}$ $S_{\varepsilon,}$ and σ_ε represent the production of turbulent kinetic energy, dissipation source, and turbulent Prandtl number. The first two terms on the left hand side of Eq. (B-6) are the transient and convection of ε while the first through fourth terms on the right hand side represent the diffusion, production, dissipation, and source of ε. Although the k-ε model is only presented with Eqs. (B-5) and (B-6), a detailed description of modeling assumptions and list of constants may be found in Fluent manual (2005) or book by Wilcox (2006).

Overall, the k-ε turbulence model has been used as it and its two equation variants are commonly used for free surface flows (Jachowski 2008, Rhee et al. 2005, Dinham-Peren et al. 2008). Additionally, use of the URANS technique should be valid as the turbulent time scales are much smaller than those of the mean flow.

Lastly, to account for the interactions between the water and air at the free surface, a multiphase model must be implemented to close the problem. Fluent provides Euler-Lagrange and Euler-Euler models. The Euler-Lagrange model requires the knowledge of the number of discrete bubbles of the secondary phase (air). This method is out of the question for our current modeling as it is necessary that air bubbles develop naturally. Therefore, one of the Euler-Euler models available in FLUENT must be used: Volume of Fluid (VOF), Mixture, or Eularian. The Mixture and Eularian models can handle dispersed flows with the mixture model specifying a relative velocity between phases and the Eularian model solving a separate set of equations for each phase. Again the Mixture model is invalid as the relative velocity between phases is not known in advance, while the computational expense of the Eularian model make it unreasonable for simple applications. Therefore, the surface capturing VOF model is chosen to quantify interactions between air and water. Experimental comparisons have proven its accuracy for free surface ship flows (Jachowski 2008, Rhee et al. 2005, Dinham-Peren et al. 2008). The VOF model solves a single momentum equation for the flow (Eq. B-3) assuming velocity, turbulence, and pressure fields are shared among phases. The multiphase behavior is then accounted for by solving a modified continuity equation which tracks the volume fraction, α, in the cells,

$$\frac{1}{\rho_q}\left[\frac{\partial}{\partial t}\left(\alpha_q \rho_q\right) + \frac{\partial}{\partial x_j}\left(\alpha_q \rho_q (u_j)_q\right) = S_{\alpha_q}\right], \tag{B-5}$$

where ρ, S, and u_j are the density, source, and velocity in the j-direction respectively. The subscript, q, denotes the phase which is being solved for. In a two-phase flow Eq. (B-5) is only solved for the secondary phase while the volume fraction of the primary phase is found by the relation,

$$\sum_{q=1}^{n} \alpha_q = 1 \tag{B-6}$$

where Eq. (B-6) physically forces the sum of the volume fraction over the total number of phases, n, to result in unity. With knowledge of the phase present in each cell, the free surface and properties are determined. Ultimately the multiphase behavior is captured by the phase averaged fluid properties which enter the momentum and turbulence equations.

Although the VOF model is the most appropriate model available in FLUENT, for our current application it still has deficiencies which limit the applicability of the model. Most notably the phase interface is smeared across a finite distance instead of immediately transitioning from one phase to the other. These effects are reduced by decreasing grid size but ultimately the VOF model cannot accurately predict the dispersion of small bubbles of one phase in another. Therefore, it can be expected that the VOF model will accurately predict the mean air cavity flow structure, but will only capture air bubble entrainment when the bubble size is much larger than the mesh.

With a closed set of governing equations, the multiphase flow is solved with the PISO pressure-velocity coupling algorithm with time marching using a 1st order implicit method. The pressure is discretized by PRESTO method, momentum and turbulence use 2nd order upwind, and the volume fraction is discretized by the geo-reconstruct technique. Surface tension is applied in the VOF model by introducing an additional force depending on interface curvature and the air-water surface tension coefficient, 0.072 N/m.

The boundary conditions used on the computational domain in Fig. B.1 closely represent experimental setups being studied concurrently at Washington State University. The ground and ship bottom are modeled as no-slip wall conditions. The air vent at the top of the domain is set at atmospheric pressure with an inlet volume fraction specifying that only air enters through the vent. The boundary on the left side of the domain is modeled as a velocity inlet with water entering at a constant velocity U, corresponding to the ship forward speed. Lastly, the outlet boundary condition is specified as the hydrostatic pressure measured from the initial water surface position (H). During the initialization all cells underneath the initial water surface position are defined as water, while all above are defined as air. As the solution progresses the free surface will change but the outlet boundary condition will still depend on the initial water position which corresponds to the water surface far upstream of the ship.

An example of a computational mesh created is shown in Fig. B.2. The mesh uses a two-dimensional structured quad grid with refinement in the area in which the air cavity is thought to develop. The mesh is refined into the viscous sub-layer with a $Y+ \approx 1$. The near wall behavior is accounted for in the k-ε model with enhanced wall functions.

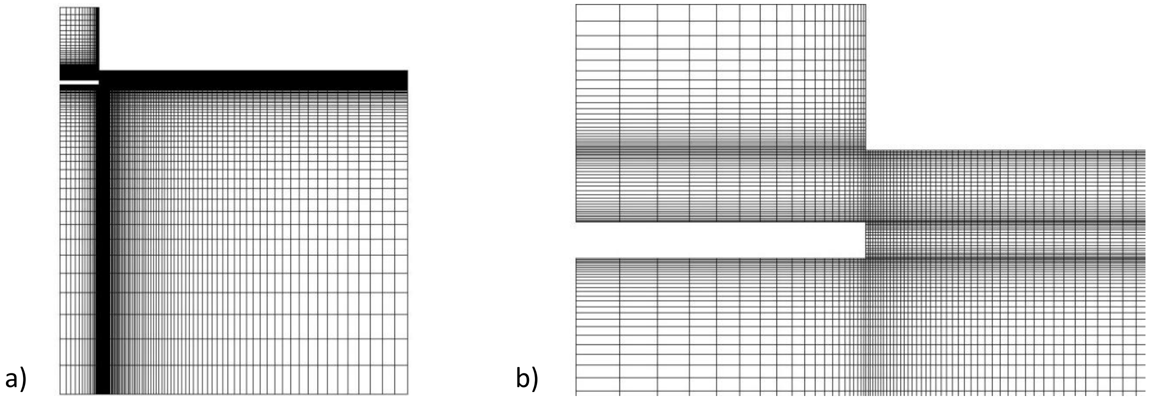

Figure B.2: Computational mesh: a) full domain; b) close up of air cavity zone.

Results

The above numerical model is implemented for a fixed ship step height of h = 9.5 mm and velocity of 0.684 m/s. In all simulations the vent geometry is additionally fixed; while the vent pressure is maintained at the atmospheric conditions. This configuration corresponds to the situation in which a natural air cavity may form. As mentioned previously, the purpose of the current study is to determine solution technique capabilities and air cavity behavior for varying ship submergence, H (and hence Froude number based on submergence).

Figure B.3 presents the free surface contours taken at instantaneous times for all submergence values. The light and dark regions in Figs B.3a-h represent the water and air phases respectively. A submergence (8 mm) corresponding to $Fr_H \approx 2.3$ (Haussling, 1980) was initially chosen to ensure step separation. The step separation and natural air cavity creation can be easily verified for all submergences in Fig. B.3. In studying the free surface contours there appear to be three distinct regions of air cavity formation. The first region, occurring at high submergence and low Froude numbers ($2.3 < Fr_H < 2.5$), is characterized by unsteady air cavity behavior. In such cases the air cavity may significantly vary in length, and it is possible for bubbles formed by air cavity to be transported in the downstream direction. As the ship submergence is moderately reduced ($2.5 < Fr_H < 2.7$) the unsteadiness in the solution is avoided and a long, steady, and relatively slender air cavity is created. In such cases the cavity length is independent of time, and no shedding is observed. The last distinct region occurs at relatively low submergence where the Froude number based on height is greater than 2.7. In this limiting case, the small submergence no longer provides downstream wave amplitudes of great enough magnitude to attach to the bottom of the ship and form an air cavity. In Figs. B.3f, g, and h the water height at the downstream domain boundary is roughly the initial height of the water surface. It appears that these cases are somewhat unrealistic as the ship is nearly entirely out of the water. Therefore, in the range studied, beneficial air cavity regimes are at low and moderate Froude numbers.

Although instantaneous snapshots of the steady regime ($Fr_H > 2.5$) are adequate, transient flow structures at high submergence and low Froude number must be addressed in more detail. Particulars have been shown in Fig. B.4 for the unsteady ship submergence of $h = 8$ mm. It is apparent that the closing portion of the air cavity is strongly unsteady. A splashing behavior occurs as the water wave impinges on the ship bottom at relatively steep angles. This behavior creates air bubbles which appear to linger in the impingement region and occasionally transport downstream. There is great potential in configurations which can utilize downstream transmitted air to create additional air cavities (such as filling the recesses studied by Matveev, 2007a) and further reduce the drag. It was expected that there may be a similar unsteady shedding regime with long slender cavities; however, no such case is observed. Although the lack of unsteadiness in long slender regimes may be physical, bubble size limitations in the current techniques limit our capabilities in this regime.

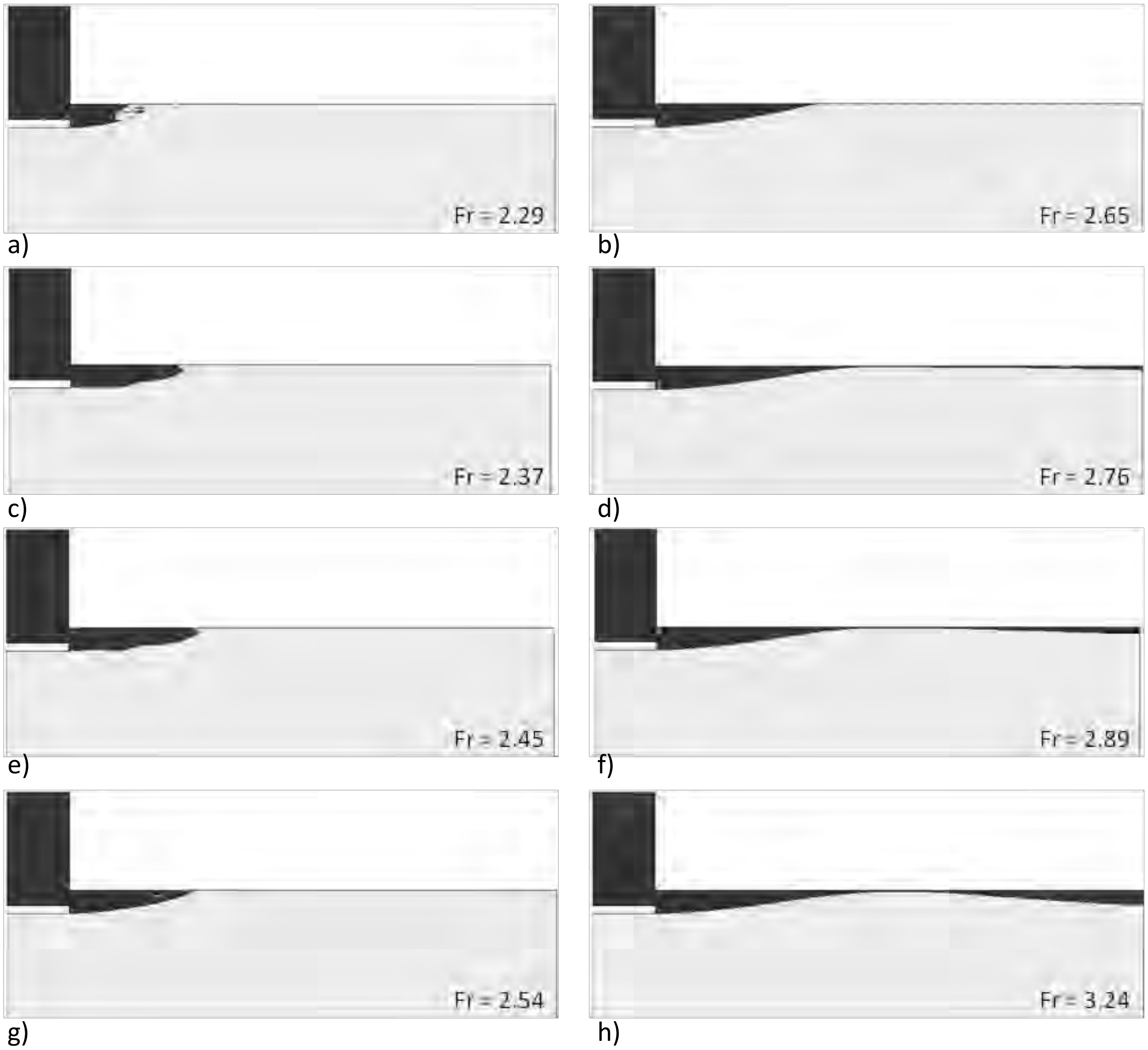

Figure B.3: Air cavity development with varying ship submergence: a) H = 8.0 mm; b) H = 7.5 mm; c) H = 7.0 mm; d) H = 6.5 mm; e) H = 6.0 mm; f) H = 5.5 mm; g) = 5.0 mm; h) H = 4 mm. Where the dark area represents air and the light area represents water.

Of the unsteady effects shown in Fig. B.4, it is important to understand why the majority of the bubbles linger in the air cavity region instead of being carried downstream. A further study of this phenomenon is shown by comparing the phase contours in Fig. B.5a with the velocity vectors in B.5b. Several recirculating “eddies” are observed in the air cavity flow patterns. With this limited analysis it appears that the unsteady air bubbles are caught in recirculation zones created in the unsteady flow and are rarely released into the downstream flow.

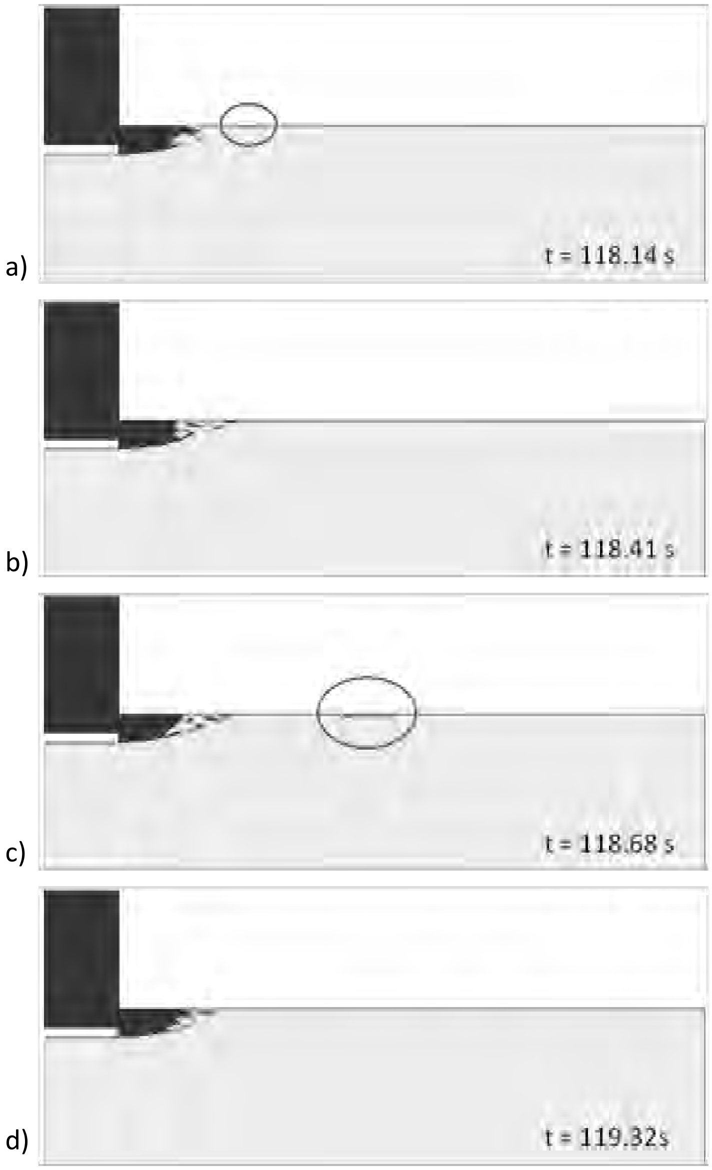

Figure B.4: Unsteady shedding cavity at large submergence and low Froude number (H = 8 mm, Fr = 2.29): a) t = 118.14 s; b) t = 118.41 s; c) t = 118.68 s; d) t = 119.32 s. Where the dark area represents air and the light area represents water.

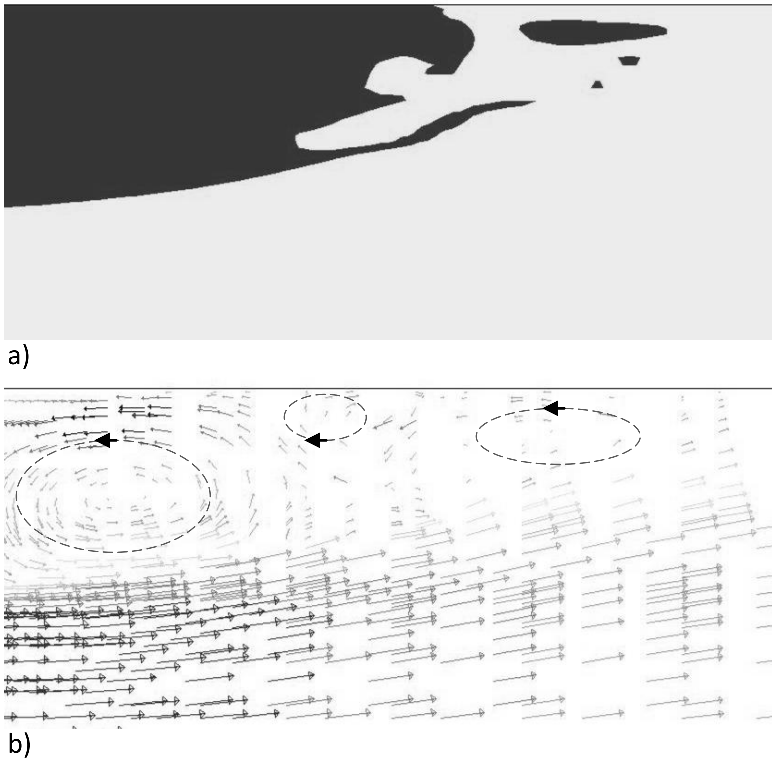

Figure B.5: Behavior at end of air cavity in an unsteady regime (H = 8mm, Fr = 2.29): a) phase contours; b) velocity vectors colored by x-velocity. In the phase contour plot the dark area represents air while the light area represents water.

Lastly, the average cavity length has been plotted with varying Froude number based on submergence. As the Froude number is increased, the cavity length is stretched, yielding a greater reduction in the friction drag. Although the small unsteady regime provides a reduced cavity length, if air shed downstream is properly utilized there is the potential for further drag reduction. As noted earlier, although the cavity length increases with Froude number, there is a limiting value where the wave no longer fully impinges on the ship bottom and the results become unrealistic ($Fr_H > 2.7$).

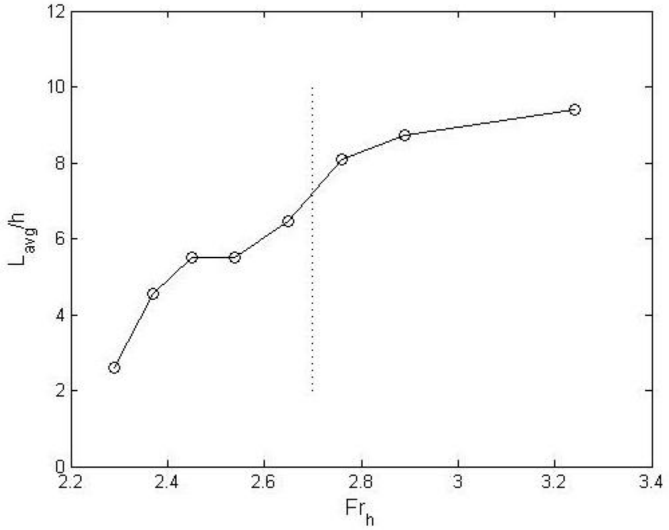

Figure B.6: Effect of Froude number on time averaged cavity length. Dotted line represents the approximate configuration limit where submergence is not great enough to cause the air cavity to fully close.

Overall, the air cavity ship study has provided support for the use of naturally formed air cavities in reducing necessary injection power. Unfortunately the beneficial regimes, including long air cavities and air shedding, appear only in very small ranges (and may be difficult to achieve). Although this information on air cavity ships is important, perhaps the most significant result is the knowledge gained on the numerical technique. The VOF method implemented in commercial code Fluent works relatively well for cases with a well defined phase interface. However, in cases with dispersed phases, including small bubbles, the accuracy is significantly reduced. In order to overcome this inaccuracy, significant mesh refinement should be completed in the area near the free surface. In cases with heavily dispersed phases, the VOF model will become invalid and another approach will be necessary.

The current model was tested for small scales only. For future high-Reynolds studies, the surface tension and viscosity may play insignificant roles, possibly resulting in different behavior (which must be studied).

Appendix C: Two-Dimensional NACA 0012 Airfoil Validation

For further numerical validation of the problem setup, an analysis of the NACA 0012 airfoil has also been completed. The NACA 0012 is a symmetric airfoil which is commonly used to validate numerical methods, and has been chosen due to the large amount of data available. The current analysis took place at a Reynolds number of $4.5 \cdot 10^6$ and an angle of attack of 6°. The specific solution parameters are very similar to the previous analysis of the NACA 4412 and are shown in Table C.1.

density	1.225 kg/m^3
viscosity	1.7894e-5 kg/m-s
chord	1 m
grid size	284550 cells
solver	2D Steady
pressure-velocity coupling	SIMPLE
press. descretization	2nd Order
mom. descretization	3rd Order Muscle
mod. viscosity descretization	3rd Order Muscle
turbulence model	Spalart-Allmaras
Y+	0.5-5

Table C.1. NACA 0012 solution parameters.

A comparison of the current simulation C_L and C_D with other numerical methods are shown in Table C.2. The numerical values for Kwag, Hirata, and Mathew were taken from references (Kwag, 1997), (Hirata, 1993), and (Mathew et al., 2006) respectively. As shown earlier the experimental values are again taken from "Theory of Wing Sections" (Abbott and Doenhoff, 1959).

Data	Current	Kwag	Hirata	Mathew	Abbott
C_L	0.658	0.6136	0.65	0.65	0.64
C_D	0.0106	0.032	0.0117	0.0135	0.0084

Table C.2. Unbounded NACA 0012 aerodynamic forces with α = 6°.

It is shown again that the lift is predicted very closely between all of the numerical methods shown. Similarly, the drag appears to be over predicted for all numerical techniques. The drag doesn’t only appear to be off, but it appears to depend on the numerical methods used. The similarity of the data to accepted numerical methods further validates the current problem setup and use of Fluent.

Appendix D: Drag Prediction Difficulties

It is widely understood that one of the current weaknesses of CFD is the prediction of drag (and viscous forces). For example, consider Figure 2.7b. Although drag follows the physically correct trend its magnitude is inaccurately predicted. This behavior is not only noticed in our numerical model, but many similar numerical results (Kwag, 1997), (Firooz and Gadami, 2006), (Hirata, 1993), (Barber et al., 1998), (Rumsey and Ying, 2002) tend to over predict the drag in comparison to experimental data (Abbott & Doenhoff, 1959). Table C.2 presents the drag prediction comparison between several published numerical models. Due to the nearly constant margin of error in the drag, drag information can still be used for relative studies.

There are a couple common theories for the error in numerical drag prediction. The most obvious occurs in the selection of the turbulence model. Most CFD codes such as Fluent only provide turbulence models for fully turbulent flow. By using a turbulence model, all flow is assumed turbulent. Most physical cases will realistically have transitional flow, where a portion of the boundary layer near the nose is laminar before transitioning to turbulent. The false assumption that the laminar flow is turbulent will increase the drag at the nose of the airfoil above its actual value. Additionally an increased turbulent viscosity will artificially damp out unsteady effects. This is thought to be one of the fundamental errors leading to drag over prediction and is discussed further by (Van Dam, 1999). A detailed study of drag errors resulting from turbulence modeling is also addressed by Wilcox (2006). Many people also suspect that some of the common drag errors may lie in the difficulty in taking accurate experimental measurements (Guilmineau et al, 1997).

One simple correction for poor drag prediction is to compare an initial numerical study with experimental data to find an average error between the two (Cosentino, 2007). This incremental error represents the average value that the numerical method is off by. For some cases a good approximation of the actual drag is found by simply adding this drag error to the numerical data. To successfully use this method, a validation study would be required to show that the drag is off by a fairly constant value over the given range.

From table C.3 it appears that all codes poorly predict the drag, and among different codes the drag prediction will also vary. The variation of drag prediction between different codes has been studied at a recent drag prediction workshop. This study compared 4 different codes which solved the same problem with the same grid. Among the codes the range in total drag prediction was 14 counts, while the standard deviation was 6 counts (Morrison et al., 2003). So, when computing drag with different codes, each code must be validated, and the drag error computed separately.

In many cases, drag may appear incorrect and cease to follow the physically expected pattern. This is generally seen when the grid is insufficient. Therefore, if this occurs, the grid may need to be refined or coarsened in important regions. A fairly coarse grid may be sufficient in finding the pressure distribution, but the viscous effects require a fine grid along the surface. It is good practice to use boundary layer cells along the solid surfaces which fall in the proper range (section 2.1.8).

The above discussion should always be considered when analyzing numerical drag data. Drag is generally poorly predicted with CFD, but using the proper techniques, you can still obtain useful design information from the numerical drag values.